EXPERIMENTAL AND NUMERICAL STUDY OF PHASE TRANSITION OF $LiFePO_4$ MATERIAL IN LITHIUM ION BATTERIES

by

MD NOOR E ALAM SIDDIQUE

Presented to the Faculty of the Graduate School of

The University of Texas at Arlington in Partial Fulfillment

of the Requirements

for the Degree of

DOCTOR OF PHILOSOPHY

THE UNIVERSITY OF TEXAS AT ARLINGTON

May 2014

Acknowledgements

I like to express my sincere thanks to my supervisor Dr. Fuqiang Liu because without his continuous support, encouragement, knowledge and technical help this program could not be finished. At various stage of this program, I went through some real hard times and he was always very supportive and kind to me at those very hard times. I am particularly very much grateful to him for being kind and supportive to me.

I also thank my committee members Dr. Choong-Un Kim, Dr. Seong Jin Koh, Dr. Yaowu Hao and Dr. David Alan Wetz for their valuable knowledgeable suggestions which helped me to find the way to overcome the difficulty in this research.

I like to extend my thanks to the Department of Materials Science and Engineering here in University of Texas at Arlington for letting me use all their facilities and for providing me the opportunity to do my research during my entire stay here. I also thank all the faculty members of the department for their knowledgeable lectures in the class and advice outside the class. I also want to thank all the department staffs, particularly Jennifer Standlee for being very nice and helpful to me.

I like to give special thanks to the Characterization Center for Materials and Biology (CCMB) as they provided me all the opportunity to use their facilities for my research. Without this facility this study could never be accomplished as I spent significant amount of time there to do my experiments. I like to thank Dr. Jiechao Jiang, the facility manager for his wonderful support and technical advice during my experimentation.

I sincerely appreciate the help and support from my labmates. They created a very friendly and professional work place here. Particularly I am grateful to Amir Hosein Salehi Gilani whose technical expertise and support was an essential ingredient of this

study. I also like to thank specially my fellow labmate Dr. Chiajen Hsu, Dong Liu, Syed Dawar Sajjad and Wei Zi for their wonderful support.

I am mostly grateful and hence thank my wife Sharmin Sultana Silvy for her wonderful support and inspiration. Without her sacrifice for me, I certainly would not be able to accomplish this degree. I like to express my gratitude to my family members, specially my mother who always inspires me, believes me and prays for me to Allah for my protection and my father who was always proud of me and whose presence was one of my biggest inspirations. I also thank my father-in-law and mother-in-law for their continuous inspiration.

December 5, 2013

Abstract

EXPERIMENTAL AND NUMERICAL STUDY OF PHASE TRANSITION OF $LiFePO_4$ MATERIAL IN LITHIUM ION BATTERIES

Md Noor E Alam Siddique, PhD

The University of Texas at Arlington, 2014

Supervising Professor: Fuqiang Liu

Phase transition behavior of $LiFePO_4$ material has been studied in this work. During electrochemical charge/discharge processes, $LiFePO_4$ transforms into $FePO_4$ and this electrochemically driven phase transition of the two-phase system results in a potential plateau in a battery discharge curve. Besides, battery performance, especially under high rates, depends critically on this two-phase transition. However, this phase transition mechanism in the $LiFePO_4$ crystal structure has yet not been understood in details. Developing better understanding is essential for designing high performing, safe and stable batteries.

Currently available phase transition models for $LiFePO_4$, such as the classical 'core-shrinking model' and recently the 'domino cascade model', have shed lights on the phase transition mechanism, however, with somewhat contradicting conclusions. The former predicted a continuous phase transition between $LiFePO_4$ and $FePO_4$ within an individual particle. In contrast, the latter, based on the fact of anisotropic diffusion of Li, provided a microscopically heterogeneous picture of phase transition: phase transition is abrupt, and de-lithiated and lithiated particles co-exist in a battery electrode.

To achieve a better understanding of the two-phase transition phenomena, two specially designed sophisticated methods, i.e., in-situ Raman spectroscopy and in-situ X-ray Diffraction (XRD), have been developed in this work. The particle level phase transition of $LiFePO_4$ was probed in the in-situ Raman study. Under slow-rate

discharge/charge, it was found that the particles were either fully transformed or untransformed indicating that the phase transition in $LiFePO_4$ material was not uniform at the particle level. Electronic conductivity and local electrode microstructure determined the preferred sequence of phase transition of the particles. This study also revealed that non-equilibrium phase transition occurred as a result of delayed phase transition. The in-situ XRD study attempted to investigate the bulk level phase transition behavior of $LiFePO_4$ and was conducted at four different discharge rates. Analysis of the high-resolution diffraction patterns showed a gradual and continuous change in phase transition. Again, a delayed phase transition was observed at high-rate discharge due to the non-equilibrium pathway. From both in-situ Raman and in-situ XRD experiments, only two stoichiometric compounds ($LiFePO_4$ and $FePO_4$) was detected, indicating that during electrochemical charge/discharge processes once Li ion de-intercalates/intercalates, it immediately forms the end-members and no intermediate compounds exist.

Particle size and morphology of $LiFePO_4$ were also studied using numerical models in the phase transition behavior. At a slow discharge rate, plate shaped particles showed higher capacity than spherical particles and the opposite trend was observed at high discharge rates above some critical discharge rates. Big particles and high discharge rates induced non-equilibrium phase transition in the $LiFePO_4$ particles which expands the miscibility gap between the end-members and gave sharp narrow two-phase interfaces.

Table of Contents

Acknowledgements iii

Abstract v

List of Illustrations x

List of Tables xvii

Chapter 1 Introduction 1

Chapter 2 Background Information and Objective of the Study 5

2.1 Introduction 5

2.2 Li ion Battery System 5

2.2.1 Battery components 5

2.2.2 Performance Parameters and Selection Criteria of Battery Materials 6

2.2.3 Battery Materials 10

2.2.3.1 Anode and Electrolyte 10

2.2.3.2 Cathode 10

2.3 $LiFePO_4$ Materials 12

2.3.1 Structure of $LiFePO_4$ 12

2.3.2 Thermodynamics of $LiFePO_4$ 13

2.3.3 Phase Transition Models 15

2.3.3.1 Core Shrinking Model 15

2.3.3.2 Domino Cascade Model 17

2.3.4 Experimental techniques to study Phase Transition of $LiFePO_4$ 20

2.4 Scope of study and objectives 24

Chapter 3 Synthesis of LiFePO4 Particles and Li ion Battery Making 26

3.1 Introduction 26

3.2 Synthesis of $LiFePO_4$ 26
3.2.1 Solid State Synthesis 26
3.2.2 Characterization 27
3.3 Electrode Fabrication 30
3.4 Electrolyte Preparation 33
3.5 Battery Assembly 33
Chapter 4 In-situ Studies using Raman Spectroscopy 35
4.1 Introduction 35
4.2 Design of Battery Casing 36
4.3 Electrode Fabrication and Battery Making 38
4.3.1 Electrode Fabrication 38
4.3.2 Battery Making 39
4.3.3 Raman Laser Interaction with battery components and Corrective measures 40
4.4 In-situ Raman experiment: Data Recording and Analysis 44
4.4.1 First Cycle: Slow discharge 45
4.4.2 Effect of Discharge rate: Second and Third cycle 50
4.5 Conclusion 54
Chapter 5 In-situ X-ray Diffraction (XRD) Study 55
5.1 Introduction 55
5.2 Making battery housing for in-situ XRD study 55
5.3 Electrode preparation and battery assembly for in-situ XRD study 57
5.4 In-situ XRD experimentation 59
5.4.1 Test Protocol and Recording the real-time phase transformation 59
5.4.2 Effect of Discharge rate 66

5.5 In-situ Raman results vs. in-situ XRD results 73
5.6 Conclusion 76
Chapter 6 Numerical study of phase transition 77
6.1 Introduction 77
6.2 Mushy Zone Approach 78
6.2.1 Model Description 79
6.2.2 Effect of Diffusivity through two-phase interface 83
6.2.3 Validation of model using equilibrium simulation 84
6.2.4 Particle Geometry Effect 86
6.2.5 Particle Size Effect 92
6.2.6 Nature of two-phase interface 95
6.3 Conclusion 98
Chapter 7 Conclusion 100
Appendix A Code for simulating Spherical particles 103
Appendix B Code for simulating Plate Shaped particles 109
References 118
Biographical Information 136

List of Illustrations

Figure 1.1: Electric vehicle sales and lithium demand for electric vehicle batteries from 2008 to 2020 [2]. 2

Figure 1.2: Comparison of volumetric and gravimetric energy densities of various rechargeable battery systems [3]. 3

Figure 2.1: Schematic illustration of Li ion battery system including Li ion movement during charging and discharging. 6

Figure 2.2: (a) Thermodynamic stability criteria of the electrolyte, (b) Selection criteria for electrode materials based on the thermodynamic stability criteria of the electrolyte [18]. . 9

Figure 2.3: Comparison of thermal runaway properties of different cathode materials for LIBs [58]. 11

Figure 2.4: a) Crystal structure of $LiFePO_4$, b) a layer of $LiFePO_4$ which consists of FeO_6 octahedra and PO_4 tetrahedra [73]. 12

Figure 2.5: Schematic representation of Gibbs free energy with the Li ion content and associated two-phase mixture region. 13

Figure 2.6: Schematic representation of Gibbs free energy of the α-β two-phase system and associated potential profile during discharge. 14

Figure 2.7: Illustration of the shrinking-core model during discharge. [75] 16

Figure 2.8: Schematic view of the 'domino-cascade' mechanism for the lithium de-intercalation /intercalation mechanism in $LiFePO_4$ crystallites [73]. 18

Various techniques have been employed to study the phase transition of $LiFePO_4$ materials to date. To study the Li ion insertion behavior, different research groups used either chemical [60, 79-81, 86-91] or electrochemical [76, 85, 90, 92-101] lithiation/de-lithiation processes. Besides probing these phase transition was attempted using both

Figure 2.9: Schematic representations of the $LiFePO_4$ (in red) and $FePO_4$ (in green)

phases in the four models proposed in the literature for the Li insertion/extraction mechanisms in $FePO_4$ /$LiFePO_4$ materials: (a) bulk core shell model, [4, 103] (b) radial core shell model, [79] (c) domino-cascade model, [73] and (d) a 4^{th} model that can be called as the spinodal decomposition model freely schematized from ref [80]. In all of the models, except the domino-cascade model, the particles are mixed and composed of the two phases [85]. 20

Figure 3.1: Flow diagram for solid state synthesis method to synthesize $LiFePO_4$ material. 27

Figure 3.2: XRD patterns obtained from materials synthesized through solid state synthesis method. JCPDS card # 81-1173 is shown in bottom plot. 28

Figure 3.3: Particle size distribution of the synthesized LiFePO4 material at 700 ^oC for 8 hours. 29

Figure 3.4: FE-SEM image of the solid state synthesized $LiFePO_4$ material at 700 ^oC for 8 hours. 29

Figure 3.5: Schematic of slurry making process containing active material and conducting carbon. 30

Figure 3.6: Schematic of electrode (cathode) fabrication process where doctor blade is used to coat $LiFePO_4$ slurry on Al current collector. 31

Figure 3.7: SEM image of a cathode containing 70% C-$LiFePO_4$, 20% Conductive carbon and 10% PVDF binder. 32

Figure 3.8: Galvanostatic charge discharge profile of a lithium ion cell. Cathode Composition is 70% C-$LiFePO_4$, 20% Conductive carbon and 10% PVDF binder. C_2 and D_2 indicate the 2^{nd} cycle charge and discharge profile while C_3 and D_3 indicate the 3^{rd} cycle charge and discharge profile. 34

Figure 4.1: Schematic of the cell design for in-situ Raman spectroscopy. The real working cell operating in the Raman spectrometer sample holder is shown in the bottom. 37
Figure 4.2: Schematic of the cathode making process specially suitable for in-situ Raman spectroscopy. 38
Figure 4.3: Raman spectra from four different areas after carbon gasification treatment. Areas A and B show decomposition of $LiFePO_4$ while areas C and D shows the vibration signal of PO_4^{3-} (υ1) of $LiFePO_4$ material [106]. 43
Figure 4.4: Raman mapping of a area after carbon gasification process of the electrode. The points with intense signal from the vibrational signal of PO_4^{3-} (υ1) of $LiFePO_4$ material can easily be found from this map which can be used for subsequent in-situ study [106]. 44
Figure 4.5: Schematic showing electrode configuration for in-situ study. The small laser spot only focuses on few active material particles. 45
Figure 4.6: Charge discharge cycle at 0.3C rate during slow rate in-situ Raman spectroscopy. Blue line indicates the current profile and the black line indicate the potential profile and vertical lines on them indicates the point when the Raman spectra were recorded. 46
Figure 4.7: Raman spectra collected during electrochemical charge discharge at 0.3C. R1, R2, and R3 indicates the Raman spectra collected during rest period and C1, C2, etc indicates the Raman spectra taken during charge and D1, D2, etc are Raman spectra taken during discharge as indicated in Fig. 4.6. 47
Figure 4.8: Peak de-convolution and Gaussian fit analysis of one representative Raman spectra D1 collected during electrochemical discharge at 0.3C. The time when D1 is indicated by the 1st vertical line on the potential profile of discharge curve in Fig. 4.6. 48

Figure 4.9: (a) Progress of phase transition during charge and discharge at 0.3C. (b) Current and Potential profile during charge and discharge is shown along with the points when Raman spectra were recorded. 49

Figure 4.10: (a) Progress of phase transition during charge and discharge at 1C. (b) Current and Potential profile during charge and discharge is shown along with the points when Raman spectra were recorded. 52

Figure 4.11: (a) Progress of phase transition during charge and discharge at 2C. (b) Current and Potential profile during charge and discharge is shown along with the points when Raman spectra were recorded. 53

Figure 5.1: Schematic of the cell design for in-situ XRD study is shown on the left side and the real working cell operating in the X-ray diffractometer sample holder is shown on the right side. 56

Figure 5.2: XRD spectra shown under the Kapton film indicates the suitability of using as a X-ray transparent window material in the electrochemical cell to be used in in-situ XRD study. 57

Figure 5.3: Charge discharge cycle at 0.1C rate (1^{st} cycle) during slow rate in-situ Raman spectroscopy. Blue line indicates the current profile and the black line indicate the potential profile and vertical lines on them indicates the point when the Raman spectra were recorded. 61

Figure 5.4: XRD patterns collected during electrochemical charge discharge at 0.1C (1^{st} cycle). R1, and R2 indicates the XRD patterns collected during rest period and C1, C2, etc indicates the XRD patterns taken during charge and D1, D2, etc are XRD patterns taken during discharge as indicated in Fig. 5.4. 62

Figure 5.5: Peak de-convolution and Gaussian fit analysis of one representative XRD pattern D6 collected during electrochemical discharge at 0.1C. The time when D6 is indicated by the 6th vertical line on the potential profile of discharge curve in Fig. 5.3.....63
Figure 5.6: (a) Phase transition progress during electrochemical charge discharge at 0.1C (1st cycle). The dotted lines indicate the equilibrium progress paths. (b) Electrochemical charge discharge profiles of the 1st cycle, where blue lines indicate current profile and black lines indicate potential profile. 65
Figure 5.7: Phase transition progress line during electrochemical discharge at 0.1C (1st cycle) after the correction of history from the charge process. The dotted line indicates the equilibrium progress path.....66
Figure 5.8: (a) XRD patterns collected during electrochemical charge discharge at 2nd cycle. (b) at 3rd cycle (c) at 4th cycle. R1, and R2 indicates the XRD patterns collected during rest period and C1, C2, etc indicates the XRD patterns taken during charge and D1, D2, etc are XRD patterns taken during discharge.....67
Figure 5.9: (a) Phase transition progress line during electrochemical charge discharge during 2nd cycle (0.3C discharge). The dotted lines indicate the equilibrium progress paths. (b) Electrochemical charge discharge profiles of the 2nd cycle, where blue lines indicate current profile and black lines indicate potential profile.....69
Figure 5.10: (a) Phase transition progress line during electrochemical charge discharge during 3rd cycle (0.5C discharge). The dotted lines indicate the equilibrium progress paths. (b) Electrochemical charge discharge profiles of the 3rd cycle, where blue lines indicate current profile and black lines indicate potential profile.....71
Figure 5.11: (a) Phase transition progress line during electrochemical charge discharge during 4th cycle (1C discharge). The dotted lines indicate the equilibrium progress paths.

(b) Electrochemical charge discharge profiles of the 4th cycle, where blue lines indicate current profile and black lines indicate potential profile. 72

Figure 5.12: Phase transition progress line during electrochemical discharge at all four different discharge rates after the correction of history from the charge process. The dotted line indicates the equilibrium progress path. 73

Figure 5.13: Phase transition progress lines obtained during different discharge rates and from in-situ Raman spectroscopy and from in-situ XRD study. 74

Figure 5.14: Schematic explaining phase transition mechanism during equilibrium and non equilibrium process at slow and high discharge rates. In-situ Raman study area and in-situ XRD study area in the electrodes are also marked in the schematic. 75

Figure 6.1: Schematic illustration of equilibrium and non-equilibrium phase transformation in (a) battery discharge and (b) phase diagram. α and β are referring to the Li-poor phase ($FePO_4$) and Li-rich phase ($LiFePO_4$), respectively. 79

Figure 6.2: Impact of interfacial diffusion coefficient on discharge capacity and battery performance (inset) for a sphere with radius of 20 nm. Values of *A* in the function $f(c_{Li}) = Ab^{1.8}$ are **1**: 9.45x10^{-5}, **2**: 1.08x10^{-4}, **3**: 1.35x10^{-4}, **4**: 6.74x10^{-4}, and **5:** 1.08x10^{-3}. 83

Figure 6.3: Impact of interfacial diffusion coefficient on discharge performance and particle surface composition (inset). The simulation is done for a sphere with radius of 20 nm at discharge rate of 20C. The dash lines in the inset indicate the equilibrium and maximum compositions. 84

Figure 6.4: Li concentration distribution along the normalized thickness of a 20 nm-thick plate at discharge rate of 0.5C. *A*=0.00135 in $f(c_{Li})$ has been used for the MZ model. 85

Figure 6.5: Variation of Li concentration at the front and back surfaces of the 20 nm-thick plate during discharge at 0.5C. The inset compares the discharge performance. 86
Figure 6.6: Discharge performance of a $LiFePO_4$ plate and a sphere at 0.5C. The inset shows particle surface concentration of Li near completion of discharge. 88
Figure 6.7: Li concentration profiles along the normalized thickness during discharge in (a) a plate (thickness l_0=20 nm) and (b) a sphere (radius r_0=20 nm) at 2C discharge rate. The state-of-discharge is indicated in the figures. The dash lines indicate the thermodynamic equilibrium phase compositions. 89
Figure 6.8: Comparison of capacity as a function of discharge rate for plate-shaped and spherical particles. 90
Figure 6.9: Ratio of the Li ion flux at the two-phase interface for two different particle shapes during discharge. 91
Figure 6.10: Discharge performances of single spherical particle of $LiFePO_4$ at a) 0.5C, b) 1C and c) 2C rate. 93
Figure 6.11: Miscibility gap during the discharge process for different particle size at a) 0.5C, b) 1C and c) 2C discharge rate. 94
Figure 6.12: Li concentration profiles at SOD of 44% for different particle size at a) 0.5C, b) 1.0C, and c) 2.0C. 96
Figure 6.13: Gradient of chemical potentials of spherical particles at 1C discharge rate at 44% SOD (corresponding to Fig. 6.12b). 97

List of Tables

Table 4.1: List of Raman active vibration modes for components (electrode material and electrolyte) of the working battery. 40

Table 5.1: Protocol of the electrochemical charge-discharge for the in-situ XRD study. . 60

Table 6.1: Parameters used in the simulation (Refs. [42, 105]) 82

Chapter 1

Introduction

Extensive use of energy storage or batteries started with revolution in development of portable devices like cell phones, cameras, personal notebooks etc. Some of these portable devices can use primary batteries or secondary batteries that are also known as rechargeable batteries. One of the widely known rechargeable batteries is the led acid batteries. Later on, small sized nickel-cadmium, nickel-metal hydride batteries were also developed which occupy a huge consumer market. With the development of these secondary batteries, and also different consumer electronic devices, the need for batteries with high energy density becomes more and more prominent to meet the continuous demand for smaller, light weight, reliable, and high performing devices. The first breakthrough to meet these demands came with the development of lithium ion batteries (LIB) in the 90's. Since then, the demand for LIBs increased exponentially and by now already crossed $13000 million value [1]. The present and future demand scenario is compared in Fig. 1.1, where one most potential application is either plug-in hybrid electric vehicles (PHEV, HEV) or electric vehicles (EV).

LIBs first came with the promise of having high energy density. The energy density of different secondary rechargeable batteries is compared in Fig. 1.2. As is shown, LIBs show higher volumetric and gravimetric energy density than most of the other rechargeable batteries. Higher volumetric and gravimetric energy density enables smaller and lighter batteries. So, this unique battery system becomes an automatic potential choice for EV technologies. For this reason, scientists and engineers focused on this battery system within the last two decades and published thousands of research papers. The research areas include development of new electrode material, electrolyte

solution, and separator material, optimizing the battery parameters, battery design, safety and durability and obviously reducing cost.

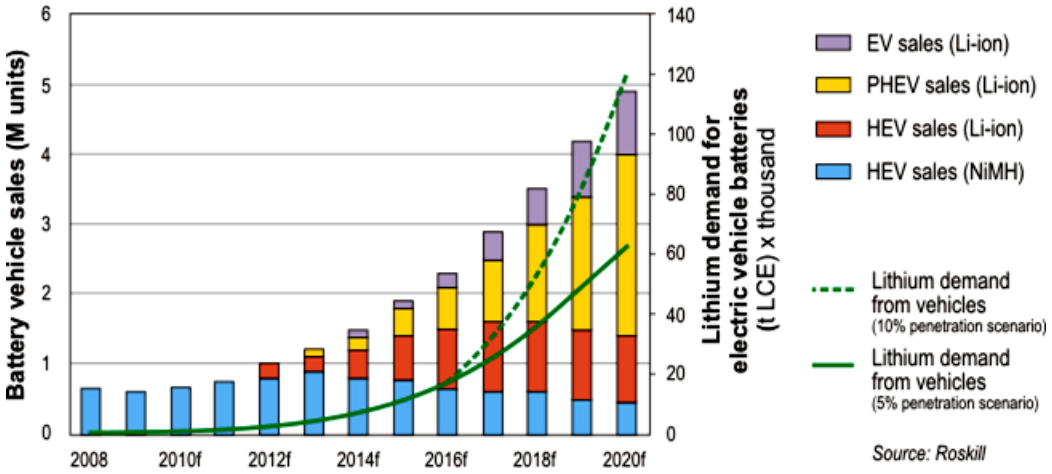

Figure 1.1: Electric vehicle sales and lithium demand for electric vehicle batteries from 2008 to 2020 [2].

The battery technology can be advanced through improving material, design and employing better battery management practices. But without improving the material itself the energy storage technology cannot move forward. This LIB technology is one such example where new material system gave high performing, reliable energy storage system with high energy density. To further improve the charge/discharge capacities and reliability of LIBs, the materials used have to be advanced. Discovering new electrode materials and understanding their structure-performance relationship are keys to the above-mentioned improvement.

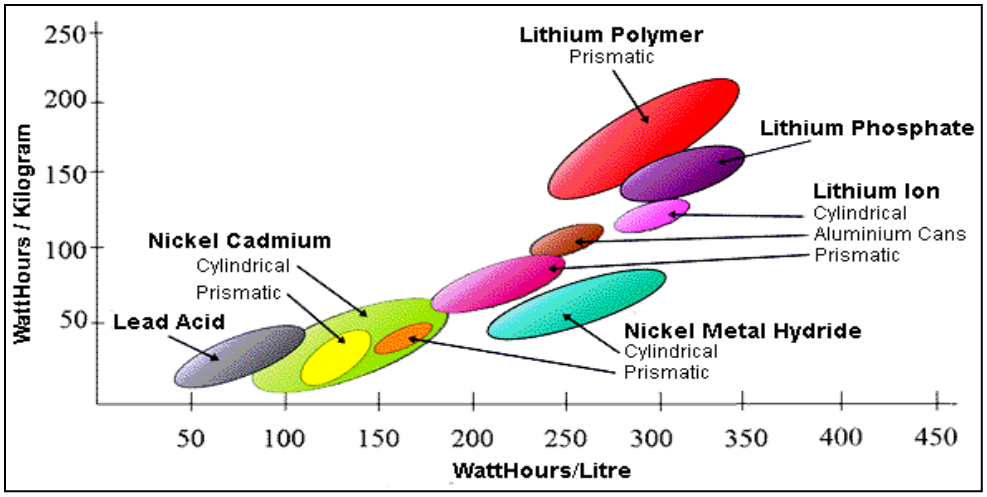

Figure 1.2: Comparison of volumetric and gravimetric energy densities of various rechargeable battery systems [3].

When LIBs was first introduced, the cathode material used was mostly transition metal oxide materials. And then one breakthrough in cathode materials came with the introduction of $LiFePO_4$ of olivine structure [4]. This material is safe, stable, cheap, easy to synthesize and also able to deliver high capacity. The poor electronic conductivity of this material was a problem initially and later on it was fixed using different techniques and approaches.

$LiFePO_4$ gives a very flat potential plateau during discharge due to the presence of a two phase system. But at high discharge rates, this material shows reduced capacity and reduced potential due to partly lithium ion diffusion problems through anisotropic crystallographic channel and partly due to the unique phase transition phenomena. Slow discharge leads to the equilibrium phase transition (between lithium rich $LiFePO_4$ and lithium poor $FePO_4$) where Li diffusion through anisotropic crystallographic channel does not necessarily compete with the Li flux that comes from the electrochemical discharge rates. That results in a stable potential and good capacity during the equilibrium phase transition. On the other hand, non-equilibrium phase transition could appear at higher

discharge rates, which is complicate because of the anisotropic Li diffusion, Li ion migration difficulty through porous network and the presence of a narrow interface between end members ($LiFePO_4$ and $FePO_4$) with very limited Li ion diffusivity.

Apart from all these issues, the phase transition phenomena in $LiFePO_4$ material, both equilibrium and non-equilibrium are not well understood so far. There exist many debates on several key issues regarding this phase transition mechanism. This very intrigue and important phase transition phenomenon is the motivation to study further the phase transition mechanism, which forms the central theme of this study. This work thus strives to clarify the phase transition mechanism and also to understand the particle level phenomena of $LiFePO_4$ materials.

This dissertation begins with a very general description of LIB system together with introduction on battery materials and their selection criteria in Chapter 2. Chapter 2 also includes description of $LiFePO_4$ material, its phase transition models and representative techniques to study the phase transition, and finally concludes with a list of objectives of this study. Chapter 3 describes the $LiFePO_4$ synthesis method and the characterization tools and most importantly details of electrode and battery making procedures.

The two main experimental techniques, i.e., in-situ Raman spectroscopy and in-situ XRD, to study the phase transition phenomena in LIBs containing $LiFePO_4$ are discussed in details in Chapter 4 and Chapter 5. Due to experimental limitation every aspect of the phase transition behavior cannot be studied experimentally and hence numerical study on individual $LiFePO_4$ particles is included in Chapter 6. And lastly Chapter 7 summarizes the key findings of this work and proposes future work.

Chapter 2

Background Information and Objective of the Study

2.1 Introduction

LIBs have some basic components: anode, cathode, electrolyte, and separator. Extensive amount of research has already been devoted to improvement of performance of LIBs through developing electrode materials [5-9], reducing particle size [10] and optimizing shape [7, 11, 12] of active material particles of the electrode, and using different additives [13-15].

$LiFePO_4$, one prominent cathode material that shows a stable plateau of potential during discharge due to the unique phase transition through movement of the two-phase interface [16]. In this chapter, details of the LIB system, materials, their attributes and particularly details of $LiFePO_4$ materials, its phase transition behavior are discussed. Finally, based on existing study on this material and theoretical knowledge, a scope of research will be identified.

2.2 Li ion Battery System

2.2.1 Battery components

In the schematic illustration of Fig. 2.1, during charge lithium ions come out of the cathode ($LiFePO_4$), and travel through the electrolyte and separator (which should be permeable to lithium ion), and become intercalated into the anode. During discharge, the above processes reverse. In this particular case of Fig. 2.1, the anode is made of graphitic carbon coated on top of a copper foil along with some binder (PVDF) and the cathode is $LiFePO_4$-based material coated on an aluminum foil along with conducting additives such as carbon.

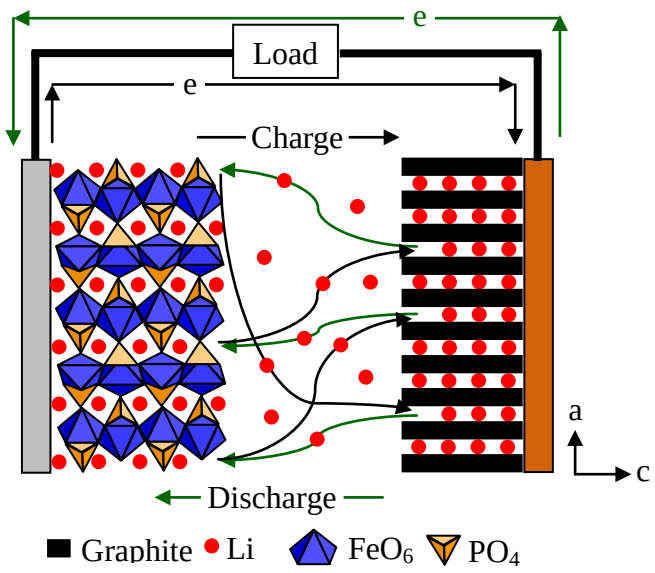

Figure 2.1: Schematic illustration of Li ion battery system including Li ion movement during charging and discharging.

The battery reactions can be expressed as follows:

Anode reaction: $6C + xLi^+ + xe^- \leftrightarrow C_6Li_x$

Cathode reaction: $LiFePO_4 \leftrightarrow Li_{(1-x)}FePO_4 + xLi^+ + xe^-$

where the forward direction (from left to right) indicates charge reaction and the reverse direction indicates discharge reaction.

2.2.2 Performance Parameters and Selection Criteria of Battery Materials

Performance of the energy storage systems is relying on several parameters and also depending on the applications, though some specific parameters become more important comparing to others. These parameters include the potential, power the battery delivers to the device, storage capacity, columbic efficiency on energy discharge, charge/discharge rate, etc. The selection of battery materials significantly depends on open circuit voltage (OCV) of the cell. The OCV depends directly on the chemical potential of the electrode materials and is described as [17]

$$V_{OC} = \left(\mu_A - \mu_C\right) \Big/ F \quad \text{.....2.1}$$

where μ_A and μ_C are the chemical potentials of the anode and cathode materials respectively and *F* is the Faraday constant. In a battery electrode, due to low conductivity of the solid phases and liquid electrolyte phase, as well as slow electrochemical reactions, the voltage V_{dis} obtained during discharge can be decreased by an amount of η_{dis} which is called overpotential [17].

$$\eta_{dis} = V_{OC} - V_{dis} \quad \text{.....2.2}$$

Similarly, during a charge process a certain overpotential η_{ch} has to be applied together with the OCV and hence the overpotential can be expressed as

$$\eta_{ch} = V_{ch} - V_{OC} \quad \text{.....2.3}$$

where V_{ch} is the potential applied when charging the cell.

In a complete discharge process, the effective energy density stored in the cell is *QV/W*, where *Q* is the amount of charge transferred and *W* is the weight of the cell. During a galvanostatic discharge, near the end of discharge process diffusion of Li ions through electrode materials and Li ion migration through electrolyte limits the capacity (*Q/W*) which will appear lower than the theoretical capacity.

Battery performance is characterized with two kind of efficiency such as energy efficiency and columbic efficiency. The energy efficiency of a lithium ion cell is [17]

$$EnergyEfficiency = \left(\int_0^Q V_{dis}\, dq \Big/ \int_0^Q V_{ch}\, dq \right) \quad \text{.....2.4}$$

And the columbic efficiency can be expressed as

$$ColumbicEfficiency = \left(Q_{dis} \Big/ Q_{ch} \right) \quad \text{.....2.5}$$

Several cells are connected in series to get a desired voltage *V* and in parallel to get the desired capacity *Q* for specific application.

The open circuit potential can be chosen according to Eq. 2.1 by changing the electrode material. But the electrode material cannot be randomly chosen as the electrolyte might decompose in the operating potentials if the potential is above or below the stability potential window of the electrolyte. The potential window of the electrolyte system is

$$E_g = E_{LUMO} - E_{HOMO} \quad \text{.....2.6}$$

where the LUMO and HOMO are respectively the lowest unoccupied molecular orbital and highest occupied molecular orbital of the electrolyte. Fermi energy level of the anode E_{FA} has to be lower than LUMO and the Fermi energy level of the cathode E_{FC} has to be higher than the HOMO to fulfill the thermodynamic stability criteria. If the E_{FC} lies above the electrolyte LUMO, the electrolyte will be reduced and if the E_{FA} lies below the electrolyte HOMO, the electrolyte will be oxidized which results in the following thermodynamic stability criterion.

$$eV_{OC} = E_{FA} - E_{FC} \leq E_g \quad \text{.....2.7}$$

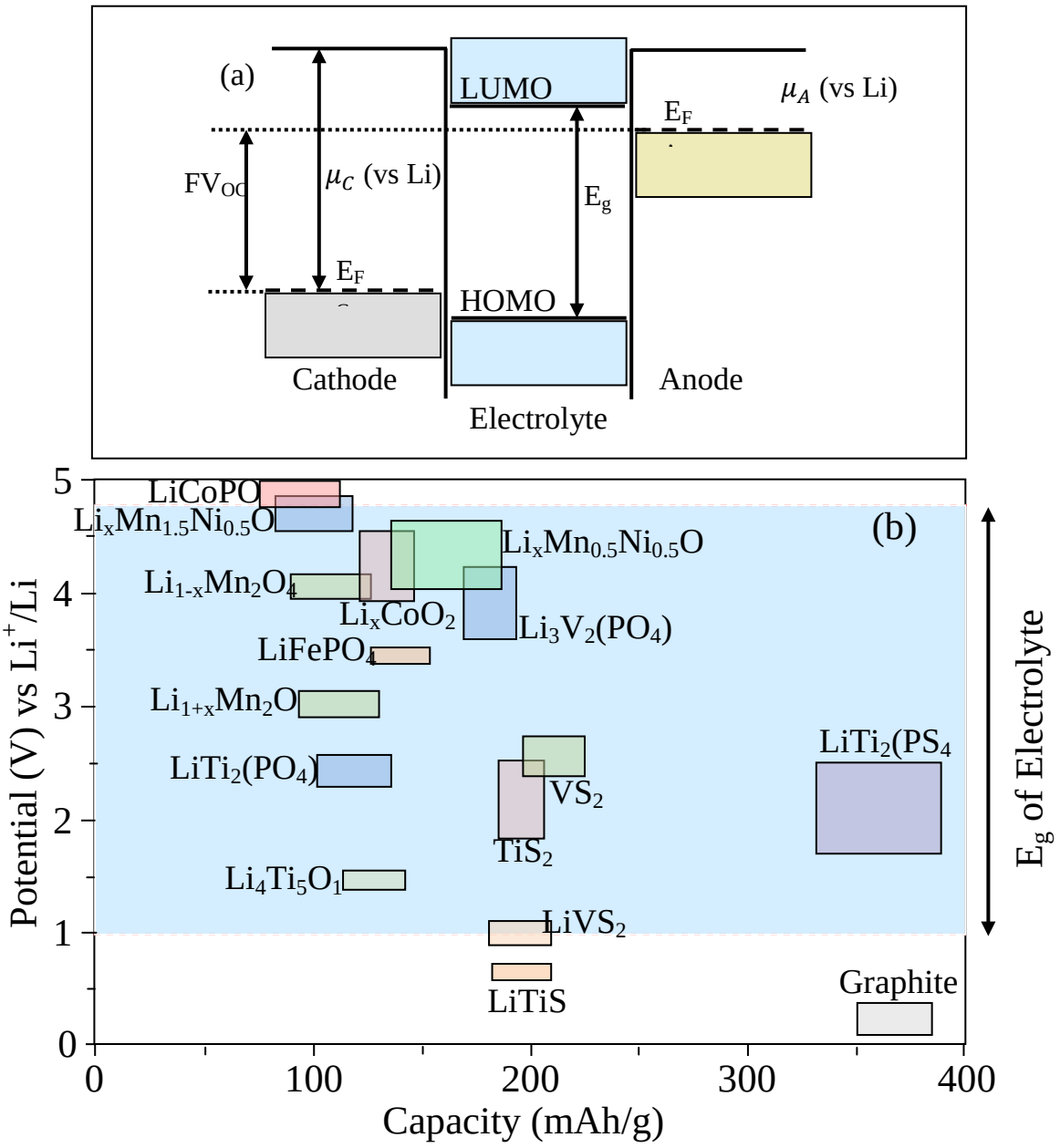

Figure 2.2: (a) Thermodynamic stability criteria of the electrolyte, (b) Selection criteria for electrode materials based on the thermodynamic stability criteria of the electrolyte [18].

The thermodynamic stability criterion for electrolyte is shown in Fig. 2.2(a) and Fermi energy level for different electrode materials in a typical non-aqueous electrolyte system is shown in Fig. 2.2(b).

2.2.3 Battery Materials

2.2.3.1 Anode and Electrolyte

For the anode, mostly carbon based materials are used, but some other materials like lithium foil, Si [19], Si-C composite [20-22], SnO_2 [23], $Li_4Ti_5O_{12}$ [24-26] are also used for higher capacity, stability and better performance. Electrolyte systems for LIBs include lithium salts like $LiPF_6$ [27], $LiAsF_6$ [28], $LiClO_4$ [28], $LiBF_4$ [28], $LiCF_3SO_3$ [29] dissolved in organic solvents such as ethylene carbonate (EC) [28, 30], dimethyl carbonate (DMC) [30, 31], diethyl carbonate (DEC) [28], etc.

2.2.3.2 Cathode

Cathode materials include oxides, phosphates, sulpho-phosphates that can undergo oxidation and reduction during charge and discharge reactions. A very detailed discussion on cathode materials is published by M Stanley Whittingham [32]. Lithium transition metal oxide such as $LiCoO_2$ [5, 33-38], $LiNiO_2$ [9, 39, 40], $LiMn_2O_4$ [26, 30, 41-44], LiV_3O_8 [45], $Li(Ni,Mn,Co)O_2$ [8, 46], $Li(Ni_{0.8}Co_{0.15}Al_{0.05})O_2$ [6] etc, is a type of material that is very common in commercial LIBs. $LiCoO_2$ is one of the successful commercial cathode materials, but still it has some issues that make it less attractive. $LiCoO_2$ is not very stable at overcharged condition as cobalt dissolution in the electrolyte is believed to happen at a high potential [34]. Also a sharp change in the lattice parameters with lithium intercalation [35] causes stress and micro-cracking of the electrode materials [47]. In addition, cobalt in $LiCoO_2$ is expensive compared to other transition metals such as nickel, manganese, iron, etc. Another transition metal oxide $LiNiO_2$ has higher energy density [48] than $LiCoO_2$, but is less stable [39] and less ordered material [40]. $LiMn_2O_4$

[26] has also been attempted as cathode material which is safer and cheaper than $LiCoO_2$, but shows less capacity. V_2O_5 [49] and LiV_3O_8 [50] are also used as cathode materials. They show higher capacity but lower voltage (3 V or less).

Another class of cathode materials is $LiMPO_4$ [51] with olivine structure which includes $LiFePO_4$, $LiMnPO_4$ [52], $LiCoPO_4$ [53], $LiMn_{0.25}Fe_{0.75}PO_4$ [54, 55], $LiFe_{1-x}Co_xPO_4$ [56], and $Li_3V_2(PO_4)_3$ [57] etc. In this class, $LiFePO_4$ is the most promising one.

Some cathode materials might decompose at overcharge condition or at elevated operating temperatures and these reactions are exothermic which eventually cause the battery temperature to rise. This higher temperature promotes the reactions of cathode materials with non-aqueous solvents (EC, DMC, PC etc) which generate more heat and the temperature continue to rise and eventually at some point the battery might fail and explode and fire hazard can be created. This situation is called the thermal runaway. The thermal property of some cathode materials is compared in Fig. 2.3 [58] and from this figure, it is observed that $LiFePO_4$ and $LiMn_2O_4$ are two most safe cathode materials. Besides, $LiFePO_4$ is cheap and most safe material and this is one good reason that people are motivated to study $LiFePO_4$.

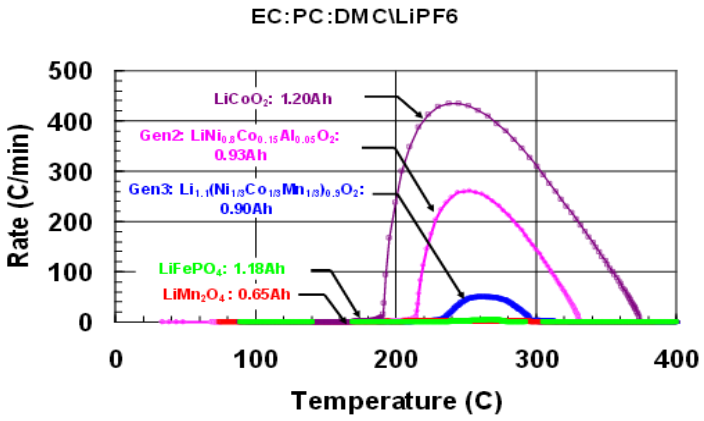

Figure 2.3: Comparison of thermal runaway properties of different cathode materials for LIBs [58].

2.3 $LiFePO_4$ Materials

Olivine type $LiFePO_4$ was first described as the battery electrode material by Professor Goodenough [4]. It is relatively cheap, has very stable potential plateau (3.5 V vs Li^+/Li theoretically) during discharge [59-61], and theoretical capacity of 170 mAh/g [4, 62] and good stability against thermal runaway [63]. Moreover it is observed in Fig. 2.2(b) that $LiFePO_4$ material is stable in the electrolyte potential window according to the thermodynamic stability criteria. Apart from having all attractive properties, its intrinsic electronic conductivity is very poor which is of the order of 10^{-9} S/cm^2 [32]. Several strategies have been adopted to increase the conductivity of $LiFePO_4$ such as conductive carbon coating [64-68], particle size reduction [48], metal powder addition [69, 70], doping with supervalent ions [65, 67, 71, 72], etc.

2.3.1 Structure of $LiFePO_4$

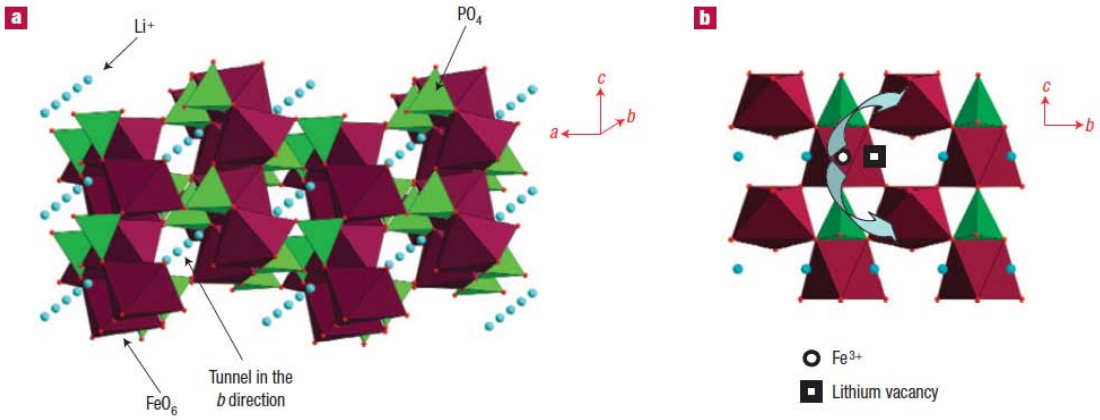

Figure 2.4: a) Crystal structure of $LiFePO_4$, b) a layer of $LiFePO_4$ which consists of FeO_6 octahedra and PO_4 tetrahedra [73].

$LiFePO_4$ is an olivine structure (*Pnma*) with an orthorhombic unit cell. The crystal structure can be better explained with the help of the illustration in Fig. 2.4. $LiFePO_4$ structure has some parallel sheets made of FeO_6 octahedra which have corner sharing

connections to each other. These $[FeO_4]_n$ sheets are parallel to 'bc' plane which connect to other $[FeO_4]_n$ sheet with the help of PO_4 tetrahedron along 'a' direction making a 3D structure which has lithium tunnel parallel to the 'b' direction. PO_4 tetrahedron has a common edge with FeO_6 octahedron. Fig. 2.4(a) shows the 3D structure of $LiFePO_4$ and the individual $[FeO_4]_n$ sheet is shown in Fig. 2.4(b). Lattice parameters of $LiFePO_4$ (discharged state) are *a*=10.3375 Å, *b*=6.0112 Å, and *c*=4.6950 Å [74] and the lattice parameters for $FePO_4$ (charged state) are *a*=9.7599 Å, *b*=5.7519 Å, and *c*=4.7560 Å [74].

2.3.2 Thermodynamics of $LiFePO_4$

Thermodynamics of a two-phase system is introduced here to illustrate the two-phase transformation phenomenon. Gibbs free energy versus composition plot is shown in Fig. 2.5. At room temperature the free energy curves of both α ($FePO_4$) and β ($LiFePO_4$) have minima at some particular compositions as shown in Fig. 2.5. In the composition range from α_e to β_e, the criterion that requires minimum Gibbs free energy of the system leads to a two-phase mixture typically at room temperature.

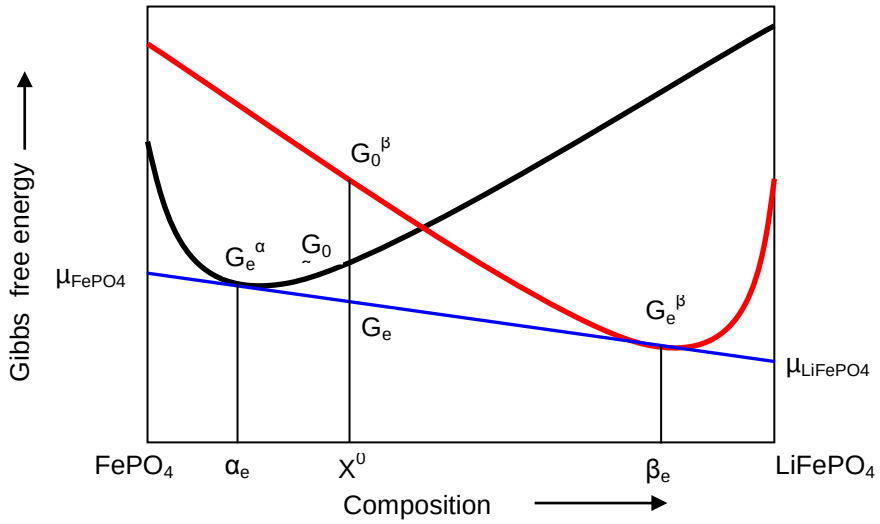

Figure 2.5: Schematic representation of Gibbs free energy with the Li ion content and associated two-phase mixture region.

During discharge of a LIB, Li ions diffuse into the $FePO_4$ particles and after reaching the composition of X_1 in Fig. 2.6 the two phase mixture appears and it continues until the composition X_2 is achieved. Chemical potentials are obtained from the common tangent of the Gibbs energy curves (Fig. 2.5). Equilibrium potential of the battery can be calculated according to the Eq. 2.1 where $\mu_{Li(c)}$ and $\mu_{Li(a)}$ represent the chemical potentials of the cathode and anode materials respectively. Anode material is usually a single phase material throughout the Li ion intercalation and hence the chemical potential is usually constant. Chemical potential of the cathode material is plotted in the upper part of Fig.2.6 and thermodynamic battery potential (OCV) derived from the Gibbs free energy curve is placed in the bottom part of the Fig. 2.6 which was described by Eq. 2.1.

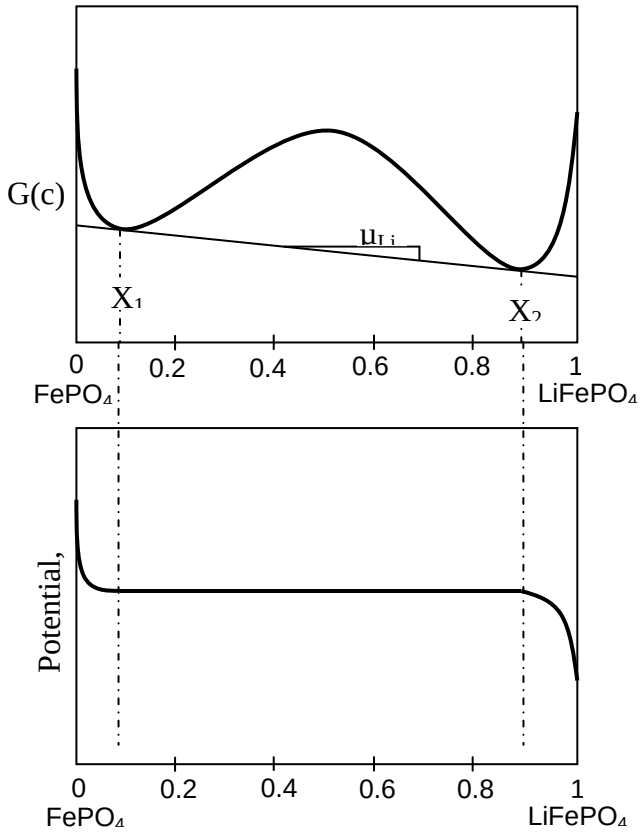

Figure 2.6: Schematic representation of Gibbs free energy of the α-β two-phase system and associated potential profile during discharge.

2.3.3 Phase Transition Models

During discharge, Li ion diffuses into $FePO_4$ (Heterosite) particles which transforms into a new phase $LiFePO_4$ (Triphylite) and during the charge process the reverse phase transition takes place. This phase transition relies on diffusion of Li ions through the crystal structure of active materials. Diffusion of Li ions through the $LiFePO_4$ structure is not isotropic but anisotropic along the preferred 'b' direction [73]. This makes Li ion diffusivity higher along the 'b' direction [73] which is due to the 1D tunnel shown in the structure of $LiFePO_4$ in Fig. 2.4. This anisotropic Li diffusion makes the phase transformation more complicated. Several phase transition models such as core-shrinking model [4, 75], domino-cascade model [73], mosaic model [76, 77], mushy zone approach [7], single phase kinetic model [78] have been postulated by different research groups to describe phase transition phenomena of LiFePO4 materials. And in many aspects these models somehow contradicts with each other which will be highlighted in next few sections. The two-phase models can be broadly categorized into two groups such as the core-shrinking model and domino-cascade model which will be discussed in detail in the following sections.

2.3.3.1 Core Shrinking Model

One of the pioneering works regarding phase transformation study of $LiFePO_4$ particles was done by Venkat Srinivasan and John Newman [75] which is known as the so-called core-shrinking model or core-shell model. This model was first proposed by Padhi et. al. [4] and later was advanced by Srinivasan and Newman [75], and L Laffont and C Delacourt et. al. [79].

Venkat Srinivasan and John Newman considered phase transformation in spherical particles. Their approach is schematically illustrated in Fig. 2.7. During discharge, Li ions diffuse into the particles starting from the surface which initially creates

Li_yFePO_4 where y is a very small value. Then a thin shell of $Li_{1-x}FePO_4$ is formed where x is close to zero which is a distinctively different phase than the initial $FePO_4$ phase. With continuing discharge (Li intercalation), the shell continues to grow until the whole particle becomes $Li_{1-x}FePO_4$ and later on completely transforms into $LiFePO_4$ at the completion of discharge. So, initial single phase transforms through a two-phase system with diffusion of Li ions through a thin moving interface. During the charge, the Li diffusion direction reverses causing a Li-poor shell and Li-rich core where the shell grows inward to finally form $FePO_4$.

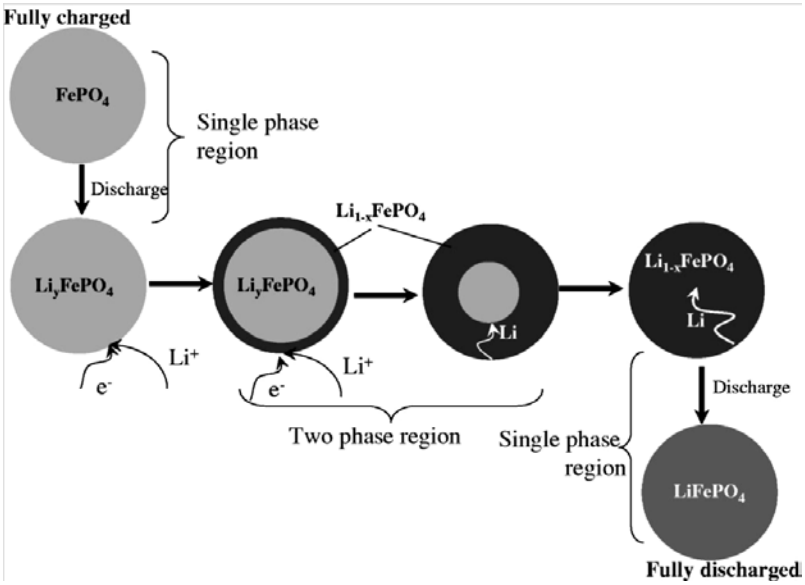

Figure 2.7: Illustration of the shrinking-core model during discharge. [75]

The key attributes of this core-shell model or core-shrinking model are as follows:

1) The phase transition in any particle continues throughout the entire charge or discharge process. The progress of the phase transition is gradual and continuous.

2) During discharge, the phase transition starts from the outer surface of the particle and moves inward and a distinctive two-phase interface separates the two end members ($LiFePO_4$ and $FePO_4$). The existence of this two-phase interface together with the coexistence of two end members in one particle was experimentally validated by several research groups [80, 81].
3) In the process of charge and discharge, a certain level of solid solubility is predicted between the two end members. In other words, end members of composition Li_xFePO_4 and $Li_{1-x'}FePO_4$ (x and x' have small values close to zero) are predicted.

Although this core-shrinking model gives insight of the process, it didn't necessarily assume all the parameters realistically or in other words it has some inherent limitations. The major limitations include:

1) It did not include kinetically induced effects; so it cannot predict the non-equilibrium phase transformation behavior at higher discharge rates.
2) It did not include the physics that the Li diffusion through the two-phase interface is significantly sluggish [82].
3) It uses isotropic diffusion of Li ions. But Li ion diffusivity has significant different values along different crystallographic directions [51, 83].
4) It did not study the particle shape and size effect on the phase transformation behavior.

2.3.3.2 Domino Cascade Model

C Delmas, et.al studied the phase transformation behavior of $LiFePO_4$ using a model which they call domino-cascade model [73]. In this model they considered the anisotropic Li ion diffusion through the $LiFePO_4$ lattice where Li ions have a preferentially

high diffusion coefficient along the 'b' direction. They found that once the de-lithiation starts, the change in the charge of Fe ions causes the strong change in the Fe-O and O-O bond lengths in the FeO_6 octahedra which leads to structure distortions. Since FeO_6 octahedron and PO_4 tetrahedron shares a common O-O edge, the change in O-O bond length also affects PO_4. These changes in FeO_6 and PO_4 environments make it difficult to introduce a significant amount of Fe^{3+} ions in $LiFePO_4$ and a significant amount of Fe^{2+} ions in $FePO_4$ and hence a large compositional domain for solid solutions is not possible. As a result, a two-phase mixture of two end-members [$Li_{1-\varepsilon}FePO_4$ (ε~0) and $Li_{\varepsilon'}FePO_4$ (ε'~0)] exists during the charge-discharge process. When the de-intercalation starts a small polaron of Fe^{3+} forms [84] (similar phenomenon happens for Fe^{2+} when lithiation takes place) and the change in the environment of FeO_6 and PO_4 push this polaron to next FeO_6 octahedron. Thus with the lithium de-intercalation along the '*b*' direction a two-phase interface moves along the '*a*' direction which as shown in Fig. 2.8.

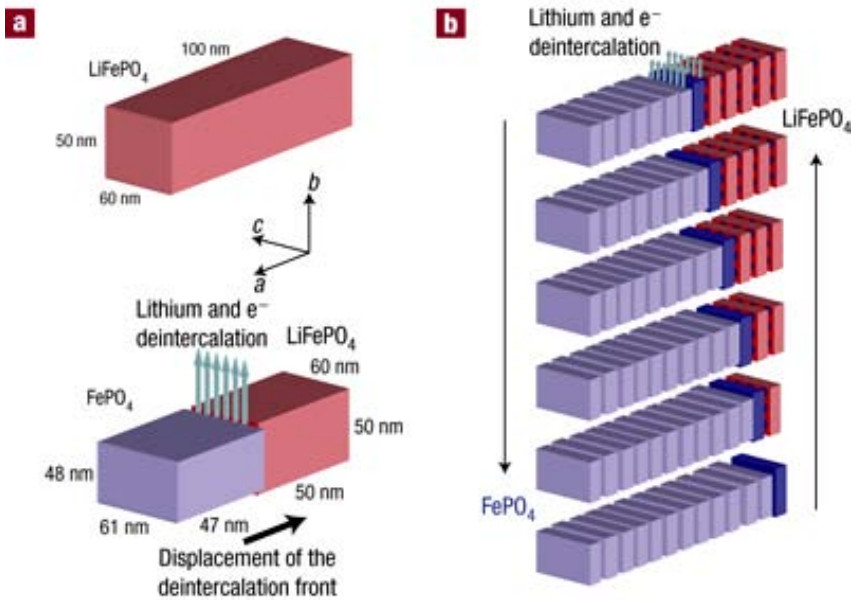

Figure 2.8: Schematic view of the 'domino-cascade' mechanism for the lithium de-intercalation /intercalation mechanism in $LiFePO_4$ crystallites [73].

Due to the large difference in bond lengths and angles between $LiFePO_4$ and newly formed $FePO_4$ block, strong distortions appear locally that causes instability to the adjacent $[FeO_4]_n$ layers. This results in the easiness to remove lithium ions from the *b* tunnels adjacent to newly formed $FePO_4$ block instead of starting a new nucleation site to form a new $FePO_4$ block elsewhere in the same particle. Rather nucleation of a new $FePO_4$ block within the same crystal particle requires higher activation energy whereas lithium de-intercalation adjacent to the already formed $FePO_4$ block can proceed without the increase of activation energy. So, once the intercalation or de-intercalation starts in any particle, it finishes very quickly for that particle. But chemical and electrochemical lithiation/de-lithiation can give different pictures. Chemical intercalation/de-intercalation obviously has the tendency to nucleate simultaneously at different points within one crystal particle and hence forms the domains of two phases ($LiFePO_4$ and $FePO_4$) in one single crystal [79, 81].

Key attributes of the domino-cascade model are as follows:

1) Once the phase transition starts in any particle, it finishes very quickly in that particle. In one particle, phase transition does not continue during the entire period of the discharge process of the cell. Depending on the discharge rate, some particles with good electronic conductivity, having access to the Li ions get activated for phase transition while some other particles might not be activated for transition.
2) During the phase transition, only two end members ($LiFePO_4$ and $FePO_4$) are present as the unique structure of $LiFePO_4$ and $FePO_4$ permits almost no solid solubility, if not, very limited solubility. Once Li ions enter $FePO_4$ structure (vice versa), distortion in local crystal structure causes

the entire structure transforms into $LiFePO_4$ very quickly permiting very limited solulibility of Li ions.

2.3.3.3 Comparison between phase transition models

The phase transition models are summarized in the schematics of Fig. 2.9 [85]. The classical core-shrinking model proposed by Padhi et. al [4] and further advanced by Srinivasan and Newman [75] considered isotropic Li ion diffusion (Fig. 2.9(a)). The 'radial core shell model' is a version of core shrinking model but considers anisotropic Li ion diffusion along '*b*' direction and in this model it is assumed that during lithiation the Li ion intercalation starts from the surface of the particles and during de-lithiation the Li ion de-intercalation starts from the middle of the particles (Fig. 2.9(b)). Domino-cascade model uses the anisotropic Li ion diffusion along '*b*' direction, and once transition starts in a particle it very quickly finishes in that particle (Fig. 2.9(c)). Another model, which can be described as a spinodal decomposition model (Fig. 2.9(d)), predicts that a new phase can nucleate at any crystal defects and at any intermediate stage of charge or discharge. It also predicts that one particle can have many domains of both phases and the second phase can be found isolated inside the mother phase. Among these models, only domino cascade model predicts that at any stage of charge or discharge, some particle can be found which has completed the phase transition while some other particles might not even start transforming. Other models predicts the continuous and gradual phase transition progress during the entire period of charge or discharge.

2.3.4 Experimental techniques to study Phase Transition of $LiFePO_4$

Various techniques have been employed to study the phase transition of $LiFePO_4$ materials to date. To study the Li ion insertion behavior, different research groups used either chemical [60, 79-81, 86-91] or electrochemical [76, 85, 90, 92-101] lithiation/de-lithiation processes. Besides probing these phase transition was attempted using both

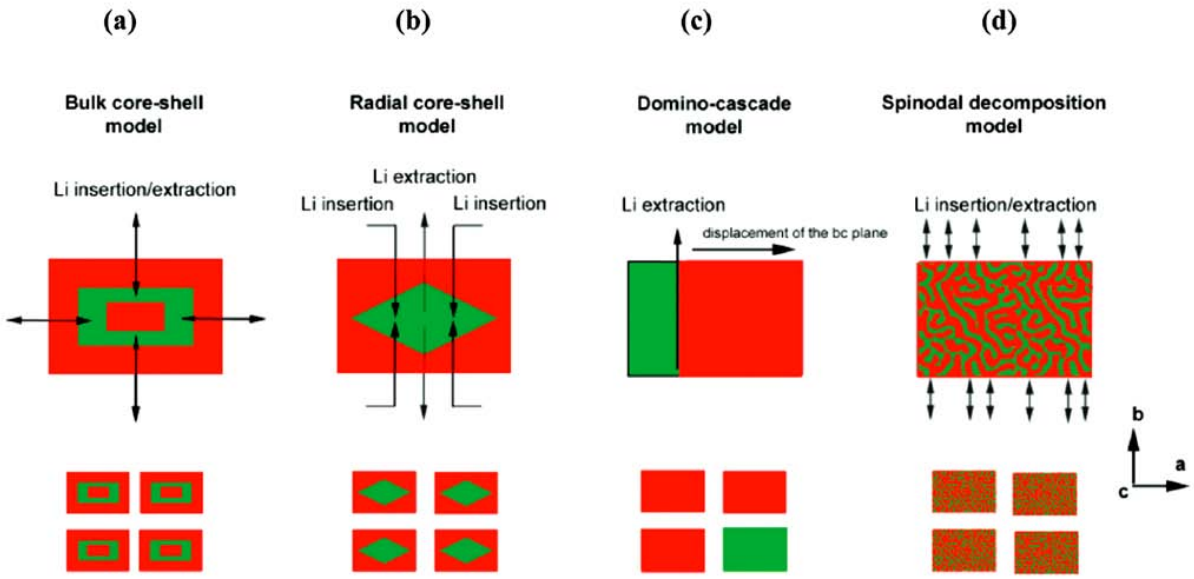

Figure 2.9: Schematic representations of the $LiFePO_4$ (in red) and $FePO_4$ (in green) phases in the four models proposed in the literature for the Li insertion/extraction mechanisms in $FePO_4$ /$LiFePO_4$ materials: (a) bulk core shell model, [4, 103] (b) radial core shell model, [79] (c) domino-cascade model, [73] and (d) a 4^{th} model that can be called as the spinodal decomposition model freely schematized from ref [80]. In all of the models, except the domino-cascade model, the particles are mixed and composed of the two phases [85].

ex-situ [60, 79-81, 85-89, 91, 93, 94, 97, 99] and in-situ [76, 90, 95, 96, 98, 100-102] methods. Because of these variations of the lithiation/de-lithiation processes and the data recording methods, observation and conclusion about the phase transition mechanism for $LiFePO_4$ materials varied widely. Various types of characterization tools have been employed by the researchers to probe the phase transition phenomena and to characterize the phase boundary and phases present during the lithiation/de-lithiation process. Among them, the use of Transmission Electron Microscopy (TEM/HRTEM) [81, 85], Raman spectroscopy [80, 91, 102], X-ray Diffraction (XRD) [80, 91, 95, 97, 98, 100,

101], Electron Energy Loss Spectroscopy (EELS/HREELS) [79, 85, 87], Valence Electron Energy Loss Spectroscopy (VEELS) [88], Mossbauer Spectroscopy [86, 100], X-ray Photoelectron Spectroscopy (XPS) [94], Neutron Powder Diffraction (NPD) [60, 76, 86], X-ray Absorption Spectroscopy (XAS) [90, 91, 96, 98, 101], X-ray Absorption Near Edge Structure (XANES) [96], Scanning Transmission Electron Microscopy (STEM) [89], High Angle Annular Dark Field Scanning Transmission Electron Microscopy (HAADF-STEM) [89], Annular Bright Field Scanning Transmission Electron Microscopy (ABFSTEM) [99], Precession Electron Diffraction (PED) [85] etc. has been reported so far. They used active materials of different particle sizes and morphologies. A comparative study on use of different characterization tools is done by Corey T Love et. al. [96]. The key findings from these experimental characterizations can be listed as follows.

1) Domains of two end members (Li-rich phase and Li-poor phase) coexist in one particle separated by an interface. This was observed in the ex-situ experiments on chemically lithiated/de-lithiated particles [79-81, 86, 87].
2) Interface between the two end members are observed. The interface was found because of the existence of a mixture of two end members but not a solid solution [79]. HRTEM also captured a disordered interface (not amorphous) in an ex-situ experiment of chemically de-lithiated large plate shaped $LiFePO_4$ particle [80, 81]. Using HREELS from the ex-situ experiments, the interface is found to be approximately 8-15 nm wide in a partially chemically de-lithiated plate shaped particles.
3) Some theoretical study and models predicted that the interface between the two end members moves along '*a*' direction of the orthorhombic crystal structure during the progress of phase transition. HRTEM study in

an ex-situ experiment of partially de-lithiated large plate shaped $LiFePO_4$ particle [81] and XPS study [94] on samples of electrochemically lithiated/de-lithiated at different state of charge-discharge also were able to capture this phenomenon. One dimensional movement of interface was also recorded using kinetic study and analyzed with the Avrami-Johnson-Mehl-Errofev equation [92, 104].

4) Domino-cascade model [73] predicted at any stage of charge or discharge, electrode consists of a mixture of fully lithiated particles and completely de-lithiated particles. In one particle two end members does not coexist. This is also supported by ex-situ study on electrochemically de-lithiated $LiFePO_4$ particles using HRTEM and PED [85].
5) Two end members were identified as $Li_{0.89}FePO_4$ and $Li_{0.05}FePO_4$ at room temperature from ex-situ neutron diffraction data from approximately 100 nm particles [60]. Smaller particles have higher solid solubility [92, 105] at room temperature and can even be one single phase of composition $LixFePO_4$ (x can have any value within 0 and 1) for less than 15 nm particles [105] for the entire period of charge/discharge process. In other words, the miscibility gap between the two end members during charge/discharge process can completely disappear at high temperatures for $LiFePO_4$ particles below certain critical size.
6) Usually the LIBs containing $LiFePO_4$ material are charged/discharged within the potential window of 2.5 V to 4.2 V. But if it is deeply discharged to 0.75 V or so, below 1.5 V the battery gives a slopping (reducing or increasing during discharge and charge respectively) potential profile

which indicates the absence of any two-phase system and one solid soluble phase [16].

2.4 Scope of study and objectives

It is already discussed that phase transition between $LiFePO_4$ and $FePO_4$ gives a flat plateau of potential during charge or discharge and at the particle level understanding of the detailed mechanism of this phase transition is very important to overcome the high rate charge/discharge barrier and also to optimize the battery design for various applications including hybrid electric vehicles. So far the observation of phase transition phenomena is contradicted by different phase transition models and also by experimental observation using a range of different characterization tools and experimentation methods. Based on all the information presented here, the phase transition of $LiFePO_4$ material needs to be studied in more detail and hence the objectives of this study are listed as follows.

1) Synthesize highly crystalline $LiFePO_4$ materials and characterize them using different tools such as particle size analyzer, XRD, SEM, electrochemical tests, etc.
2) Since chemical lithiation/de-lithiation and electrochemical lithiation/de-lithiation gives different observation and in a real working battery electrochemical lithiation/de-lithiation takes place, it is critical to study $LiFePO_4$ materials through in situ electrochemical test.
3) In-situ experiment gives real time information from a working battery and in-situ study is always preferred over ex-situ experiments; therefore in-situ techniques were adopted herein to study the phase transition of $LiFePO_4$.

4) Phase transition of $LiFePO_4$ needs to be studied at different length scale such as at particle lever and at the bulk level, and hence the in-situ experiments were conducted at two distinctly different length scales. For example, in-situ XRD experiment in a traditional powder X-ray diffractometer can give the bulk-level phase transition information of $LiFePO_4$ but Raman spectroscopy could be used to probe very small electrode area so that particle-level phenomena can be studied.
5) To better understand the phase transition of $LiFePO_4$ at the particle level, numerical study will be conducted to understand the effect of particle size and particle morphology on phase transition.

Chapter 3

Synthesis of LiFePO4 Particles and Li ion Battery Making

3.1 Introduction

Both synthesis of $LiFePO_4$ materials and LIB fabrication process need special care as it requires the special inert atmosphere. Electrode making process has to be tuned properly to obtain optimum electrode properties like porosity, conductivity, etc. and the battery has to be assembled in an argon filled glove box to protect from atmospheric oxygen and moisture. Special attention has to be paid to all these requirements to make a good performing LIB. In this chapter, synthesis of active $LiFePO_4$ material, their characterization, electrode fabrication using them, and finally battery assembly process is discussed in detail.

3.2 Synthesis of $LiFePO_4$

3.2.1 Solid State Synthesis

$LiFePO_4$ material has been synthesized using solid state synthesis method. In the beginning of the solid-state synthesis, the precursors such as Li_2CO_3 (Sigma-Aldrich), $FeC_2O_4.2H_2O$ (Sigma-Aldrich) and $NH_4H_2PO_4$ (Sigma-Aldrich) were mixed properly in a stainless steel container using ball milling for 1 hour. The precursor mixture was heat-treated at 350^oC in argon for 3 hours in a tube furnace. During the heat treatment, the precursor compounds decomposed and released H_2O, CO_2 and NH_3. After this step, the carbon coating precursor cellulose acetate (Sigma-Aldrich) was mixed with the decomposed mixture and was heated in a tube furnace at 700^oC for 8 hours under argon gas flow to get carbon coated crystalline $LiFePO_4$. The solid synthesis method is shown with the help of the flow diagram in Fig. 3.1.

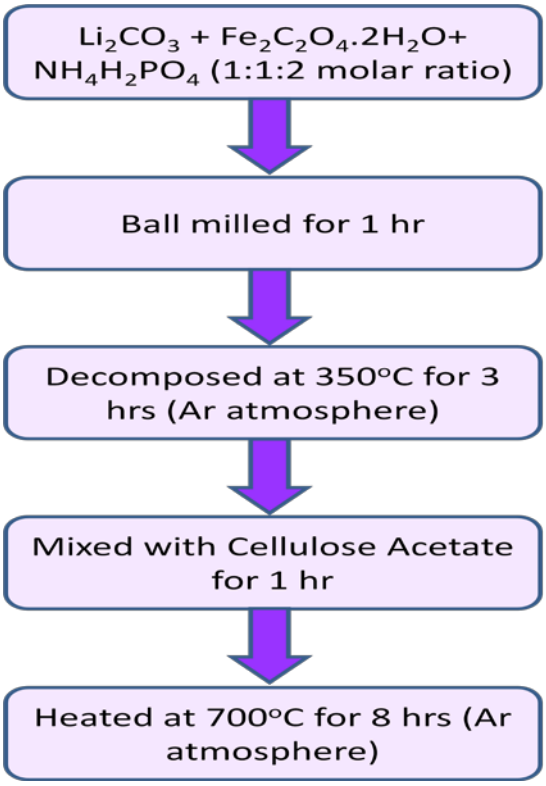

Figure 3.1: Flow diagram for solid state synthesis method to synthesize $LiFePO_4$ material.

3.2.2 Characterization

After synthesis, the routine characterization techniques like XRD, SEM, electrochemical test, etc. have been employed to study the material. X-ray diffraction test was done to confirm the phases of the synthesized material. Figure 3.2 shows the XRD patterns of the synthesized $LiFePO_4$ and the olivine structure (*Pnma*) was confirmed using the JCPDS card number 81-1173.

Particle size of the synthesized $LiFePO_4$ particles were determined using Nanosight Nanoparticle Tracking Analyzer and the result is presented in Fig. 3.3. The average particle size determined was approximately 222 nm while most of the particles were approximately 196 nm with a standard deviation of 74 nm.

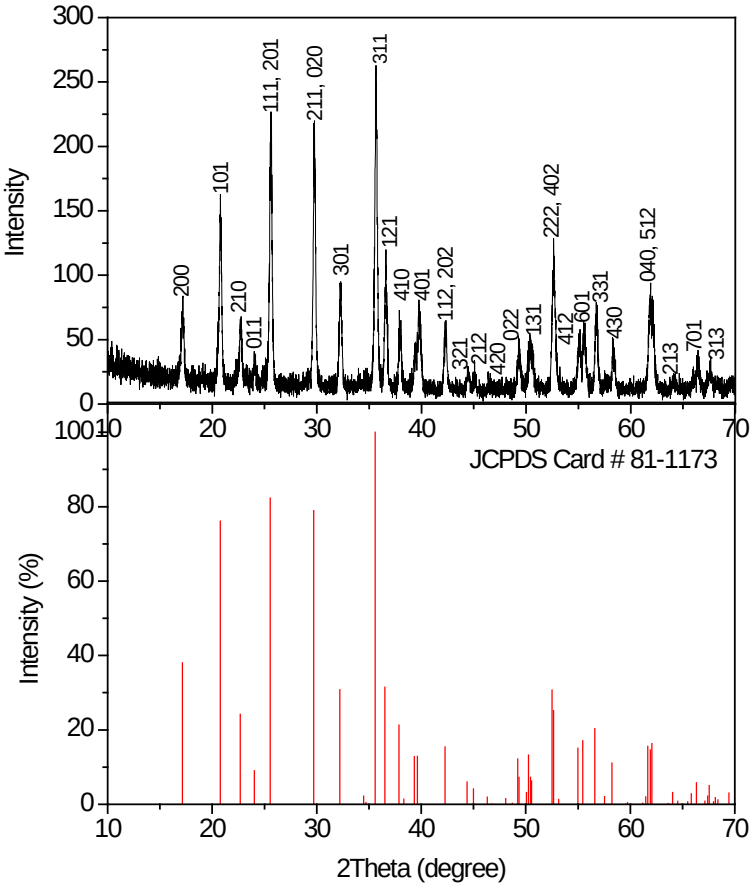

Figure 3.2: XRD patterns obtained from materials synthesized through solid state synthesis method. JCPDS card # 81-1173 is shown in bottom plot.

SEM image of the particles also give an indication of the particle size and also the particle morphology (Fig. 3.4). SEM study of the $LiFePO_4$ material was done using ZEISS Supra 55 Variable Pressure FE-SEM. Particles obtained through solid state synthesis route have an irregular shape as seen in SEM image (Fig. 3.4).

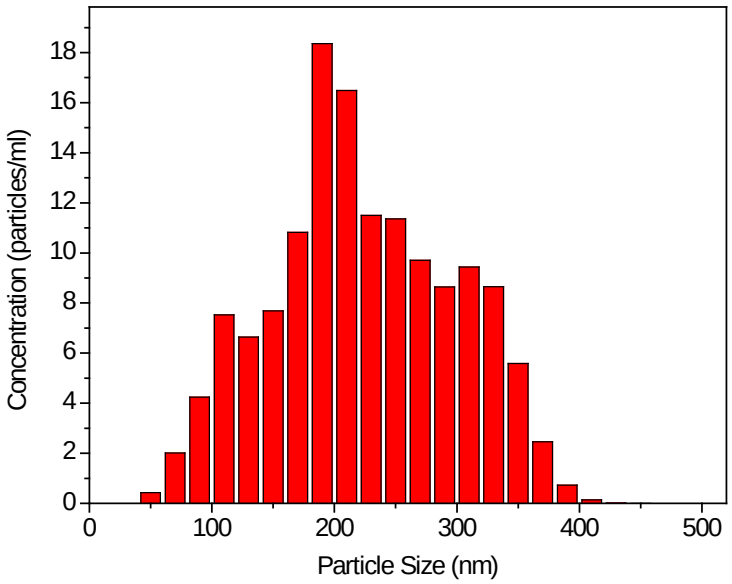

Figure 3.3: Particle size distribution of the synthesized LiFePO4 material at 700 ^{o}C for 8 hours.

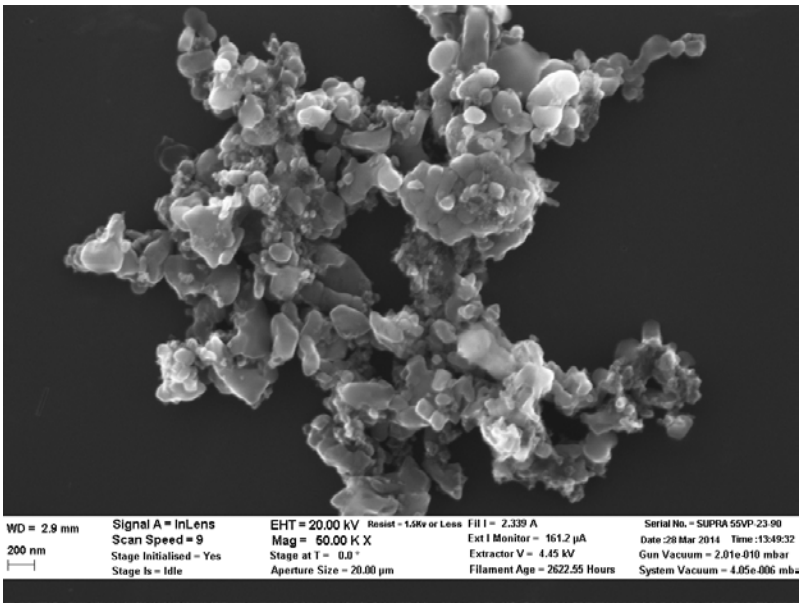

Figure 3.4: FE-SEM image of the solid state synthesized $LiFePO_4$ material at 700 ^{o}C for 8 hours.

3.3 Electrode Fabrication

To make the cathode, the first step is to make slurry containing the synthesized $LiFePO_4$ and additional conductive carbon. The steps of making electrode slurry are shown in Fig. 3.5. First, a glue was prepared e when binder PVDF (Polyvinylidene fluoride, Kynar HSV900, Elf Atochem) was dissolved in NMP (1- Methyl, 2-Pyrrolidinone, Acros Organics) at 50 ^{o}C. Then a mixture of carbon coated $LiFePO_4$ (C-$LiFePO_4$) and additional conductive carbon (Timcal Super P Li carbon) were slowly added to the glue under mixing using a magnetic stir bar on a hot-plate. After the whole mixture is added to the glue the rotation speed was adjusted to the 800 rpm and the mixing continued for 12 hours at 50 ^{o}C. The composition of cathode mixture varies in the study; one typical composition was 70% C-$LiFePO_4$, 20% conductive carbon, 10% PVDF binder. The amount of liquid NMP is also important and it has to be optimized for particular conductive carbon to get the right viscosity for coating on current collectors using a doctor blade. If the surface area of conductive carbon is high, more liquid NMP is required.

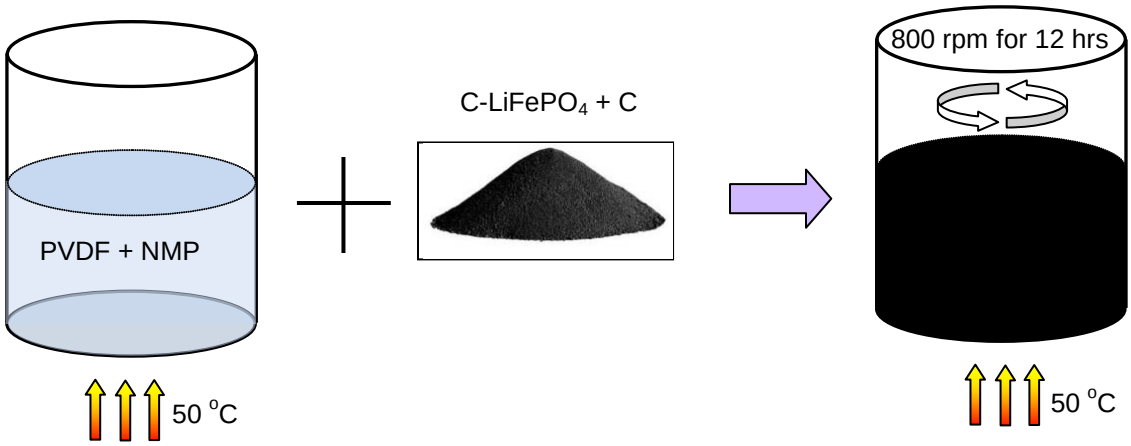

Figure 3.5: Schematic of slurry making process containing active material and conducting carbon.

By the time the slurry is being prepared, the current collector Al foil has to be ready to be coated by active material slurry. A piece of highly pure Al foil (Li ion battery grade) was cut and attached on a flat glass plate. The surface of the Al foil that will be coated by the active material slurry was pre-coated with a thin coat of graphite by rubbing a graphite bar on Al foil. This graphite layer later on acts as a solid lubricant during pressing the electrode after drying. Without this graphite layer, once the coating of active material is pressed to obtain a porous but dense continuous conductive network of

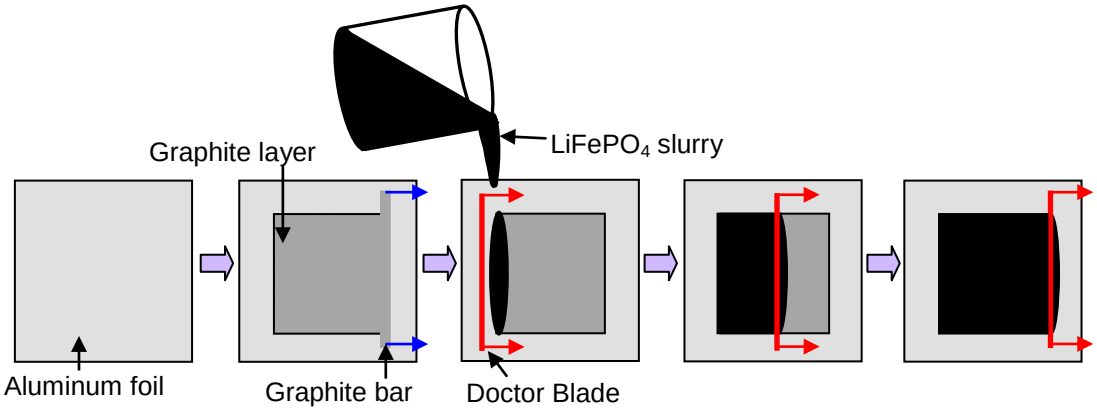

Figure 3.6: Schematic of electrode (cathode) fabrication process where doctor blade is used to coat $LiFePO_4$ slurry on Al current collector.

carbon, the coating tends to be peeled off from the Al current collector. After applying the thin graphite layer, the mixed C-$LiFePO_4$ slurry was poured on the graphitized area of the Al foil with the help of a doctor blade while the slurry was coated. The blade gap used typically for the experiments is approximately 350 µm and after drying and pressing the active material coating thickness became approximately 50 µm. The steps of slurry coating are shown in Fig. 3.6. After the coating was done, it was dried in an oven at 80 ^{o}C for 30 minutes. The cathode was then dried in a vacuum oven at 120 ^{o}C for 12 hours after the primary evaporation of liquid NMP at 80 ^{o}C. An appropriate size of the cathode

was then cut and pressed using 2 ton/cm^2 pressure before being used as a cathode. Cross sectional SEM image of a dried and pressed cathode is shown in Fig. 3.7.

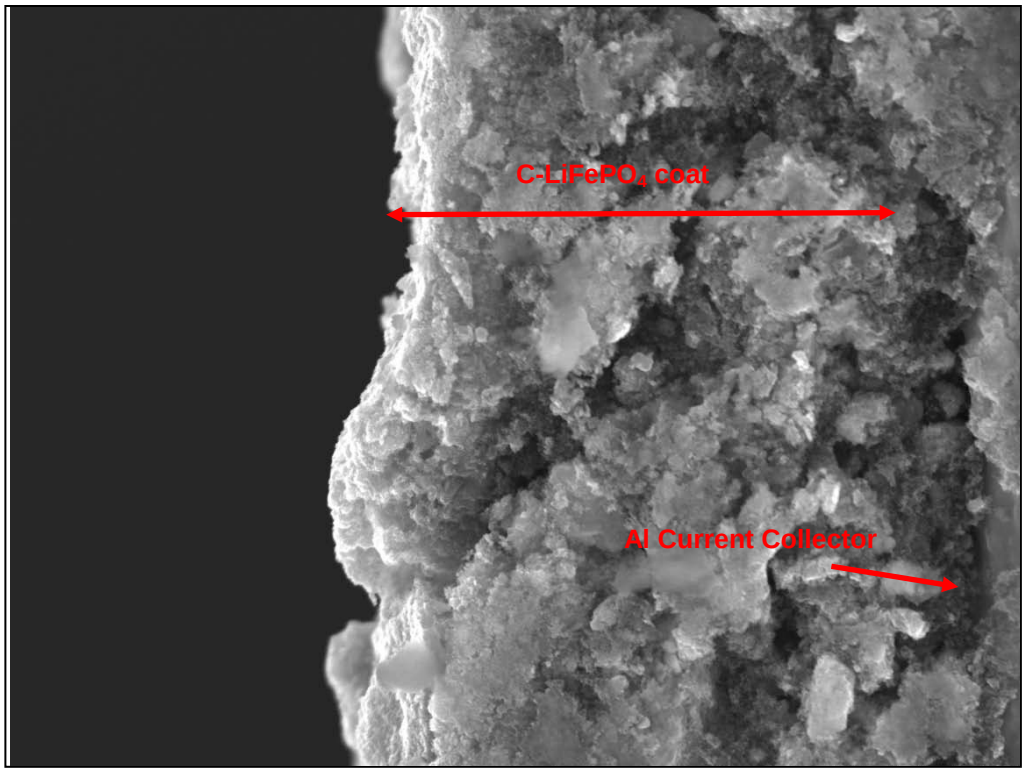

Figure 3.7: SEM image of a cathode containing 70% C-LiFePO$_4$, 20% Conductive carbon and 10% PVDF binder.

Anode used for the battery for later experiments is lithium ribbon. Lithium ribbon was cut and cleaned to remove the thin oxide layer by scratching them off and exposing fresh lithium metal surface inside an argon filled globe box. The cleaned lithium metal ribbon was then pressed against a precut stainless steel mesh. As the lithium metal is very soft, the steel mesh penetrated inside the lithium with pressure which established a very good electrical connection. This steel mesh was connected to an external potentiostat which was then electrically connected to the lithium anode.

3.4 Electrolyte Preparation

A 1:1 volume ratio of EC:DMC (Ethylene Carbonate, Di-methyl Carbonate) solvent system was used to prepare the electrolyte. EC is in a solid at room temperature and hence was melted and taken inside the argon filled glove box to prepare the electrolyte. The salt $LiPF_6$ which was dissolved in the solvent system is very sensitive to moisture and hence was only handled inside the glove box. After opening the $LiPF_6$ bottle, the solvent mixture was added immediately to minimize the exposure of LiPF6 to the atmosphere even though the glove box has very little moisture. 1M $LiPF_6$ solution was prepared to be used as electrolyte in all subsequent battery assembly processes.

3.5 Battery Assembly

For battery assembly, a home-built cell[106] was used which has a sealed glass cavity to house the cathode-separator-anode sandwich and electrolyte, with a sealant cap made of epoxy. All the battery assembly procedures were performed inside the argon filled glove box and also all the items including the cathode, separator, etc. that were taken inside the glove box were dried for at least 6 hours to ensure that they are moisture free. First, the cathode-separator-anode sandwich was inserted inside the glass cavity where the Celgard® 2500 separator was used and tested for any possible short circuit. If there was no shorting, the cathode and anode were connected with terminals inside the glass cavity which were then connected to the external stainless steel wires. Two small PTFE (poly tetrafluoro ethylene) wedges were used to push the cathode-separator-anode sandwich against the glass wall to ensure the least distance between the electrodes and hence to reduce the ohmic potential drop. Electrolyte was then added to the glass cavity to soak the separator and electrodes. Finally, the sealant cap was attached to protect the battery assembly. As the cell had the transparent glass housing, the battery was then

wrapped with some opaque Al foils to protect it from light which might degrade the electrolyte.

The assembled battery was kept idle for few hours and then subjected to the necessary electrochemical tests like cyclic voltametry (CV), impedance test, and most importantly galvanostatic charge/discharge tests. One such typical galvanostatic charge and discharge performance of a cell having a cathode of 70% C-$LiFePO_4$, 20% Conductive carbon and 10% PVDF binder is shown in Fig. 3.8. The second and third cycle of charge and discharge profile is presented in Fig. 3.8 where the columbic efficiencies are 93.5% and 93.9% which indicates the stability of the battery.

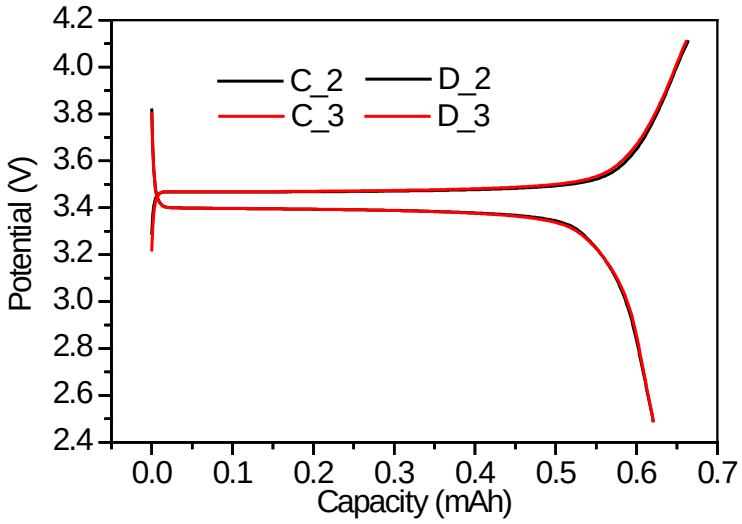

Figure 3.8: Galvanostatic charge discharge profile of a lithium ion cell. Cathode Composition is 70% C-$LiFePO_4$, 20% Conductive carbon and 10% PVDF binder. C_2 and D_2 indicate the 2^{nd} cycle charge and discharge profile while C_3 and D_3 indicate the 3^{rd} cycle charge and discharge profile.

Chapter 4

In-situ Studies using Raman Spectroscopy

4.1 Introduction

Although $LiFePO_4$ has so many attractive properties like stable potential during discharge, safe, and less expensive, the fundamental mechanism of Li transport during charge-discharge and the phase transition between two end members in $LiFePO_4$ is not fully understood. As has been already discussed in the previous chapters, two issues are controversial regarding the phase transition of $LiFePO_4$ material: one is the progress kinetics of the phase transition within a particle and the other is the existence of any possible solid solution with composition of $Li_{1-x}FePO_4$. So far, many phase transition theories/models have been proposed and many of them are supported by different experimental data as already discussed in Chapter 2. The different experimental techniques that are either ex-situ or in-situ, and the different type of intercalation/de-intercalation processes of Li ion that are either electrochemical or chemical lead to varied observations. Although in-situ experimentations have many practical challenges to obtain meaningful results with minimum errors, they are very crucial to get the real time phase transition information. At the same time, electrochemical intercalation/de-intercalation studies provided more comprehensive understanding of a real operating battery than chemical intercalation/de-intercalation study.

Raman spectroscopic technique has been used to study different battery components like electrolyte [107-110], carbon additive [111-114], carbon coating on the active material particles [115, 116], active material $LiFePO_4$ [117, 118], and other electrode components [37, 44, 113, 117, 119, 120] as well. If electrochemical charge/discharge test can be performed together with Raman spectroscopy, the result

can be more meaningful as the results come from a real working battery. So in this work the in-situ Raman spectroscopy was performed while a battery is being charged/discharged to study the phase transition phenomena of $LiFePO_4$ material. As the Raman laser spot size is around 2µm, it can practically study particle-level phase transition process. In this chapter, the detailed experimentation technique for in-situ Raman spectroscopy of a LIB containing $LiFePO_4$ material and the associated phase transition results during different rate charge and discharge process have been discussed.

4.2 Design of Battery Casing

LIBs require a sealed container to house the components so that they are protected from the atmospheric moisture and oxygen as has already been mentioned in Chapter 3. To assemble a battery to be used in the in-situ Raman spectroscopy, additional design requirements have to be considered to allow the Raman laser access the active material of the electrode to be studied. To do this, a Raman laser transparent window has to be installed at the positive electrode side of the battery.

Figure 4.1 shows the design of the transparent cell housing and experimental setup for the in-situ Raman study. The cell housing was made of an airtight cavity of glass as the electrolyte reservoir, an epoxy connector, and a sealing cap. The conductive terminals of the cell were made of stainless steel for both the cathode and anode.

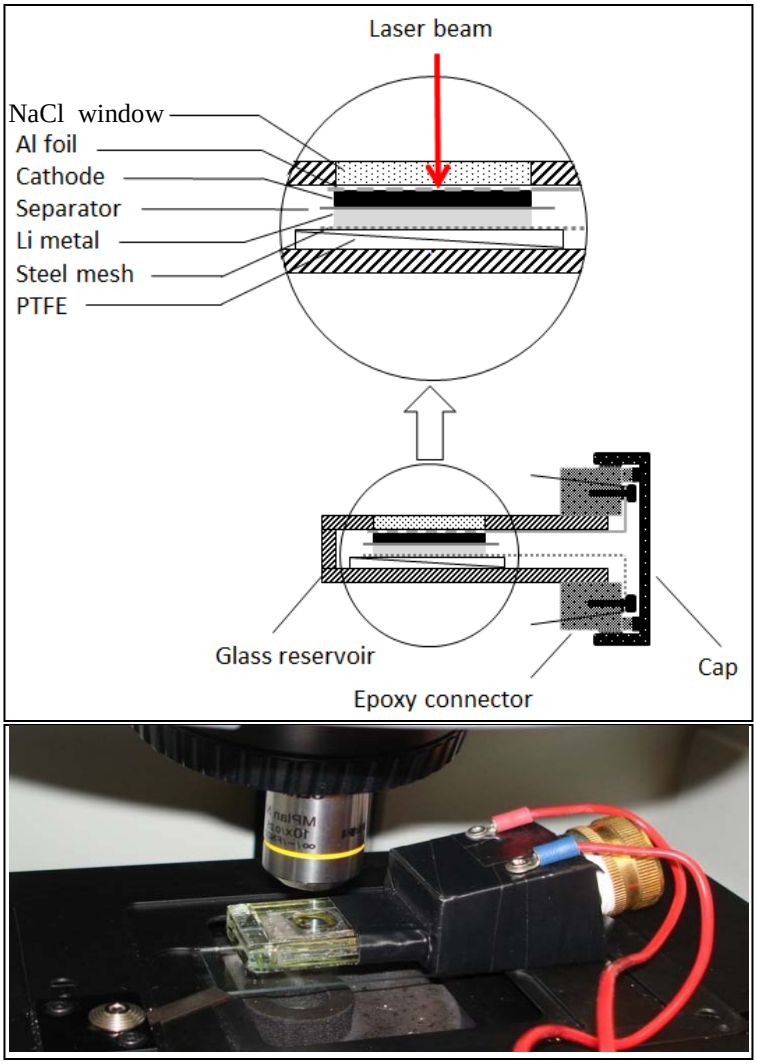

Figure 4.1: Schematic of the cell design for in-situ Raman spectroscopy. The real working cell operating in the Raman spectrometer sample holder is shown in the bottom.

This cell configuration prevents the cathode surface to be covered with an excessive amount of electrolyte. This feature consequently facilitates deeper penetration of the laser beam and therefore improves detection of chemical changes on the cathode surface. A NaCl single crystal (Edmund Optics) used as the transparent window for the

laser pathway not only minimizes laser intensity loss but also has well-defined Raman signatures that do not overlap with signals from the battery materials.

4.3 Electrode Fabrication and Battery Making

4.3.1 Electrode Fabrication

Electrodes for in-situ Raman study are different comparing to the electrodes that are used in the normal Li-ion batteries. The positive electrode in normal batteries has active material ($LiFePO_4$) coated on the current collector (Al foil) and the side with active material coated faces towards the separator and the negative electrode (anode) in a working battery. But with this configuration it is not possible to study using the in-situ Raman spectroscopy because the current collector (aluminum foil) blocks the active materials from being directly accessed by the Raman laser. So, the electrodes that will be used in the batteries for in-situ Raman study have active materials coated on a homemade aluminum mesh where small holes of the aluminum mesh will allow the Raman laser to interact with the active material. The hole size on aluminum mesh is approximately 0.5 mm and the Raman laser spot size is 2 μm which makes possible to study the material. And also, as the individual hole can be physically marked, it is possible to study the same spot if the experiment is discontinued. The preparation of this special kind of electrode is schematically shown in Fig. 4.2.

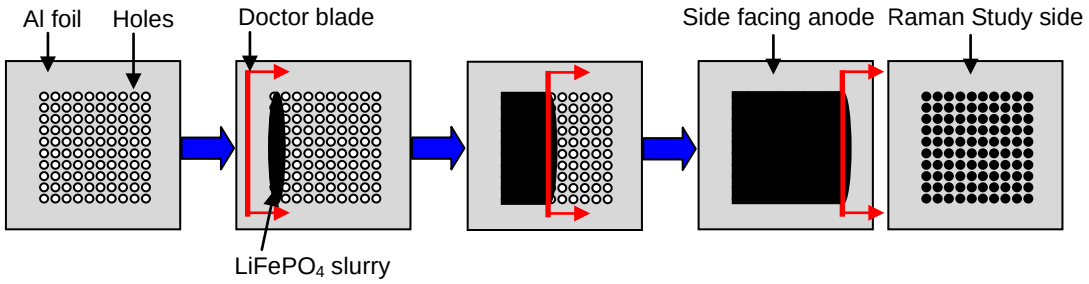

Figure 4.2: Schematic of the cathode making process specially suitable for in-situ Raman spectroscopy.

Active material slurry contains 90% C-$LiFePO_4$, 2% conductive carbon, 8% binder (PVDF). This slurry preparation is similar to the process described in Chapter 3. The slurry was then coated on the aluminum mesh (Fig. 4.2), dried in a vacuum oven at 120 ^oC and pressed with a 2 ton/cm2 pressure before being used in the in-situ Raman study. Finally, the electrode was cut to a size of 1.5 cm × 1.5 cm. Since the Raman laser interacts with the carbon (either carbon additives or carbon coating on $LiFePO_4$) in the electrode, some corrective measures were taken which will be described in section 4.3.4.

For the anode, an appropriate size (1.5 cm × 1.5 cm) of lithium ribbon was cut and pressed against a steel mesh, which acted as a current connector.

4.3.2 Battery Making

Positive electrode, separator, and the battery components were dried for 6 hours and then transferred to the argon filled glovebox to assemble the battery for the in-situ Raman study. 1M $LiPF_6$ solution with a solvent mixture of 1:1 (volume ratio) of DMC:EC was prepared inside the glovebox to be used as electrolyte for the battery. The anodic lithium, Celgard 2500 separator, and the specially fabricated cathode were assembled as a sandwich which was subsequently inserted inside the battery housing (Fig. 4.1) and then with the help of a multi-meter any possible short shorting was examined. If there was no shorting, a PTFE wedge was pushed beneath the anode side to bring the cathode closer to the Raman laser transparent window. Two electrodes were then attached to the external electrical connection and finally electrolyte was added to the electrode sandwich. After the electrodes and separator were soaked by the electrolyte for 30 minutes, extra electrolyte was drained to enhance the Raman signal from the active material. The sealant cap was finally attached properly before the battery was taken outside the glovebox for the in-situ Raman spectroscopy.

4.3.3 Raman Laser Interaction with battery components and Corrective measures

The purpose of this in-situ Raman study is to understand the phase transformation of $LiFePO_4$ materials. But to get the best results, Raman laser interaction with all the battery components has to be considered. Table 4.1 lists all possible Raman active vibration modes of $LiFePO_4$ materials and its de-lithiated phase $FePO_4$, and also other vibration modes for different battery components such as carbon and electrolyte solvents. The positive electrode was composed of carbon coated $LiFePO_4$, additive carbon, and PVDF binder. Both of these coated carbon and carbon additives along with the electrolyte interact with Raman laser and complicate the study of $LiFePO_4$ phase transition.

Table 4.1: List of Raman active vibration modes for components (electrode material and electrolyte) of the working battery.

Material	Vibration Mode	Peak Position, cm_{-1}	Reference
$LiFePO_4$	Asymmetric stretching of PO_4^{3-} (υ3)	1067, 995	[102]
	Symmetric stretching of PO_4^{3-} (υ1)	949, 943	[102]
$FePO_4$	Asymmetric stretching of PO_4^{3-} (υ3)	1126, 1068	[102]
	Symmetric stretching of PO_4^{3-} (υ1)	959	[102]
	Symmetric bending of PO_4^{3-} (υ2)	665	[102]
	Asymmetric stretching of PO_4^{3-} (υ4)	588	[102]
γ-$Li_3Fe_2(PO_4)_3$	PO_4^{3-} deformation	448, 586	[117]
	Internal stretching of PO_4^{3-}	990, 1040, 1119	[117]
α-Fe_2O_3	O-Fe-O bending	395	[117]

Table 4.1—*Continued*

	Fe-O stretching	600	[117]
	Disorder band due to point defects	646	[117]
	Second order disorder band due to point defects	1280	[117]
C	C-C in-plane bond stretching mode E_{2g} of sp^2 bonded graphite (G band)	1585 or 1582	[114, 121]
	Breathing mode of sp^2 sites A_{1g} in hexagonal rings of carbon in graphite planes (D band)	1350	[122]
	Disordered sp^3	1194, 1490, 1620	[115, 121, 123, 124]
EC	Symmetric stretching of C–O	900, 905 (salt solvated)	[125]
	Bending of C=O	720, 730 (salt solvated)	[125]
DMC	Symmetric stretching of C–O	920, 930 (salt solvated)	[125]

Some corrective measures were taken to understand these Raman interactions to get the phase transition signals from the active material $LiFePO_4$. $LiFePO_4$ particles were coated with carbon during the synthesis to enhance the electronic conductivity, but this coated carbon significantly diminishes the Raman vibration signal from the $LiFePO_4$ [117]. The coated carbon has both sp^2 bonded graphitic carbon (G band) whose position is at around 1580 cm^{-1}, and also disordered sp^3 bonded diamond carbon (D band) whose position is at around 1340 cm^{-1}. The position of G band and D band is marked in Fig.

4.3D. This sp^2 bonded graphitized carbon is beneficial because it enhances the electronic conductivity to the $LiFePO_4$ particle, particularly at the surface where electrochemical reaction takes place, but it gives hindrance to the optical penetration of the Raman laser. The Raman laser skin depth δ is expressed as

$$\delta = \frac{c}{\sqrt{2\pi\mu\sigma\omega}} \quad \text{.....4.1}$$

where ω is the optical frequency, μ is the permeability, *c* is the speed of light, and σ is the electrical conductivity of the sample. Once the carbon coating from the $LiFePO_4$ is removed, the conductivity is reduced causing the laser optical skin depth increased to get the enhanced signal from $LiFePO_4$. So, carbon coating from the $LiFePO_4$ particles has to be removed partially from the areas to be studied. This ensured minimal detrimental impact on the phase transformation because most of the areas on the electrode were unaltered to make a successful working battery for the in-situ Raman spectroscopy. Raman laser simply could gasify this coated carbon without altering the $LiFePO_4$ in olivine structure [117]. Before testing the battery the cathode was exposed to 10 mW Raman laser for 5 minutes to gasify the coated carbon to carbon dioxide. But during gasification of coated carbon, the decomposition of $LiFePO_4$ can also happen according to the following reaction.

$$12LiFePO_4 + 3O_2 \rightarrow 4Li_3Fe_2(PO_4)_3 + 2Fe_2O_3$$

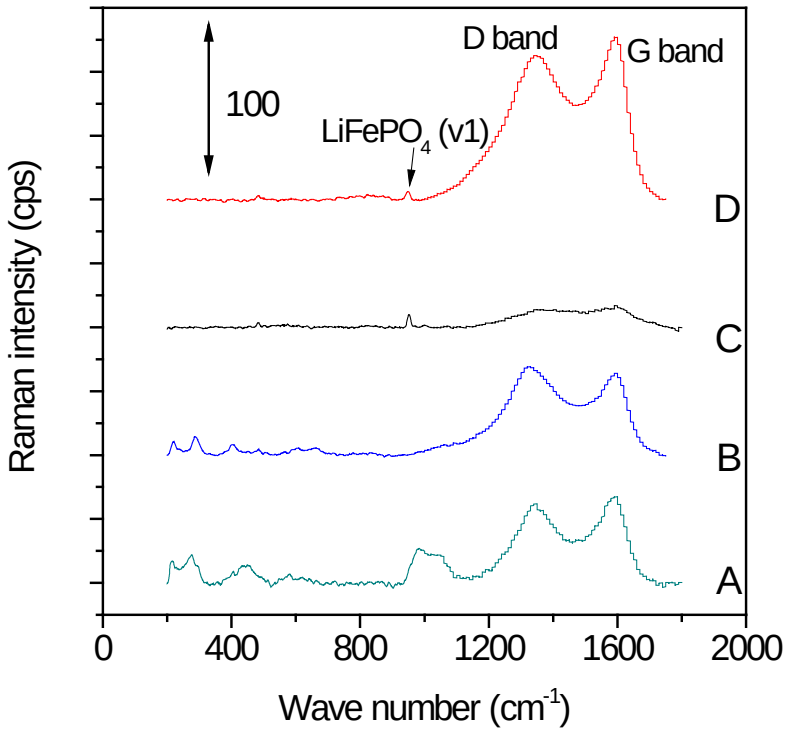

Figure 4.3: Raman spectra from four different areas after carbon gasification treatment. Areas A and B show decomposition of $LiFePO_4$ while areas C and D shows the vibration signal of PO_4^{3-} (υ1) of $LiFePO_4$ material [106].

Special care has been taken to minimize or totally avoid $LiFePO_4$ decomposition by the Raman laser. Fig. 4.3 [106] shows Raman spectra of four different areas (150 µm × 150 µm) after the gasification of coated carbon on $LiFePO_4$ particles. Areas C and D in Fig. 4.3 show the presence of vibration mode (υ1) of $LiFePO_4$ while areas A and B do not show the Raman signal from $LiFePO_4$, but rather some other vibration signals which come from the decomposition product of γ-$Li_3Fe_2(PO_4)_3$ at 488, 990 and 1040 cm^{-1} [117] and from the decomposition product of Fe_2O_3 at 217, 277, 395, and 600-650 cm^{-1} [117]. So, the C or D area was considered for in-situ study area as they give the $LiFePO_4$ signature signal and did not show any decomposition of $LiFePO_4$.

4.4 In-situ Raman experiment: Data Recording and Analysis

In Table 4.1, it has been already shown that there are several Raman active vibration modes for both $LiFePO_4$ and $FePO_4$. Among them, Raman bands of $LiFePO_4$ (υ1) at around 950 cm^{-1} and of $FePO_4$ (υ1) at around 960 cm^{-1} were targeted for study using in-situ Raman spectroscopy as these signals are more intense than others. After making the battery and before the in-situ study, the areas C and D (Fig. 4.3) were mapped for the intensity of the $LiFePO_4$ signal (950 cm^{-1}) to find the suitable spot for further in-situ investigation. Such a mapping (80 µm× 80 µm) for signal at 950 cm^{-1} is shown in Fig. 4.4 [106]. The spots with intense $LiFePO_4$ signal (950 cm^{-1}) were considered for further in-situ study.

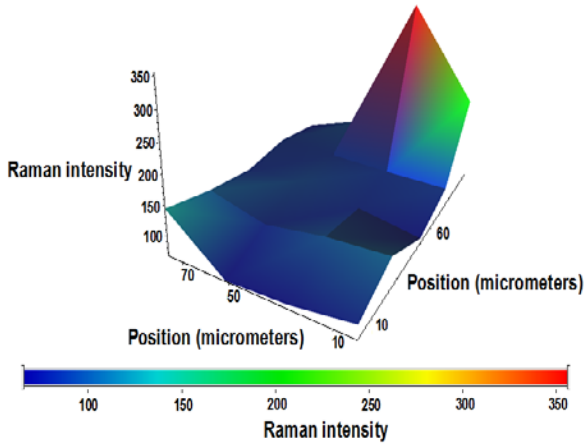

Figure 4.4: Raman mapping of a area after carbon gasification process of the electrode. The points with intense signal from the vibrational signal of PO_4^{3-} (υ1) of $LiFePO_4$ material can easily be found from this map which can be used for subsequent in-situ study [106].

In-situ Raman studies were conducted using a Thermo Scientific DXR with a 780 nm laser. The laser spot size was 2 µm with a laser power of 2 mW using 10X magnification objective lens. The exposure time was 16 s with a photo-bleach time of 30 s. The schematic in Fig. 4.5 shows the microscopic description of the electrode under the

in-situ Raman laser. The average particle size used in this experiment was around 200 nm as is shown in Chapter 3; the laser spot size was 2 μm and the Raman laser focused area contained only a few active material particles. Thus the in-situ Raman study would be able probe the particle-level phase transition phenomena.

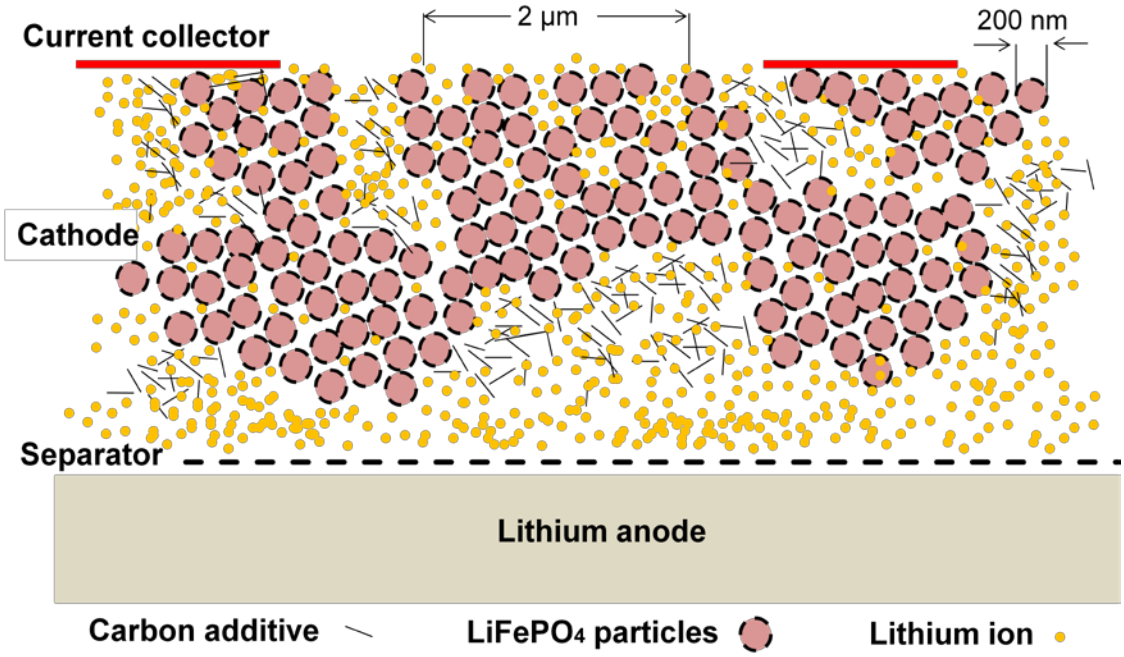

Figure 4.5: Schematic showing electrode configuration for in-situ study. The small laser spot only focuses on few active material particles.

4.4.1 First Cycle: Slow discharge

During the in-situ Raman study, the Li ion cell was electrochemically charged and discharged using a multi-channel battery tester. The cell was charged and discharged for three cycles; each cycle was at different rates. The first cycle started with a constant-current charge at 0.3C until the cell voltage reached 4.0 V, then followed by a constant-voltage charge at 4.0 V for 20 minutes. After that rest period of 45 minutes was introduced and the cell was then discharged at 0.3C rate until the voltage reached 2.5 V,

then followed by a 1 hour rest period. The first-cycle electrochemical test result is presented in Fig. 4.6 where the black vertical lines on the potential profile curve indicate the points where the Raman spectra were collected.

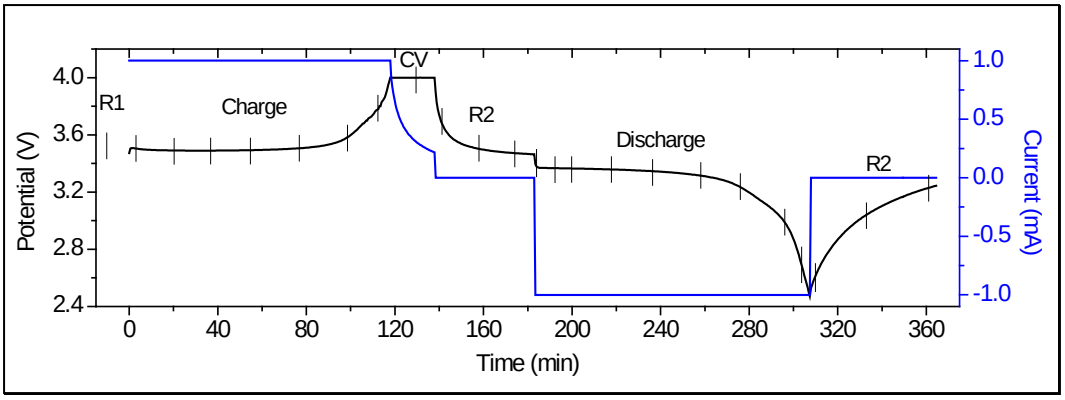

Figure 4.6: Charge discharge cycle at 0.3C rate during slow rate in-situ Raman spectroscopy. Blue line indicates the current profile and the black line indicate the potential profile and vertical lines on them indicates the point when the Raman spectra were recorded.

The associated Raman spectra that were collected during the 1st cycle of the electrochemical test are presented in Fig. 4.7. From the spectra (Fig. 4.7) it is clearly observed that during charge the $LiFePO_4$ particles transformed suddenly to $FePO_4$ between scan C5 and C6 (Figure 4.7). The same feature was observed during the discharge process where at the very beginning the signature $LiFePO_4$ phase peak showed up from scan D2, indicating that all the particles under the laser spot got transformed completely. To understand it better, quantitative analysis was performed on each spectrum by doing the Gaussian fit analysis. The Gaussian fit analysis of a representative spectrum (scan D1, 1st cycle) that contains both distinctive signature peaks of $LiFePO_4$ and $FePO_4$ is shown in Fig. 4.8.

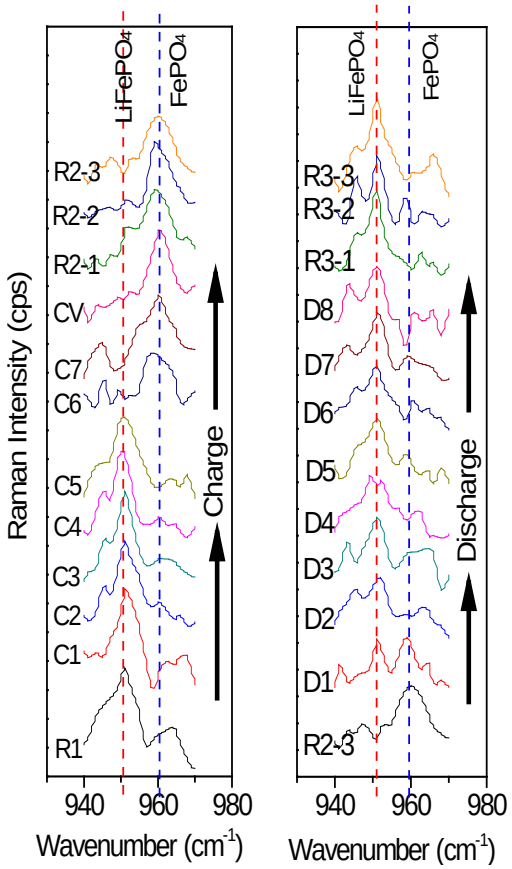

Figure 4.7: Raman spectra collected during electrochemical charge discharge at 0.3C. R1, R2, and R3 indicates the Raman spectra collected during rest period and C1, C2, etc indicates the Raman spectra taken during charge and D1, D2, etc are Raman spectra taken during discharge as indicated in Fig. 4.6.

During the Gaussian fit analysis of any spectrum, constant baseline correction was applied and the same level of correction was applied to all of the spectra to keep the quantitative analysis unbiased. From the Gaussian fit analysis of each spectrum, the peak intensity information of each peak ($LiFePO_4$ peak and $FePO_4$ peak) was taken to calculate the relative amount of phases present at any point of charge or discharge. For example, as shown in Fig. 4.8, the intensities of $LiFePO_4$ and $FePO_4$ peaks are 1.53 and

1.66, respectively, corresponding to the relative amounts of 48.03% and 51.97% for the $LiFePO_4$ and $FePO_4$, respectively, at that point.

The relative amount of phases during the charge and discharge process obtained from the Gaussian fit analyses are plotted and shown in Fig. 4.9. It is observed that during the charge process the particles in the probed area under the Raman laser transformed abruptly between scan C5 and C6; and during the discharge process, the study area of the electrode finished phase transition within the first two scans. This indicates that once phase transition starts within that small area of the electrode, it finishes very quickly.

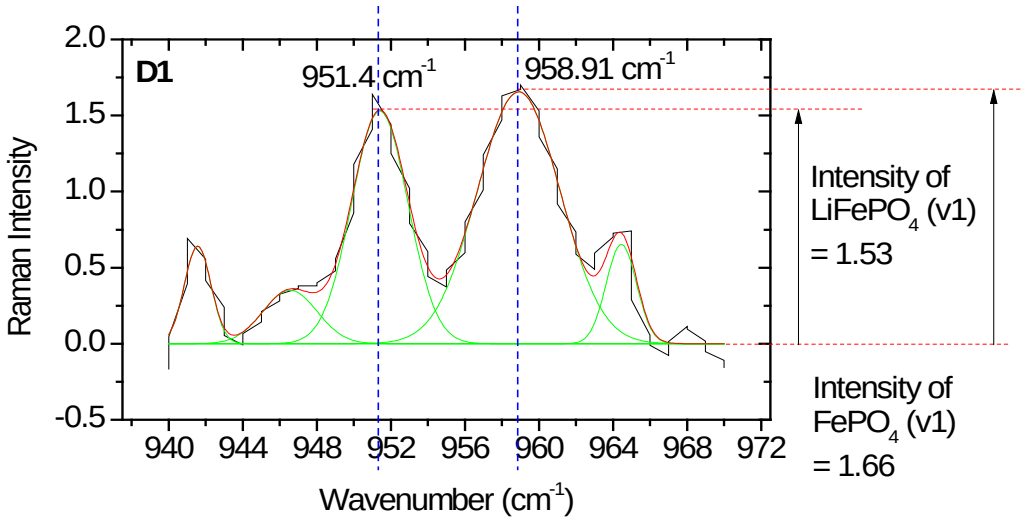

Figure 4.8: Peak de-convolution and Gaussian fit analysis of one representative Raman spectra D1 collected during electrochemical discharge at 0.3C. The time when D1 is indicated by the 1st vertical line on the potential profile of discharge curve in Fig. 4.6.

It is already explained that the in-situ Raman study only investigated a few particles under the laser focus. Though the electrode microstructure is very much heterogeneous considering a large area of electrode, the small local area (Raman laser

spot size of 2 μm) is quite homogeneous in terms of the local electronic conductivity and the availability of Li ion through the porous network of electrode. So, the particles in a small local area complete phase transition almost together and hence once phase transition starts it gets completed very quickly. Scan D1 shows that half of the particles got transformed within the probed area, but the very next scan indicates the completion of phase transition for all the probed particles. This clearly shows that in any individual particle once the phase transition starts, it completes very quickly. This particle-level phenomenon is in good agreement with the phase transition mechanism as explained by the domino cascade model [73].

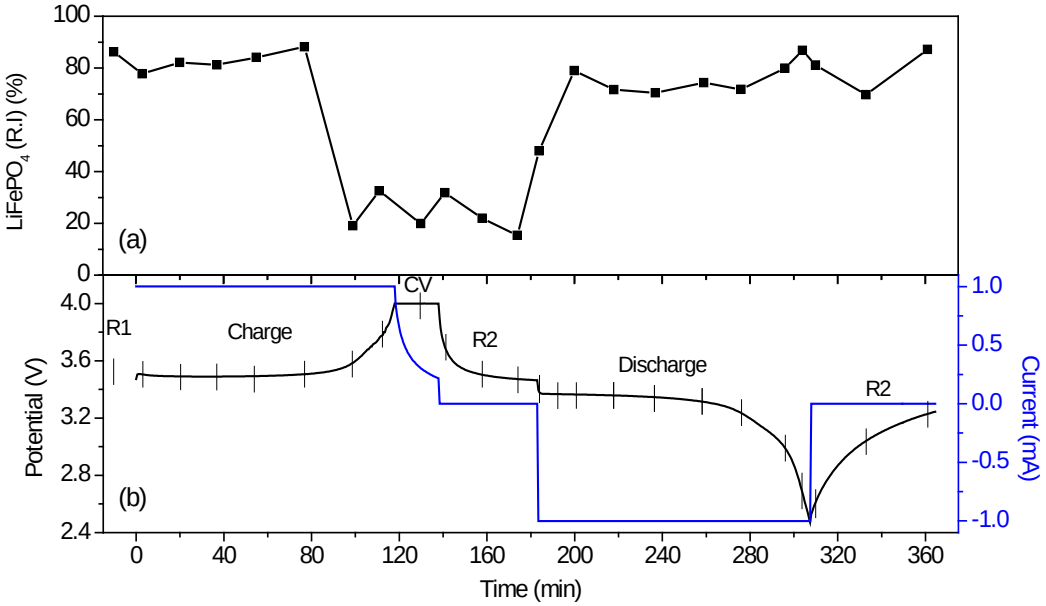

Figure 4.9: (a) Progress of phase transition during charge and discharge at 0.3C. (b) Current and Potential profile during charge and discharge is shown along with the points when Raman spectra were recorded.

4.4.2 Effect of Discharge rate: Second and Third cycle

The in-situ Raman study was also performed for two more cycles. In the second cycle, the cell was electrochemically charged at 1C rate until the cell voltage reached 4.0 V, then followed by a constant-voltage charge for 50 minutes at 4.0 V. After that a rest period of 35 minutes was introduced. The cell was then discharged at a constant rate of 1C until the voltage reached 2.0 V, subsequently followed by a rest period of 30 minutes. The electrochemical charge-discharge test results are presented in Fig. 4.10(a) and the associated Raman spectra are presented in Fig. 4.10(b).

At a higher rate charge such as 1C, it is clearly observed from Fig. 4.10(b) that the phase transition was delayed and in some particles the phase transition did not take place at all. The last scan of Raman spectrum (C5) during the constant-current charging shows a small shoulder of the $FePO_4$ phase, and during the constant-voltage charging almost half of the particles in probed area got transformed even though the charging current was reduced as seen from Fig. 4.10(b). Finally at the end of the charging process, approximately half of the particles got transformed.

During the discharge at 1C rate, the first scan D1 shows almost no transformation from the rest cycle 'R2'. But the second scan D2 shows that most of the particles (not all) that transformed during the charging process transformed back to $LiFePO_4$. Only a weak $FePO_4$ peak remained and that weak $FePO_4$ peak is present in all the scans after D2. So this high-rate charge and discharge show that even the Raman laser spot was very small (2 µm) and it contains only a few particles, heterogeneity arises at high rate at the very local area. Some particles within the perimeter of a few µm do not transform simultaneously, leading to an obvious delay in phase transition at a higher rate.

The third cycle of the electrochemical test was performed at a even higher rate of 2C. The cycle started with a constant-current charge at 2C rate until the potential reached

4.0 V, which was then followed by a constant-voltage charge at 4.0 V for 15 minutes and then by a rest period of 15 minutes. The cell was then discharged at 2C rate until the voltage reached 2.0 V; after that the cell was rested for 15 minutes. The electrochemical result for this cycle is presented in Fig. 4.11(a) and the associated Raman spectra are presented in Fig. 4.11(b). From the spectra, it is observed that almost no phase transition took place for the $LiFePO_4$ particles under the Raman laser as a similar weak $FePO_4$ peak was observed throughout the cycle. At this high charge/discharge rate, the phase transformation did not take place in any of the particles that were present in the probed area even though phase transformation was observed at a lower rate (0.3V).

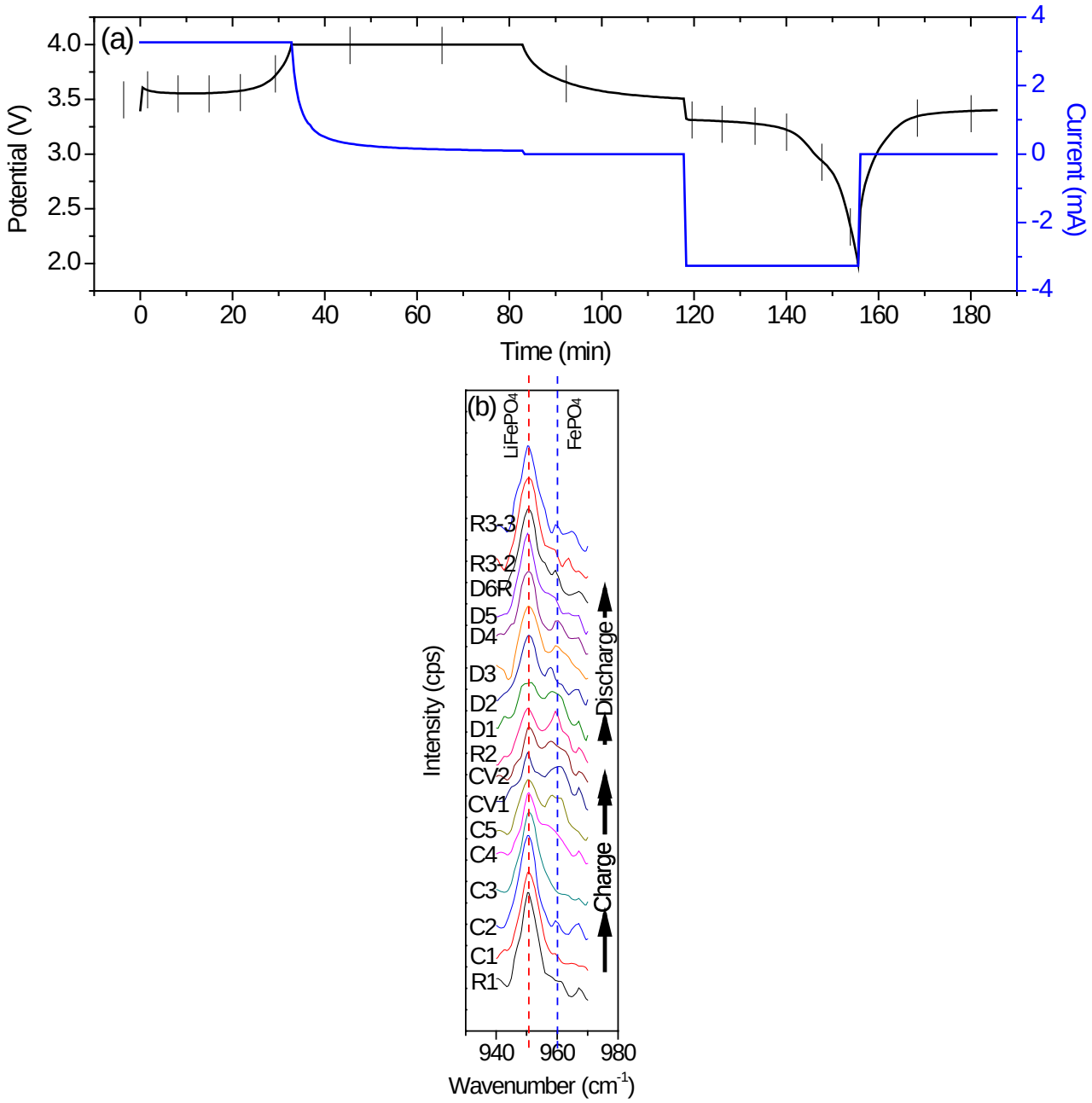

Figure 4.10: (a) Progress of phase transition during charge and discharge at 1C. (b) Current and Potential profile during charge and discharge is shown along with the points when Raman spectra were recorded.

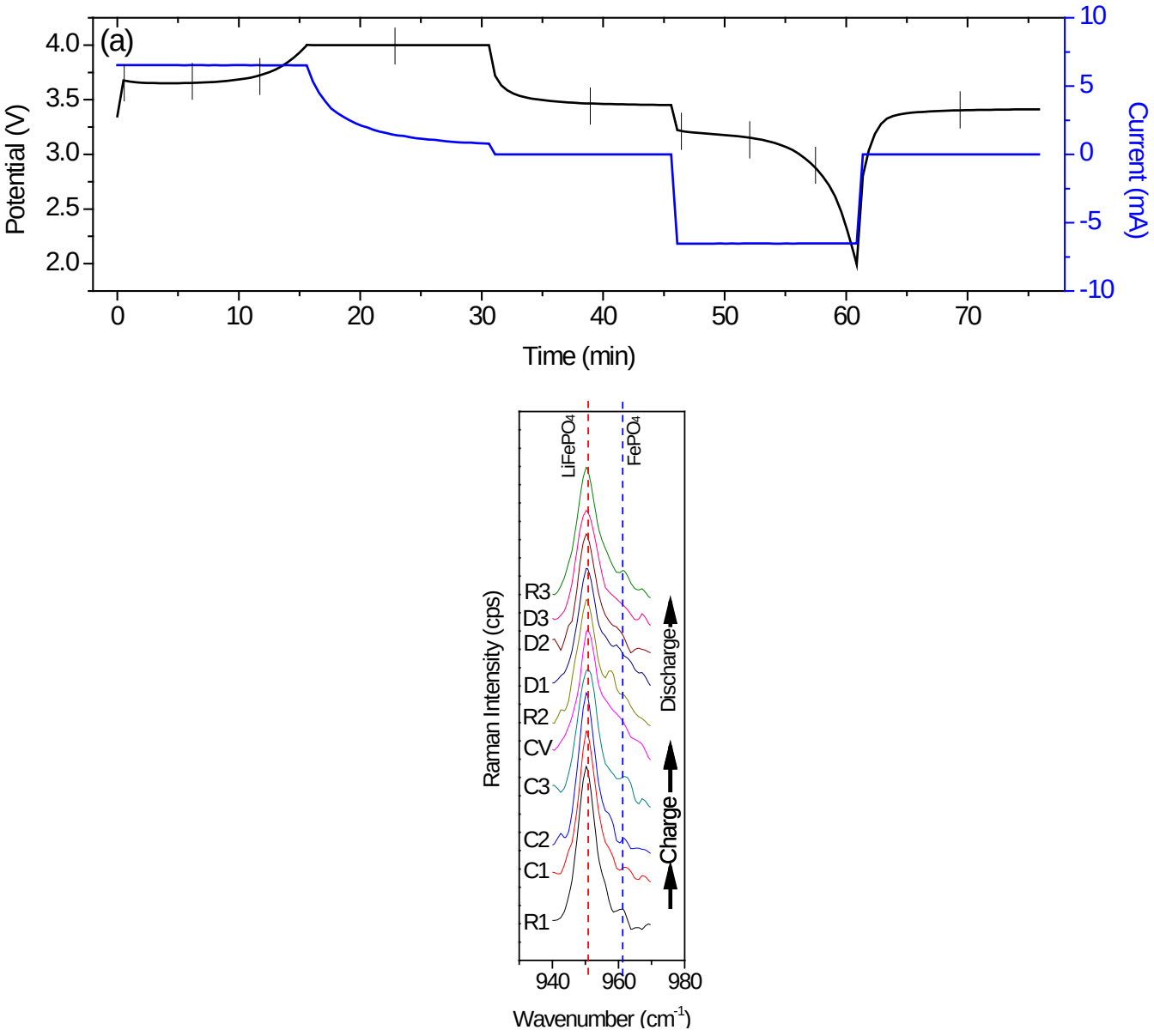

Figure 4.11: (a) Progress of phase transition during charge and discharge at 2C. (b) Current and Potential profile during charge and discharge is shown along with the points when Raman spectra were recorded.

4.5 Conclusion

This chapter discusses the detailed experimentation technique and results for the in-situ Raman study. The Li ion cell was charged and discharged at three different rates including 0.3C, 1C and 2C. The Raman laser spot size was 2 μm and the average particle size of $LiFePO_4$ was about 200 nm, indicating the probed electrode area contained only a few active material particles. During the slow discharge, it was observed that during charge and discharge once the phase transition started it finished very quickly. This finding is in good agreement with the domino-cascade model. During the fast discharge or charge at 1C, though the similar trend of quick phase transition upon being initiated still holds, a general phase transition delay was observed. At the end of charge or discharge process, not all the particles completely transformed. Further increasing the charge and discharge rate causes a very unfavorable situation where almost no phase transition was detected by the in-situ Raman spectroscopy.

Chapter 5

In-situ X-ray Diffraction (XRD) Study

5.1 Introduction

Among all the spectroscopic techniques available, X-ray diffraction is very suitable to study the phase transition of $LiFePO_4$. However, there is a limitation of using the traditional diffractometer that uses powder or polycrystalline samples: the X-ray irradiated area is quite big and it gives the average results of transformed/untransformed phases. This restricts the opportunity to study the related process at the particle level. In the previous chapter, in-situ Raman spectroscopy has been successfully applied to get the particle-level phase transition information.

In this chapter, the use of an in-situ XRD spectroscopic techniques will be discussed which is targeted to understand the phase transition phenomena of $LiFePO_4$ material. The chapter will cover details of the in-situ XRD experiment including the design of the battery housing containing X-ray transparent window, electrode preparation that enables investigation of the active material in the reflection mode of X-ray diffraction, electrochemical test protocols, and finally results of the phase transition study.

5.2 Making battery housing for in-situ XRD study

Making a battery seems very easy as it consists of very simple components like electrodes, separator and electrolyte. But Li-ion batteries use non-aqueous electrolyte and the atmospheric moisture when absorbed can degrade the electrolyte thus causing performance/capacity loss. Besides, for our experimental Li-ion batteries fresh lithium metal ribbons were used as the anode which even cannot tolerate trace amount of oxygen and moisture. All these conditions require a sealed housing which will hold the

battery components such as electrodes, separator, and non-aqueous liquid electrolyte. In case of studying the battery with the in-situ XRD the housing has another set of extra requirements which include the compatibility that it needs to fit into the sample holder of the XRD machine, and incorporation of an X-ray transparent window which will allow the X-ray to interact with the electrode materials and the diffracted beams to be recorded. To meet all these requirements, a specially designed battery housing was fabricated in the lab. The schematic design and the working case are shown in Fig. 5.1. Inside the housing near the cap two electrical connectors were placed to conduct current produced from the battery to an external battery tester.

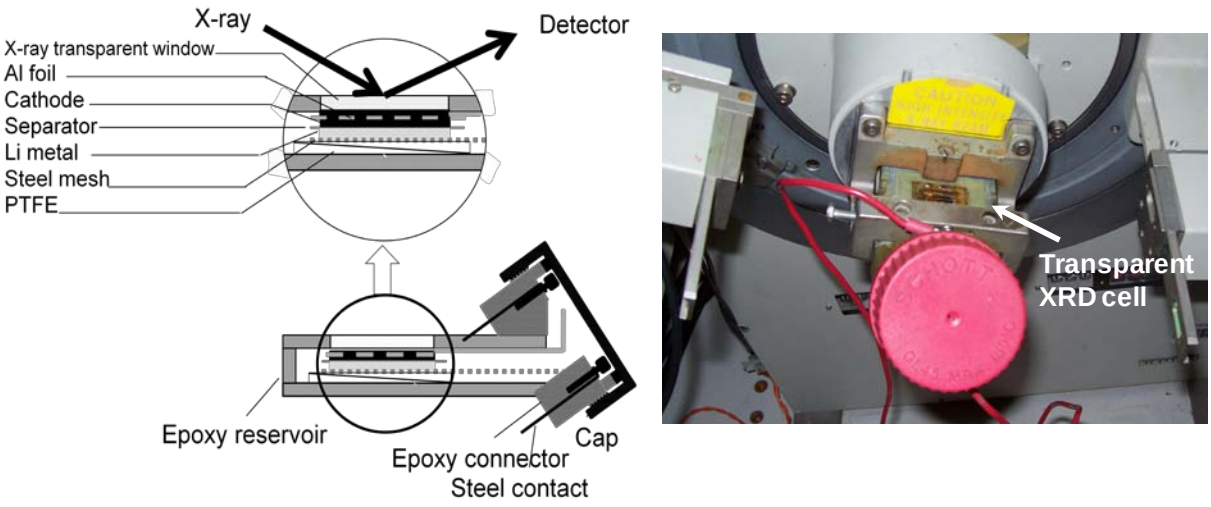

Figure 5.1: Schematic of the cell design for in-situ XRD study is shown on the left side and the real working cell operating in the X-ray diffractometer sample holder is shown on the right side.

As shown in Fig. 5.1, the battery housing is made of epoxy and the X-ray transparent window is made of a Kapton film. The Kapton film has been tested for X-ray

transparency and the XRD pattern of the $LiFePO_4$ powders under the Kapton film is shown in Fig. 5.2.

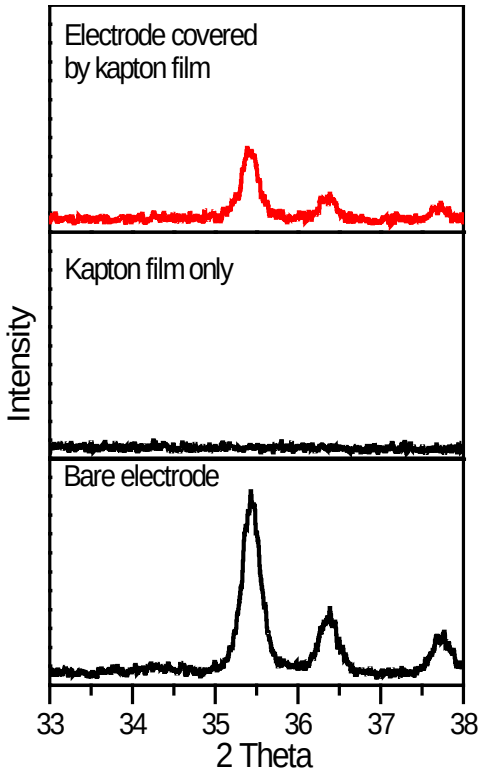

Figure 5.2: XRD spectra shown under the Kapton film indicates the suitability of using as a X-ray transparent window material in the electrochemical cell to be used in in-situ XRD study.

5.3 Electrode preparation and battery assembly for in-situ XRD study

Electrodes for the in-situ study are different in design comparing to the electrodes that were used in the normal Li-ion batteries. The positive electrode in normal batteries has active material ($LiFePO_4$) coated on one side of the current collector (Al foil), which is then facing towards the negative electrode (anode). But with this configuration it is impossible to study the active materials using the traditional X-ray diffractometer.

Traditionally the reflection mode of diffraction is used in XRD studies and the aluminum foil as the current collector blocks the active materials from the direct access of X-ray. So, the electrodes that will be used for the in-situ XRD study have active materials coated on both sides of a homemade aluminum mesh. As the current collector is a mesh instead of a solid film, electrolyte can always percolate to the other side through porous network of active materials and eventually electrochemical reactions can take place throughout the active materials of both sides. One side of the electrode faced toward the anode and the other side was studied using reflection-mode XRD.

The meshed aluminum foil was coated with active material mixture (65% active material, 20% C, 15% PVDF) on both sides using a doctor blade and then dried in a vacuum oven at 120 ^{o}C for 5 hours. Subsequently the active material and current collector sandwich was pressed with a 2 ton/cm^2 pressure. Finally, the electrode was cut to appropriate size (1.5 cm × 1.5 cm) to be used in the battery.

For the anode, an appropriate size (1.5 cm × 1.5 cm) of lithium ribbon was cut and the oxide layer was scratched off to expose the fresh lithium surface in an argon filled glove-box. This lithium ribbon was then pressed against a steel mesh and this steel mesh acted as an electrical connector with anodic lithium.

Before making a battery, the previously prepared cathode was dried for at least 6 hours and other components such as battery housing, the anode, screws, separator and accessories to make the battery were cleaned and dried for 30 minutes to ensure that they were free from moisture. To assemble the battery the Celgard® 2500 separator was placed between the two electrodes to form a sandwich which was then placed inside the specially designed battery housing (Fig. 5.1). Two PTFE wedges were pushed beneath the electrode sandwich upwards so that the cathode surface reached close to the X-ray transparent window. The next step is to add a freshly prepared electrolyte which was a

1M $LiPF_6$ solution with a mixed solvent system of 1:1 (volume ratio) of DMC:EC. The final step was to cap the battery housing to ensure proper sealing. The battery was kept inside the glove-box for a few hours so that separator and electrodes were soaked properly and the total system stabilized. After that, the extra electrolyte was drained to avoid the X-ray scattering during in-situ XRD experiment.

5.4 In-situ XRD experimentation

Before placing the battery inside the sample holder of the X-ray diffractometer the battery was tested with a few cycles of charging and discharging. During the in-situ XRD experiment, the electrochemical charging and discharging were conducted using a MTI multi-channel battery tester and the X-ray diffraction test was conducted using Siemens D500 X-ray diffractometer.

5.4.1 Test Protocol and Recording the real-time phase transformation

For the in-situ XRD experiment, the battery was tested at four different rates. Each cycle of electrochemical charging and discharging consisted of five consecutive steps. The first step was to charge the battery with a constant current at 0.1C rate followed by the next step of constant-voltage charge for 15 minutes. The battery was then kept at rest (third step) for 15 minutes. The battery was subsequently discharged at a constant rate (fourth step) followed by another rest period (fifth step) of 15 minutes. During the constant-current charging step, the cell voltage was set to a window between 2.5 V and 4.1 V and the constant voltage charging is maintained at 4.1 V. The battery was discharged at four different discharge rates of 0.1C, 0.3C, 0.5C and 1C. The test protocol of this in-situ XRD study is summarized in Table. 5.1.

The XRD pattern of the synthesized material is already presented in Fig. 3.2. Among all the peaks, $LiFePO_4$ (311) is targeted for study as intensity of this peak is the

highest and noises from the battery components such as electrolyte block some of the peaks. The position of the $LiFePO_4$ (311) peak is at ~35.66^o (2θ), and the position of the $FePO_4$ (311) is calculated as 36.703^o considering the lattice parameters of a, b, c as 9.81 A^o, 5.79 A^o and 4.78 A^o [126, 127]. There is one more peak corresponding to $LiFePO_4$ (121) at 36.6^o between $LiFePO_4$ (311) and $FePO_4$ (311). Therefore, the X-ray scan range was from 35.1^o to 37.1^o (2θ) with 0.01^o step size. The X-ray collection time for each step was 1 s and hence the total scan time over the targeted angle range is approximately 200 s. The electrochemical charge-discharge cycle is shown in Fig. 5.3 and corresponding in-situ XRD patterns are presented in Fig. 5.4. Black lines in Fig. 5.3 indicate potential profile and the blue lines indicate the current profile. The vertical black lines on the potential profile indicate the points while the in-situ XRD pattern was recorded.

Table 5.1: Protocol of the electrochemical charge-discharge for the in-situ XRD study.

Cycle Number	Discharge Rate	Charge Discharge Potential	Constant Current Charge	Constant Voltage Charge	Rest Period (min)	Constant Current Discharge	Rest Period (min)
1	0.1C	2.5 to 4.1 V	0.3602 mA	4.1 V	15	0.3602 mA	15
2	0.3C	2.5 to 4.1 V	0.3602 mA	4.1 V	15	1.081 mA	15
3	0.5C	2.5 to 4.1 V	0.3602 mA	4.1 V	15	1.801 mA	15
4	1C	2.5 to 4.1 V	0.3602 mA	4.1 V	15	3.602 mA	15

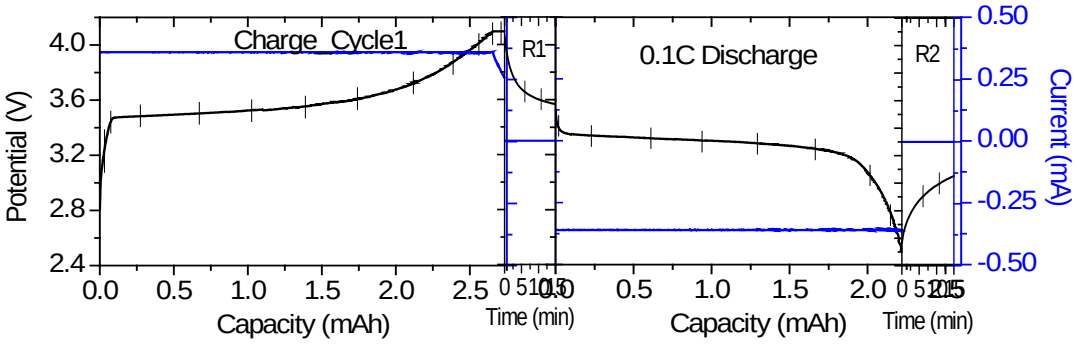

Figure 5.3: Charge discharge cycle at 0.1C rate (1st cycle) during slow rate in-situ Raman spectroscopy. Blue line indicates the current profile and the black line indicate the potential profile and vertical lines on them indicates the point when the Raman spectra were recorded.

Qualitatively, from Fig. 5.4 it is observed that at the beginning of the charging, the peaks of $LiFePO_4$ were observable on the XRD patterns, while at the end of charging the $LiFePO_4$ (311) became very weak. At the same time the $FePO_4$ (311) became dominant indicating the completion of the phase transition of most of the active material particles. It is also found that at the end of the discharge process, $LiFePO_4$ (311) peak again became strong and $FePO_4$ (311) weakened.

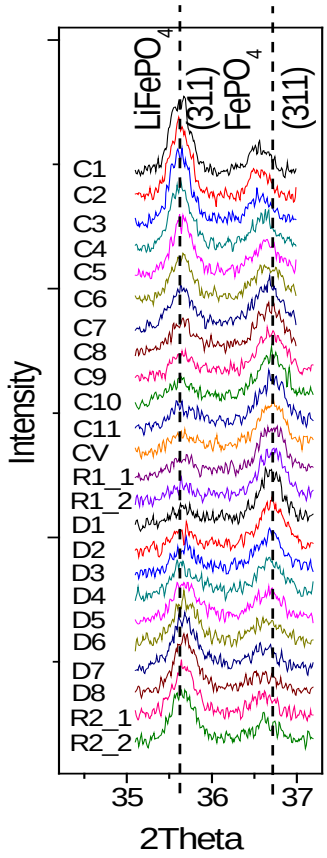

Figure 5.4: XRD patterns collected during electrochemical charge discharge at 0.1C (1st cycle). R1, and R2 indicates the XRD patterns collected during rest period and C1, C2, etc indicates the XRD patterns taken during charge and D1, D2, etc are XRD patterns taken during discharge as indicated in Fig. 5.4.

To quantify the phase transition process, the peaks in the XRD patterns were de-convoluted using Gaussian fit and the peak intensities were obtained and used to quantify the relative amount of the present phases. The de-convolution of one representative scan of D6 using Gaussian fit peak is shown in Fig. 5.5. Before the de-convolution, the XRD pattern was corrected using a constant baseline. From the de-

convoluted peaks, the peak positions, and heights were obtained. Peak positions are almost the same during the course of charging and discharging process. From the resolution of the obtained XRD patterns, it is difficult to draw any conclusion about the lattice strain during Li ion de/intercalation process. As the peak positions were almost identical, it is concluded that during electrochemical charge discharge, only two end members ($LiFePO_4$ and $FePO_4$) were present and no compound with intermediate composition (Li_xFePO_4) was observed in the cycles. However, the peak height was used to obtain the relative amount of phases at any stage of electrochemical charge or discharge, which gives the progress of the phase transition.

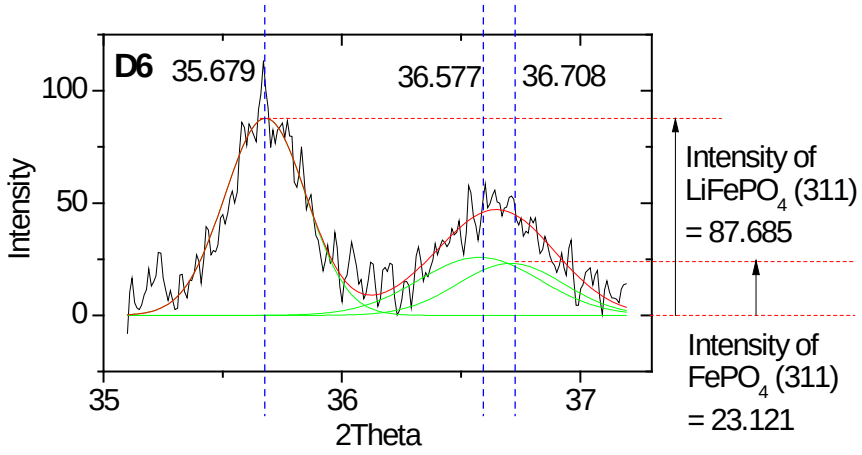

Figure 5.5: Peak de-convolution and Gaussian fit analysis of one representative XRD pattern D6 collected during electrochemical discharge at 0.1C. The time when D6 is indicated by the 6th vertical line on the potential profile of discharge curve in Fig. 5.3.

Fig. 5.6 a) shows the profile of relative amount of two phases during charge and discharge (Fig. 5.6 b)) of the first cycle. The solid lines with the square symbols (Fig. 5.6 a)) indicate the relative amount of two phases; black lines are for $LiFePO_4$ and blue lines are for $FePO_4$. It is observed that at the end of charging, the $LiFePO_4$ phase was not

completely transformed. In fact, if a longer constant-voltage charging step was used, the phase transition would progress even more toward the complete transformation. But a shorter constant voltage charge period (15 minutes) was actually used. From the Gaussian fit analyses, it was found that at the end of charging during the first cycle, the completed phase transition was approximately 80%. So to get the relative amount of phase transition during discharging, this remaining 20% untransformed materials is deducted from the amount of the second phase (during discharge, the second phase is $LiFePO_4$). Eventually, the progress profile of the phase transition during 0.1C rate discharge obtained is presented in Fig. 5.7. The dotted line in Fig. 5.7 represents the theoretical path of phase transition progress and it is found that the slow discharge at 0.1C almost follow the equilibrium path. This indicates that during a slow discharge, Li ions get enough time to maintain the equilibrium phase transition while in case of fast discharge the phase transition progress is expected to deviate from the theoretical path.

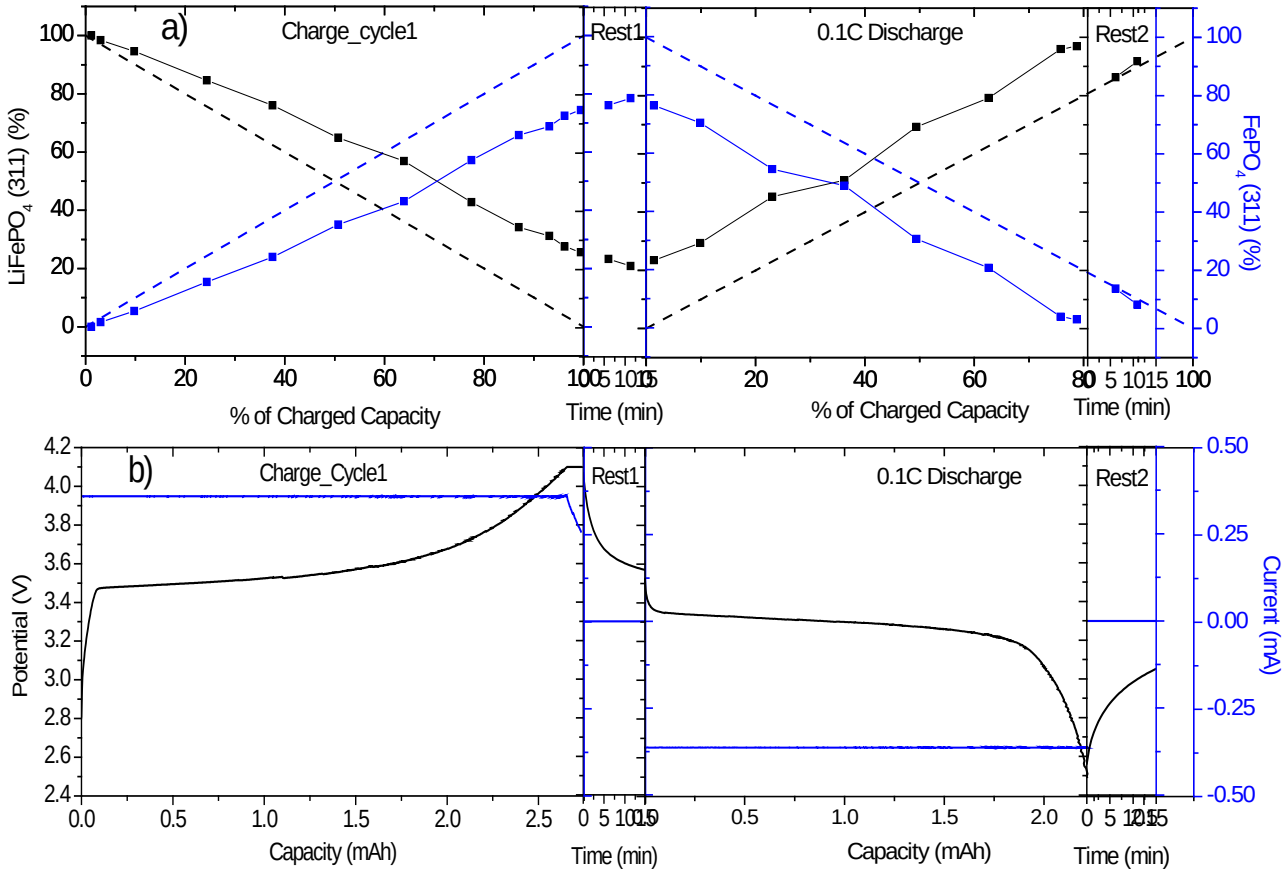

Figure 5.6: (a) Phase transition progress during electrochemical charge discharge at 0.1C (1st cycle). The dotted lines indicate the equilibrium progress paths. (b) Electrochemical charge discharge profiles of the 1st cycle, where blue lines indicate current profile and black lines indicate potential profile.

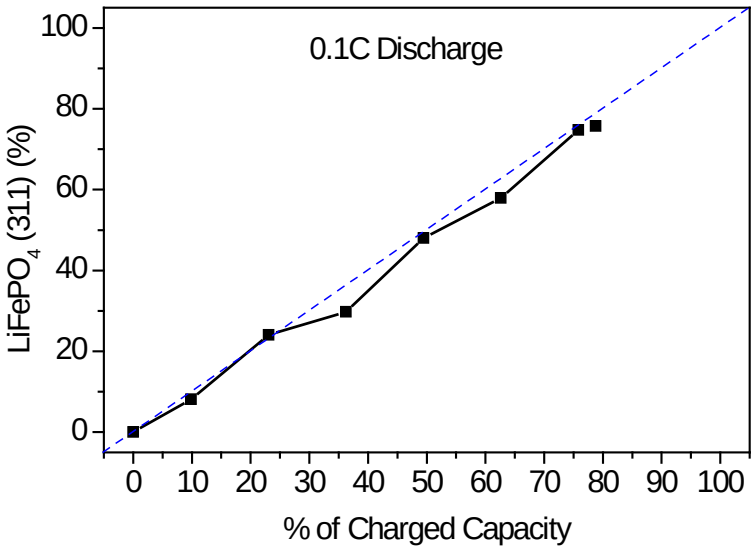

Figure 5.7: Phase transition progress line during electrochemical discharge at 0.1C (1st cycle) after the correction of history from the charge process. The dotted line indicates the equilibrium progress path.

5.4.2 Effect of Discharge rate

The in-situ XRD patterns obtained during other cycles are presented in Fig. 5.8. From Fig. 5.8 (a) it is found that from scan C4 to R3_2 (the rest period after charge during the 2nd cycle), the noise is significant and the diffraction patterns cannot be quantitatively analyzed. The reason for the noise in those XRD patterns is possible scattering from the electrolyte. During the battery assembly, extra electrolyte of not drained from the cell would scatter the X-ray and cause extra noise. During the 2nd cycle of charging, some of the electrolyte appeared on the top surface which caused scattering of X-ray. This electrolyte scattering problem could not be identified until the rest period after the charge cycle. As soon as the problem was identified, the thin layer of extra

electrolyte was removed from the top surface of the electrode and electrolyte scattering disappeared.

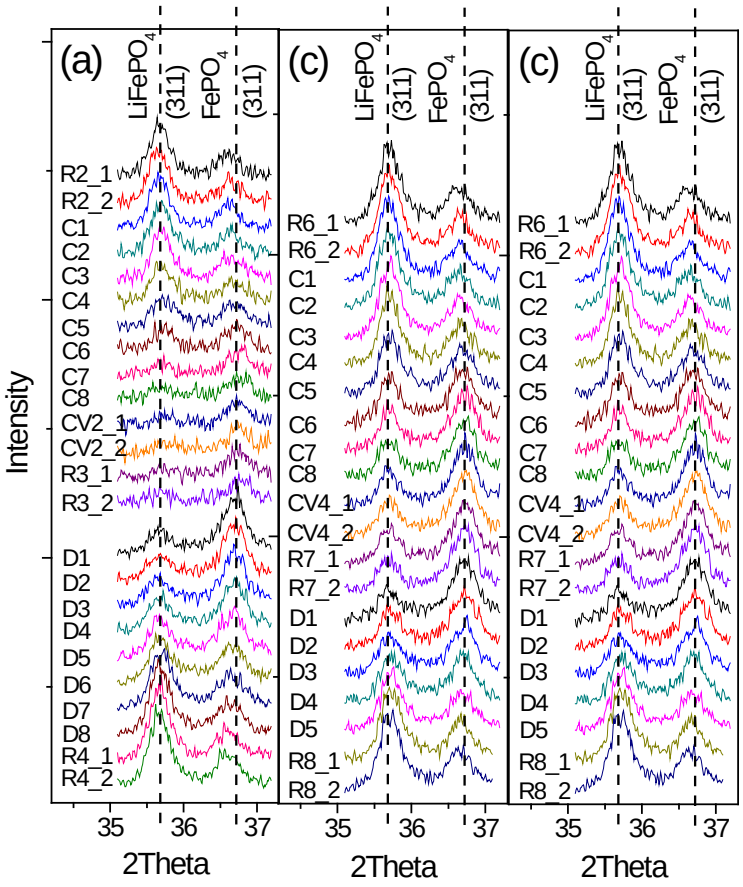

Figure 5.8: (a) XRD patterns collected during electrochemical charge discharge at 2nd cycle. (b) at 3rd cycle (c) at 4th cycle. R1, and R2 indicates the XRD patterns collected during rest period and C1, C2, etc indicates the XRD patterns taken during charge and D1, D2, etc are XRD patterns taken during discharge.

XRD patterns during the 2nd, 3rd and 4th cycles of the charging and discharging were analyzed using Gaussian fit analysis and presented in Fig. 5.9, Fig. 5.10 and Fig.

5.11. In Fig. 5.9, during the charging process, some of the data points are missing due to electrolyte scattering as explained before. In fact analyzing charging behavior was never a target of this whole experiment and that is the reason why all the cycles were done at the same charging rate of 0.1C. Even though charging of the battery was conducted at 0.1C rate for all the four cycles, the progress of the phase transition during the charging process looks different as shown in Fig. 5.9, Fig. 5.10 and Fig. 5.11. The reason of this difference can be easily understood if the amount of both phases is considered at the end of each discharge process. For example, at the end of 1^{st} cycle the relative amount of FePO4 is 8.191% indicating that 8.191% of active material was not transformed. Similarly, at the end of 2^{nd}, 3^{rd} and 4^{th} cycle, the untransformed material was 4.41%, 10.79% and 15.78%, respectively. Because these cycles have different pre-history from the previous discharging step, the progress of phase transition during the subsequent charge process looks different in all cycles.

If the battery usage is considered, the battery discharge process is the most important factor as the discharge of the stored energy is what goes to the device. And also although fast charging of the battery is desired, slow charging of the battery still can be tolerated. But considering various applications of the battery systems, some applications require the battery to discharge quickly to the devices and some applications can accept slow discharge of the battery. Fast discharge may lead to the kinetics-induced non-equilibrium phase transition of $LiFePO_4$. To study this non-equilibrium phase transition, the battery was tested at four different discharge rates such as 0.1C, 0.3C, 0.5C and 1C. However, because of the phase transition history of the previous cycle, it is hard to conceive the real phase transition progress during each discharge (at different discharge rates) from Fig. 5.9, Fig. 5.10 and Fig. 5.11. To get the real quantitative phase transition progress during all the discharge cycles, the amount of untransformed $LiFePO_4$

from the charge of the same cycle (taken from the last XRD scan during the rest period after charge) was deducted from the amount of $LiFePO_4$ during discharge.

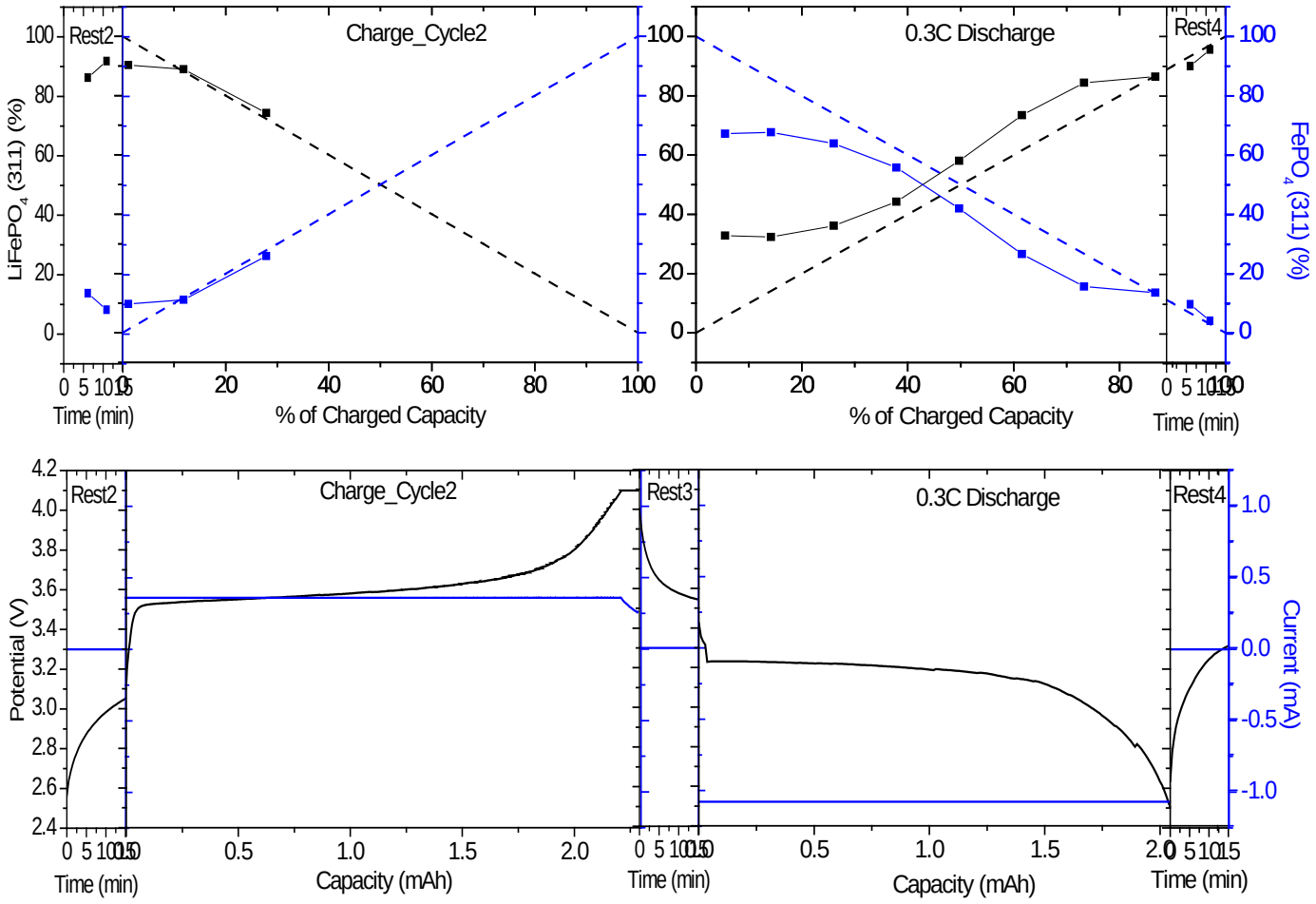

Figure 5.9: (a) Phase transition progress line during electrochemical charge discharge during 2nd cycle (0.3C discharge). The dotted lines indicate the equilibrium progress paths. (b) Electrochemical charge discharge profiles of the 2nd cycle, where blue lines indicate current profile and black lines indicate potential profile.

For 1st, 3rd and 4th cycle, the amount of untransformed $LiFePO_4$ at the end of the rest period after the charge of the respective cycle is 21.19%, 34.85%, and 37.23% respectively. For the 2nd cycle, due to scattering of X-ray by the extra electrolyte, quantitative analysis could not be performed during most of the charge cycle and the rest period after the charge. So, for the 2nd cycle the amount of untransformed $LiFePO_4$ at the end of the charge and rest period is assumed to be 25%. After correcting the progress of the phase transition curve for all cycles, the progress of phase transition during discharge at different rates are shown in Fig. 5.12.

The dotted diagonal in Fig. 5.12 line indicates the equilibrium phase transition progress during the discharge process. As is already discussed, during slow discharge the phase transition progress is close to the equilibrium path (Fig. 5.7). But the progress of phase transition at higher discharge rates was delayed as the progress line deviated from the equilibrium path. Similar kind of phase transition delays were also predicted by the study in reference [95].

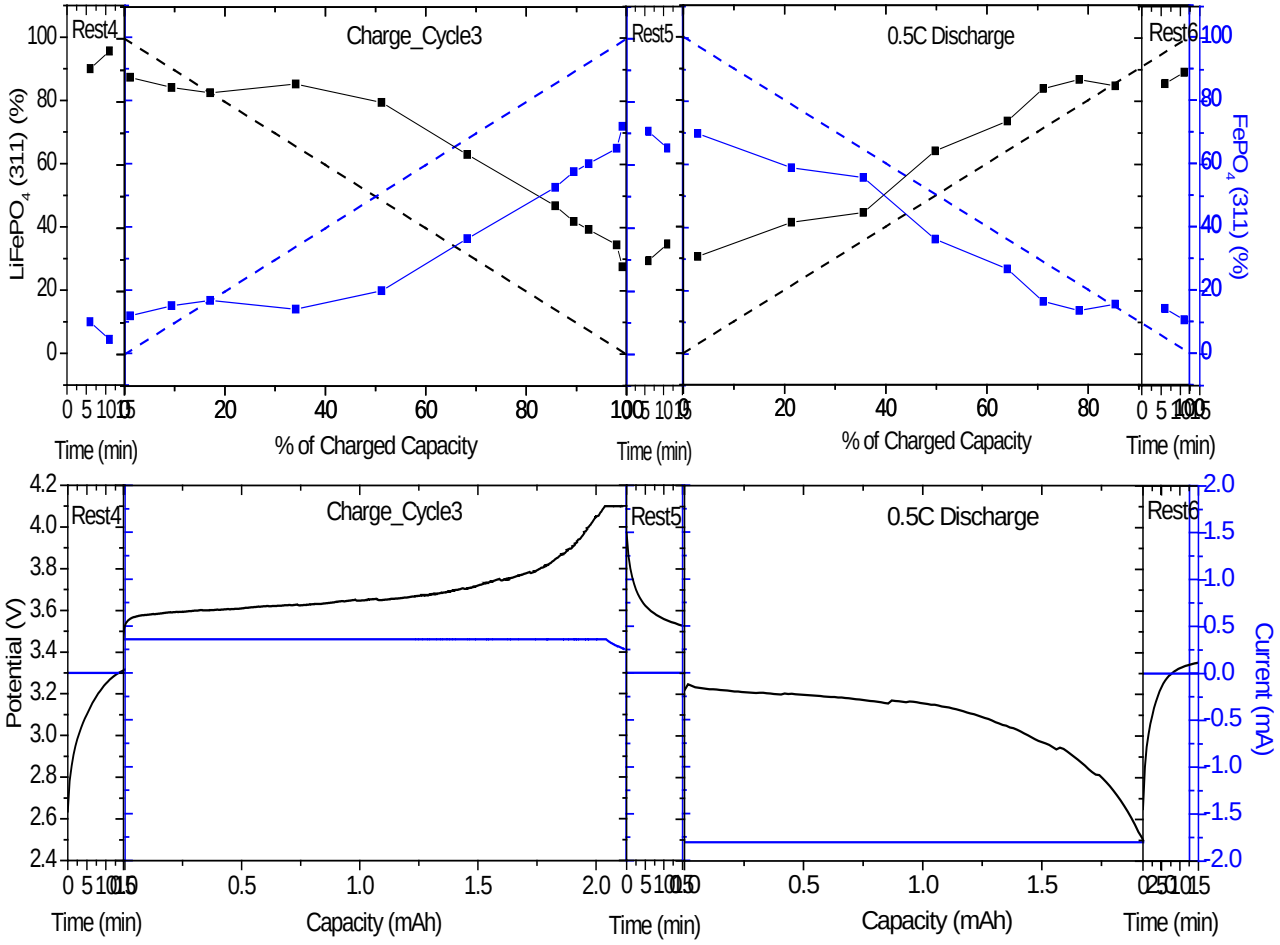

Figure 5.10: (a) Phase transition progress line during electrochemical charge discharge during 3rd cycle (0.5C discharge). The dotted lines indicate the equilibrium progress paths. (b) Electrochemical charge discharge profiles of the 3rd cycle, where blue lines indicate current profile and black lines indicate potential profile.

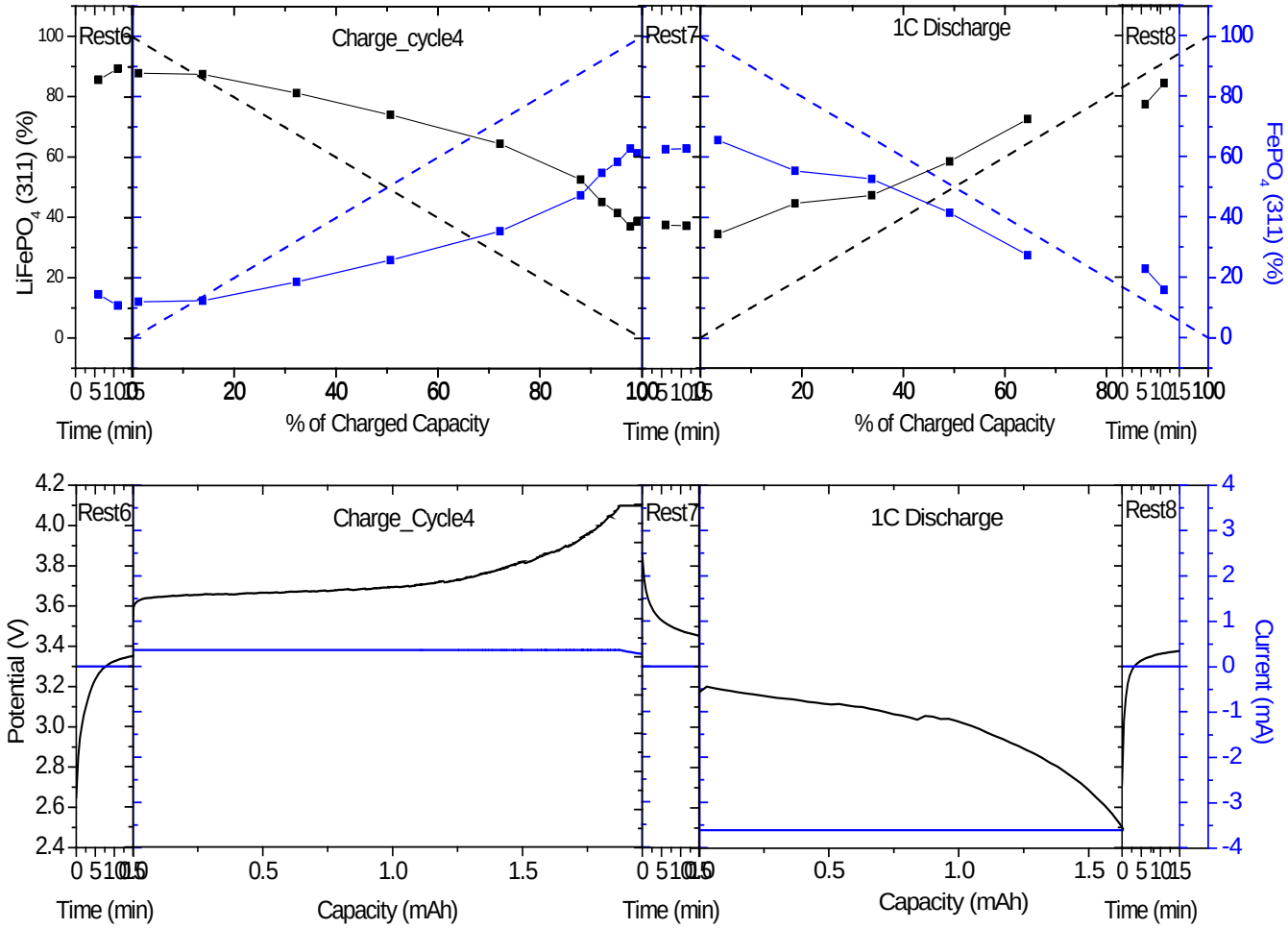

Figure 5.11: (a) Phase transition progress line during electrochemical charge discharge during 4th cycle (1C discharge). The dotted lines indicate the equilibrium progress paths. (b) Electrochemical charge discharge profiles of the 4th cycle, where blue lines indicate current profile and black lines indicate potential profile.

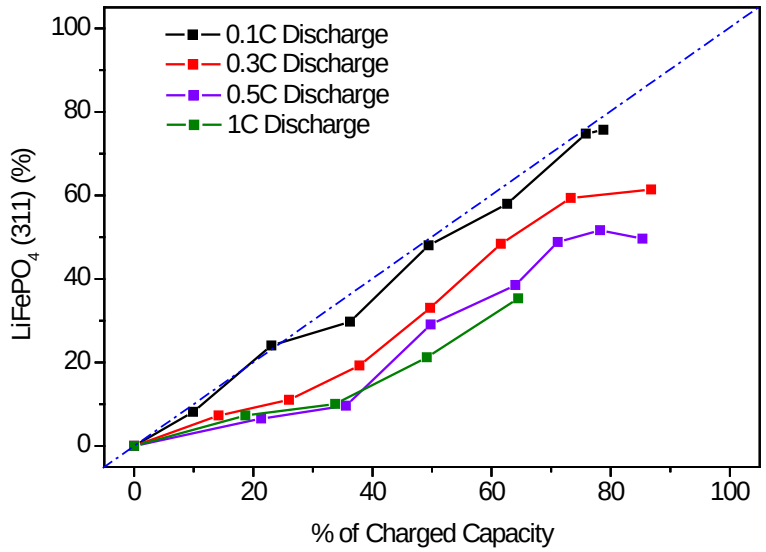

Figure 5.12: Phase transition progress line during electrochemical discharge at all four different discharge rates after the correction of history from the charge process. The dotted line indicates the equilibrium progress path.

5.5 In-situ Raman results vs. in-situ XRD results

Phase transition progress was recorded using the in-situ XRD technique for the four different discharge cycles and was also studied at 0.3C discharge rate using the in-situ Raman spectroscopy. The results from two techniques were compared in Fig. 5.13.

In chapter 4, the results from the in-situ Raman spectroscopy is discussed and it is concluded that in any particle once the phase transition starts, it finishes very quickly within the same particle. But from the in-situ XRD results (Fig. 5.12) it is observed that the progress of the phase transition is gradual and continuous during the entire discharge process. The reason of this difference of phase transition from two different experiments is that two experiments study the same phenomena at two different length scales.

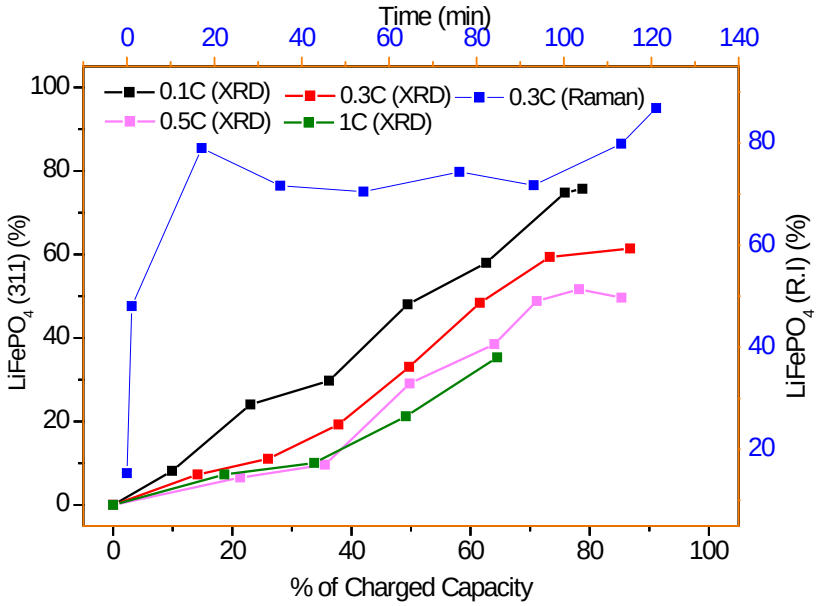

Figure 5.13: Phase transition progress lines obtained during different discharge rates and from in-situ Raman spectroscopy and from in-situ XRD study.

Raman spectroscopy uses the laser with a spot size of 2 μm which only focuses on a few active materials, and hence can safely be considered as the particle level technique. On the other hand, in-situ XRD focuses on a large area which includes many particles. During the discharge process, among these many particles (X-ray irradiated area) at any point some particles started transforming and the transformation finished very quickly on those particles while the rest of the particles did not start yet. This gives the average result from all the particles (X-ray irradiated area). As the discharge process continued more and more particles started transforming, but once transformation starts in any particle, it finishes very quickly in that particle. As a result, the in-situ XRD study actually investigated the fraction of particles that underwent phase transition, rather than the same process within individual particle. The results show that there was a gradual

and continuous phase transformation over the entire period of discharge. This phase transformation mechanism is shown with the help of a simple schematic in Fig. 5.14.

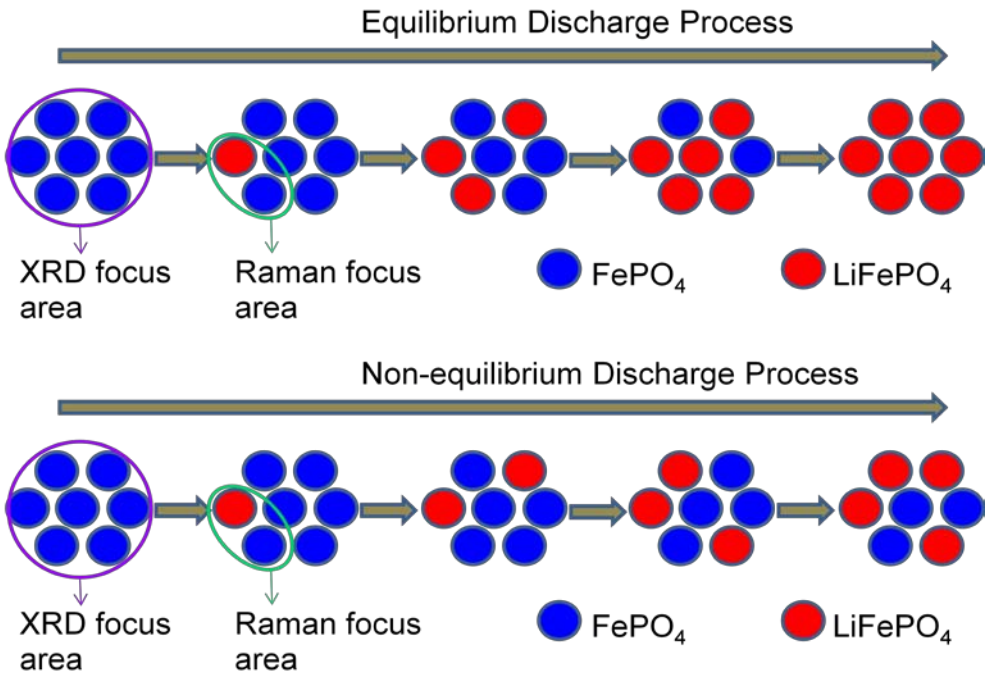

Figure 5.14: Schematic explaining phase transition mechanism during equilibrium and non equilibrium process at slow and high discharge rates. In-situ Raman study area and in-situ XRD study area in the electrodes are also marked in the schematic.

Phase transition delays during fast discharge can also be explained using the same schematic in Fig. 5.14. During fast discharge process, non-equilibrium phase transition was caused by several factors such as, insufficient Li ion availability due to the hindrance of Li ion diffusion through complex porous network, and limited local electronic conductivity. Due to these factors at a high discharge rate, some particles that can start transforming in the slow discharge or in equilibrium could postpone the phase

transformation. The delayed phase transition process is reflected in the in-situ XRD results at higher discharge rates and also in the in-situ Raman results.

5.6 Conclusion

In-situ XRD experiment was designed and employed to study the phase transition mechanism of $LiFePO_4$ material. Four different discharge rates of 0.1C, 0.3C, 0.5C and 1C were tested and analyzed. The key findings were as follows:

1) During charging or discharging processes of all cycles, no noticeable peak shift was observed for both $LiFePO_4$ (311) and $FePO_4$ (311) indicating that only two end members ($LiFePO_4$ and $FePO_4$) exist and no intermediate composition of $Li_{1-x}FePO_4$ or $Li_{x'}FePO_4$ was observed.
2) In the XRD experiment a large area of electrode was probed which has many particles, and hence the XRD results indicate the average of phases present in that large X-ray irradiated area. This gives a gradual and continuous progress of phase transition during the entire discharge or charge process.
3) Results from the XRD experiments do not contradict with the in-situ Raman results; rather it further validates that in any $LiFePO_4$ particle once the phase transition starts, it finishes quickly in that particular particle.
4) Non-equilibrium phase transition was observed at fast discharge process resulting in a delay in phase transition.
5) The in-situ XRD experiments and in-situ Raman experiments are compared and analyzed to establish a phase transition mechanism and pathway.

Chapter 6

Numerical study of phase transition

6.1 Introduction

The phase transformation between the Li-rich phase, β (e.g., $LiFePO_4$) and the Li-deficient phase, α (e.g., $FePO_4$) has been demonstrated to play a critical role in the rate performance of cathode materials, such as Mn^{2+}-doped $LiFePO_4$ [55] and nano-size $LiFePO_4$ [10, 128]. Through in-situ Raman and in-situ XRD experiments, the phase transition phenomena have been already established. The results from those experiments show the presence of phases of nearly stoichiometric end members ($LiFePO_4$ and $FePO_4$) during charge/discharge processes and suggest almost no solid solubility between them. The experiments were done using $LiFePO_4$ of approximately 200 nm and of irregular shape. But reduction of particle size and partial substitution of Fe in $LiFePO_4$ by Mn^{2+} have been found to shrink the miscibility gap, i.e., to increase the solid solution range. Furthermore, two-phase miscibility gap and ion transport during charge and discharge, depends on temperature [60, 129], composition [130], particle size [10, 130], surface coatings [131], particle shapes [132, 133], and discharge rate [7]. And also fast discharge (insertion) or charge (extraction) may lead to a kinetically-induced non-equilibrium phase transformation which affects the miscibility gap. Recent research also demonstrated that phase transformation in $LiFePO_4$ is strongly controlled by the strain energy induced from volume difference between the two phases [134]. Additional energy penalty due to the non-equilibrium phase transformation can further decrease the driving energy for phase transformation, resulting in a decrease of the discharge potential but increase of the charge potential [135]. Although these results demonstrate the

importance of miscibility gap and non-equilibrium phase transformation, the actual mechanisms and the corresponding implications are not clear.

Phase transition of individual $LiFePO_4$ particles of different particle size and shape was studied using a numerical study. Here, in this chapter, a unique Mushy-zone approach is introduced and used to study the phase transition behavior of single particle $LiFePO_4$. Also non-equilibrium phase transition at high discharge rates is studied.

6.2 Mushy Zone Approach

The kinetically-induced non-equilibrium phase transformation can be illustrated by Fig. 6.1. At a low-rate discharge (e.g., C/10 in Fig. 6.1a), a flat plateau appears at around 3.5 V for a $LiFePO_4$-based cathode, corresponding to the two-phase region in the equilibrium phase diagram (Fig. 6.1b). This equilibrium phase separation, as shown by the red curve in Fig. 6.1b, is realized by Li ion diffusion and readjustments in composition at the two-phase interfaces. However, at a high-rate discharge (e.g., 20 C in Fig. 6.1a) the flat plateau may disappear and is instead replaced with a fast decaying curve [136, 137]. These phenomena are more pronounced at lower temperature where Li diffusion is retarded. It is hypothesized that a non-equilibrium phase transformation occurs during fast discharge, where the non-equilibrium miscibility gap shifts to higher Li contents and is represented by the dashed blue line in Fig. 6.1b. The implication of this phenomenon is that the non-equilibrium miscibility gap is significantly expanded, leading to significant reduction in two-phase solubility and battery discharge capacity.

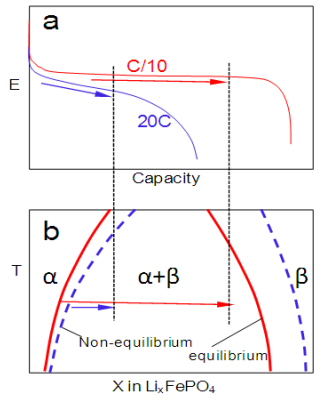

Figure 6.1: Schematic illustration of equilibrium and non-equilibrium phase transformation in (a) battery discharge and (b) phase diagram. α and β are referring to the Li-poor phase ($FePO_4$) and Li-rich phase ($LiFePO_4$), respectively.

Though the well-known “core-shrinking” description [75, 138] has been widely employed to simulate the phase separation between the two solid solution regions outside the miscibility gap; however, it fails to account for the non-equilibrium phenomenon. An approach termed as “mushy-zone” (MZ) approach, has been developed as an effective tool to study the origin and implication of the non-equilibrium phenomenon and also the miscibility gap dynamics during charge/discharge process and particle size and morphology effect.

6.2.1 Model Description

Accounting for non-equilibrium effect.— The rate of phase transformation depends on the interface mobility and Li diffusivity in both the α- and β-phases. Studies conducted by Wang et al.[139, 140] have confirmed the importance of the mixed mode of phase transformation, where the interface mobility is much slower than the Li-ion diffusion in the individual phase. Experimentally, high-resolution TEM images showed that Li insertion and extraction seem to be concentrated at the phase boundary, with

negligible transfer occurring in either the α- or β-phase [42]. Therefore, one possible approach to account for the effect of non-equilibrium phase transformation is to simply implement a sluggish interfacial diffusion coefficient in the continuum diffusion equation. The derivation of the interfacial diffusion coefficient is detailed in the following paragraphs.

Simulation of battery discharge.— Similar to the approach employed by Wang et al, [139, 140] only 1D Li transport within a single particle (plate or sphere) is simulated. The governing equations are

$$\frac{\partial c_{Li}}{\partial t} = D_{Li}\frac{\partial^2 c_{Li}}{\partial x^2} \qquad \text{for plate shaped particle……..6.1}$$

$$\frac{\partial c_{Li}}{\partial t} = \frac{1}{r^2}\frac{\partial}{\partial r}\left(D_{Li}r^2\frac{\partial c_{Li}}{\partial r}\right) \qquad \text{for spherical particle……6.2}$$

with the following boundary conditions

Particle center $x = 0$ or $r = 0$ $j_{Li} = 0$

Particle surface $x = l_0$ or $r = r_0$ $j_{Li} = \frac{i_n}{F}$ ……..6.3

where j_{Li} s the Li flux and i_n is the intercalation current.

Ignoring the anode overpotential and electrolyte resistance, the discharge potential *E* is determined from the discharge kinetics, i.e.,

$$i_n = kc_s^{0.5}.(c_{\max} - c_s)^{0.5} \times \left[\exp\left(\frac{0.5F}{RT}(E - E_0)\right) - \exp\left(-\frac{0.5F}{RT}(E - E_0)\right)\right] \text{……..6.4}$$

where *k* is a lumped factor accounting for both the exchange current and electrolyte concentration, c_s Li concentration at the particle surface, and *F* Faraday constant.

The implementation of the diffusion coefficient within the miscibility gap (either equilibrium or non-equilibrium) is straightforward. The overall Li flux j_{Li} in one-dimension within the two-phase region can be described by

$$j_{Li} = -(1-b)D_{Li,\alpha}\frac{\partial c_{Li,\alpha}}{\partial x} - bD_{Li,\beta}\frac{\partial c_{Li,\beta}}{\partial x} \quad \text{.....6.5}$$

where b is the volume fraction of the β -phase, which is determined by the lever rule.

$$b = \frac{c_{Li} - c^0_{Li,\alpha}}{c^0_{Li,\beta} - c^0_{Li,\alpha}} \qquad \text{when } c^0_{Li,\alpha} < c_{Li} < c^0_{Li,\beta} \quad \text{.....6.6}$$

Within the miscibility gap, the overall Li concentration c_{Li} is

$$c_{Li} = c_{Li,\alpha}(1-b) + bc_{Li,\beta} \quad \text{.....6.7}$$

If at thermodynamic equilibrium, compositions of the two phases at the miscibility gap have the following relationship

$$K_{Li}c_{Li,\alpha} = c_{Li,\beta} \quad \text{.....6.8}$$

Combining Eqns. 6.7 and 6.8, the phase compositions at the miscibility gap can be described by

$$c_{Li,\alpha} = \frac{c_{Li}}{1-b+bK_{Li}}, \qquad c_{Li,\beta} = \frac{K_{Li}c_{Li}}{1-b+bK_{Li}} \quad \text{.....6.9}$$

The Li diffusion flux in the miscibility gap is thus rearranged by substituting Eqn. 6.9 into Eqn. 6.5 as

$$j_{Li} = -(1-b)D_{Li,\alpha}\frac{\partial}{\partial x}\left(\frac{c_{Li}}{1-b+bK_{Li}}\right) - bD_{Li,\beta}\frac{\partial}{\partial x}\left(\frac{K_{Li}c_{Li}}{1-b+bK_{Li}}\right) \quad \text{.....6.10}$$

Rearranging Eqn. 6.10 and comparing with the Fick's first law result in the following two-phase diffusion coefficient of Li

$$D_{Li} = \left[(1-b)D_{Li,\alpha} + K_{Li} b D_{Li,\beta}\right]\left(\frac{1}{1-b+bK_{Li}}\right).f\left(c_{Li}\right) \quad \text{.....6.11}$$

where $f\left(c_{Li}\right)$ is a tunable function accounting for slow interfacial diffusion.

Parameters used in the simulations are listed in Table 6.1. A commercial computational fluid dynamics (CFD) software was used to simulate the single particle phase transition for different particle size and morphology. The codes used in the CFD software to describe the equations and properties of the material are described in Appendices.

Table 6.1: Parameters used in the simulation (Refs. [42, 105])

Parameter	**Value**
Li diffusivity in β phase, $D_{Li,\alpha}$ (m^2/s)	8×10^{-18}
Li diffusivity in α phase, $D_{Li,\beta}$ (m^2/s)	4.8×10^{-17}
Equilibrium Li composition in α phase, $c^0_{Li,\alpha}$ (mol/m^3)	616.5
Surface concentration of Li composition at β phase, $c^0_{Li,\beta}$ (mol/m^3)	19409.4
Partition coefficient of phase β to phase α, K_{Li}	31.48
Maximum Li concentration, $c_{\max}$ (mol/m^3)	22834.6
Cathode kinetic constant, *k*	3.14×10^{-6}
Tunable function $f\left(c_{Li}\right)$ in Eq. 6.11	$Ab^{1.8}$
Equilibrium potential of $LiFePO_4$, E_0 (V)	$3.4245 + 0.85e^{-800\left(c_s/c_{\max}\right)^{-1.3}} - 17e^{-0.98\left(c_s/c_{\max}\right)^{-14}}$

6.2.2 Effect of Diffusivity through two-phase interface

The impact of interfacial Li diffusivity on discharge performance of a sphere is further explored in Fig. 6.2 and Fig. 6.3. At discharge rate of 2C, low Li diffusivity makes the transition between the stages 2 and 3 less pronounced as shown in the inset of Fig. 6.2, indicating significant delay in phase transition. With the increase of Li diffusivity from A~10^{-4} (A is a tunable factor), the discharge capacity first jumps from ~80 $mAhg^{-1}$ to more than 120 $mAhg^{-1}$, and then gradually increases and eventually levels off at around 160 $mAhg^{-1}$ when A reaches ~10^{-3}. At discharge rate of 20C in Fig. 6.3, the slope of the potential flat plateau as seen during low-rate discharge is declining as demonstrated from both the discharge performance curves and the surface composition profiles. When the discharge reaches the stage 2, the surface composition continuously increases till the end of discharge. This is more pronounced for slow interfacial diffusion.

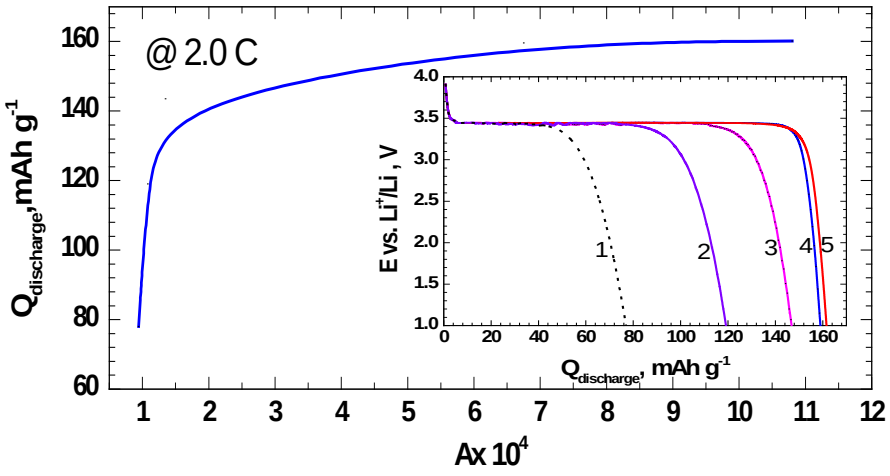

Figure 6.2: Impact of interfacial diffusion coefficient on discharge capacity and battery performance (inset) for a sphere with radius of 20 nm. Values of A in the function $f(c_{Li}) = Ab^{1.8}$ are **1**: 9.45x10^{-5}, **2**: 1.08x10^{-4}, **3**: 1.35x10^{-4}, **4**: 6.74x10^{-4}, and **5:** 1.08x10^{-3}.

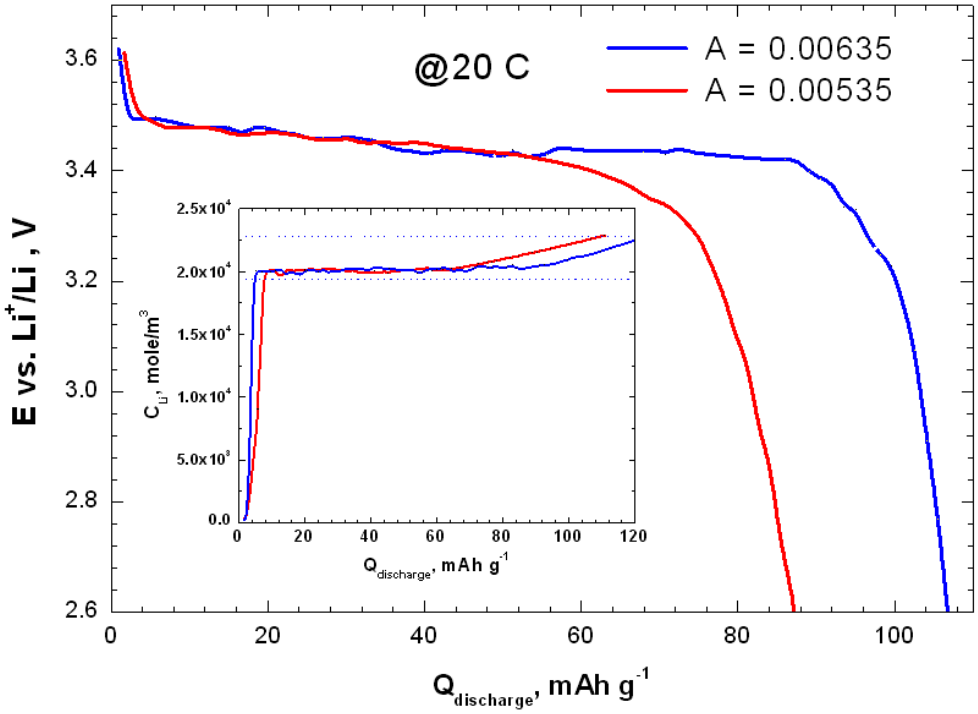

Figure 6.3: Impact of interfacial diffusion coefficient on discharge performance and particle surface composition (inset). The simulation is done for a sphere with radius of 20 nm at discharge rate of 20C. The dash lines in the inset indicate the equilibrium and maximum compositions.

6.2.3 Validation of model using equilibrium simulation

To validate the suitability of the MZ approach the equilibrium phase transformation is studied under low discharge rate and compared with core-shrinking model. This would be a baseline for further study of non-equilibrium phase transformation. The 1D simulation result of a plate at low discharge rate (0.5C) which is believed to be equilibrium phase transformation is shown in Figure 6.4 which compares the Li distribution simulated by the MZ approach with those predicted by the core-shrinking formulation (adopted from Zhang and White [38]). The sharp interfaces and moving boundaries have been successfully predicted by the MZ approach. Figure 6.4

indicates that the two approaches essentially predict almost identical phase compositions and interface locations. Also variation of Li ion distribution at the front and back surface of the plate obtained from two different approaches is compared in Figure 6.5. Here also results from two approaches show very good agreement. Three distinct stages labeled as 1, 2, and 3 in the Figure 6.5 are in agreement with the well-known three stages of phase separation during the discharge. The stage '2' corresponds to the two-phase transformation, and the stages '1' and '3' are for the single-phase transformation either in the α- or β-phases.

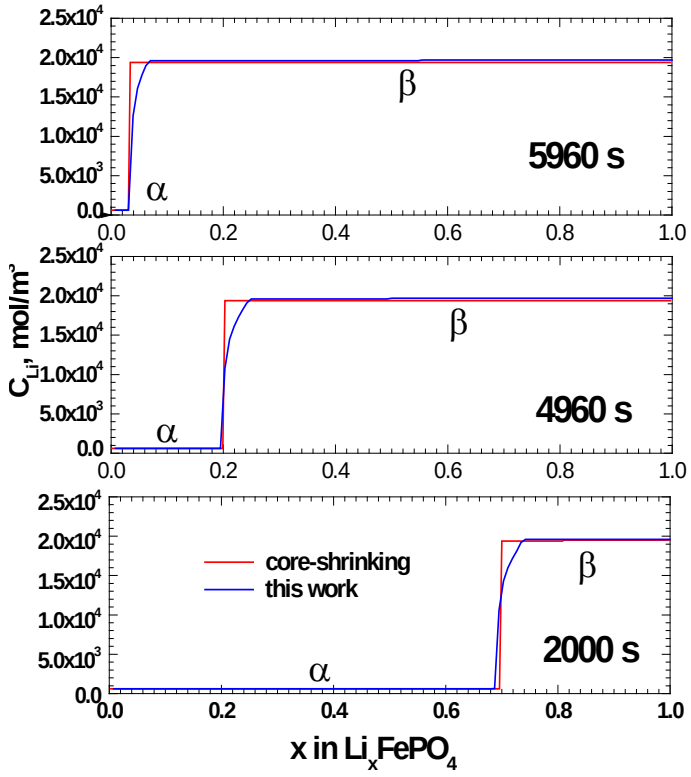

Figure 6.4: Li concentration distribution along the normalized thickness of a 20 nm-thick plate at discharge rate of 0.5C. *A*=0.00135 in $f(c_{Li})$ has been used for the MZ model.

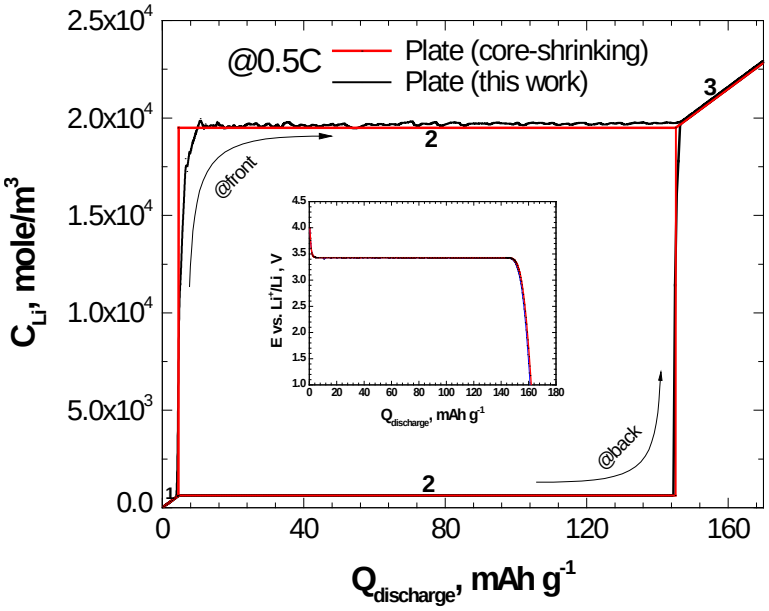

Figure 6.5: Variation of Li concentration at the front and back surfaces of the 20 nm-thick plate during discharge at 0.5C. The inset compares the discharge performance.

6.2.4 Particle Geometry Effect

As the suitability of the MZ approach has been established, the next step is to study the effect of particle shape under non-equilibrium phase transformation. Particle shape is important in phase transformation, since it affects the directions of Li diffusion and moving boundaries. For example, the phase boundary moves unidirectionally in a plate, while convergently toward the center in a sphere. The impact of particle shape is demonstrated in Fig. 6.6. Particles with different shapes show similar discharge performance up to 120 $mAhg^{-1}$, beyond which the sphere experiences a dramatic drop in cell voltage while the plate extends the discharge capacity to ~162 $mAhg^{-1}$. A sharp transition from the stage 2 to stage 3, identified from the surface concentration curve, is

observed for the plate but absent for the sphere. This can be explained by different Li flux across the two-phase interface for different particle shapes, i.e.,

$$\text{Sphere: } J = \frac{L^3 \rho Q_{th} C_{rate}}{3r^2} \qquad \text{Plate: } J = L \rho Q_{th} C_{rate} \quad \text{.....6.12}$$

where Q_{th} is the theoretical capacity, r is the radius of the α-phase core, and L is the radius of the sphere or thickness of the plate ($L = r_0 = l_0$). For the spherical particle, at the beginning of discharge ($r = L$), the Li flux at the particle surface is only one third of that of the plate. However, as discharge proceeds, the two-phase interface between the α- and β-phases shrinks dramatically in the sphere. As a result, the Li flux increases rapidly as a function of r^{-2} (Eqn. 6.12). At r = 0.58L, the two-phase interfacial flux in the sphere equals that in the plate. Upon further discharging, the Li flux across the two-phase boundary may not keep up with the required discharge rate owing to the sluggish Li diffusivity, thus developing the non-equilibrium phenomenon. This generates the gradual increase of the surface composition for the spherical particle in Fig. 6.6. On the other hand, the two-phase interfacial flux in the plate-shaped particles remains constant throughout the entire discharge process.

For higher discharge rate at 2C, Fig. 6.7 clearly indicates that delicate non-equilibrium phase transformation can be brought about by the kinetically-induced process. At the relatively higher discharge rate, Li ion diffusion and readjustments at the miscibility gap may not keep up with the high flux of Li ions from the particle surface. Therefore, equilibrium phase transformation is destroyed and non-equilibrium behavior appears. For a 20 nm-thick plate in Fig. 6.7a, the miscibility gap is found to expand, especially toward the β-phase. The relative expansion ratio of the two-phase miscibility gap is calculated to be 0.8% and 6% at 1C and 2C discharge rates, respectively. Though the expansion ratio at 2C discharge rate is large; however, it might seem that the simulation on a 1D plate

exaggerates the effect of non-equilibrium phase separation, since the Li inflow rate at a plate surface is 3 times of that at a sphere surface (when $r_0=l_0$) at the same discharge rate.

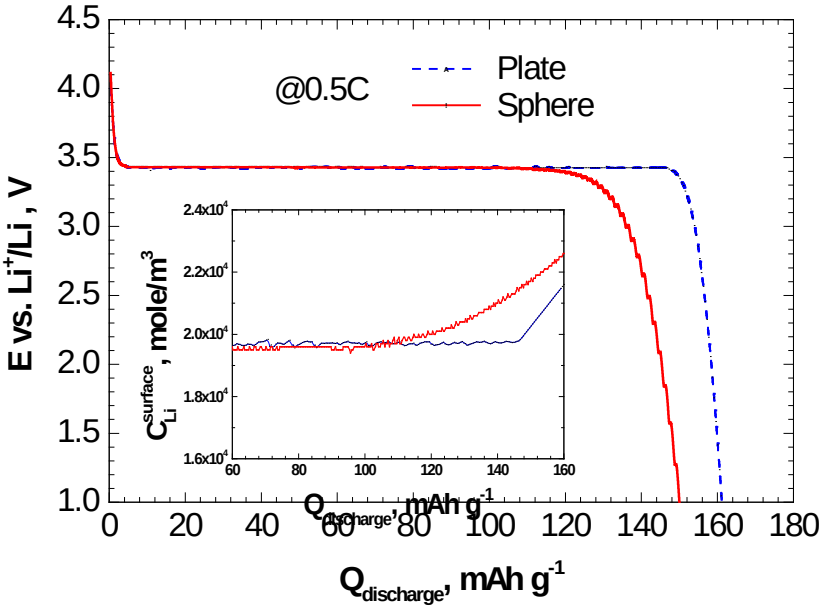

Figure 6.6: Discharge performance of a $LiFePO_4$ plate and a sphere at 0.5C. The inset shows particle surface concentration of Li near completion of discharge.

For a spherical particle in Fig. 6.7b, due to variation of the two-phase interfacial flux during discharge, the sphere first experiences equilibrium phase transformation at early stage of discharge and then non-equilibrium phase transformation upon further discharging. The β-phase composition at the miscibility gap stays at the equilibrium value initially and then increases gradually with the state of discharge (SOD). SOD is defined as the ratio of discharging capacity at a specific point to the full capacity. Near the end of discharge (e.g., SOD=0.833 when r<0.58 L), the miscibility gap expands promptly when significant non-equilibrium phenomenon develops.

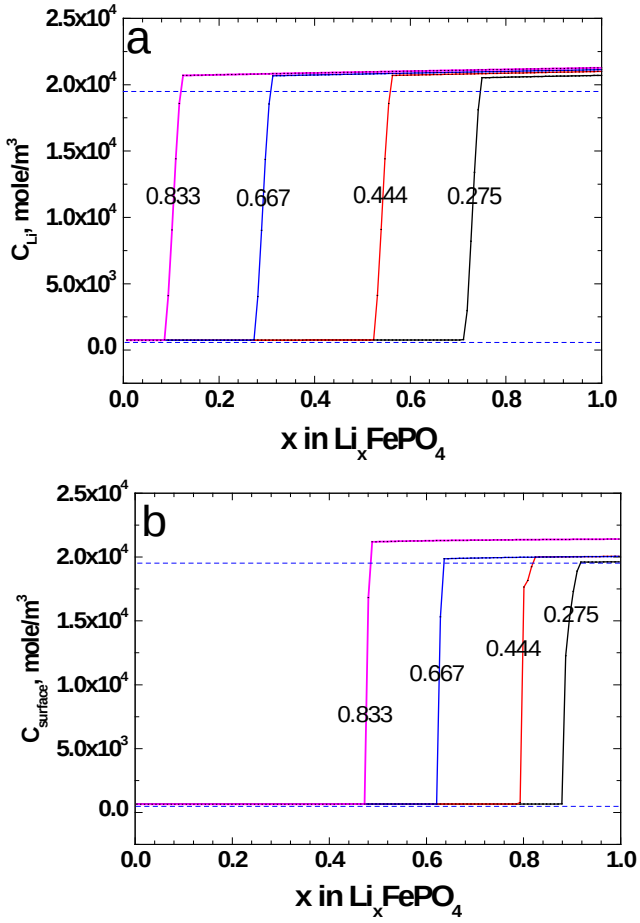

Figure 6.7: Li concentration profiles along the normalized thickness during discharge in (a) a plate (thickness l_0=20 nm) and (b) a sphere (radius r_0=20 nm) at 2C discharge rate. The state-of-discharge is indicated in the figures. The dash lines indicate the thermodynamic equilibrium phase compositions.

The different rate of phase transformation could lead to different discharge behavior of these particles. Interestingly, Fig. 6.8 shows that the curves of capacity as a function of discharge rate for plates and spheres cross at 1.5C. At lower rates, plate-

shaped particles are slightly better but show much lower capacity when discharge rate increases.

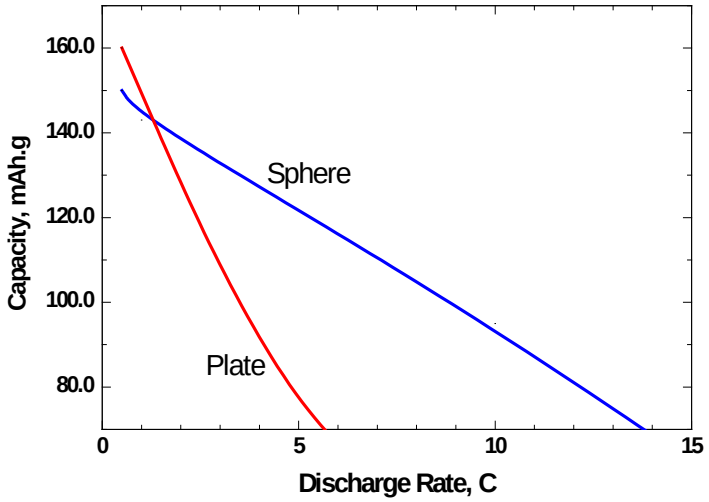

Figure 6.8: Comparison of capacity as a function of discharge rate for plate-shaped and spherical particles.

The interesting observation in Fig. 6.8 can be interpreted by different Li flux across the two-phase interface for different particle shapes [7]. The interfacial Li flux for plate shaped particles remains constant at a discharge rate throughout the entire discharge process, while the flux increases for spherical particles as phase transformation approaches the center of the particles. The ratio of interfacial flux between the two shapes shown in Fig. 6.9 indicates that at the early stage of phase transformation ($r/L > 0.58$ where r is the radius of the $FePO_4$ core and L is the plate thickness), the Li flux (required by the discharge rate) across the two-phase interface is notably smaller for spherical particles; however, as the discharge proceeds till $r/L < 0.58$ the interfacial Li flux in spheres drastically increases due to significant shrinkage of the two-phase interface, and eventually causes the kinetically-induced non-equilibrium phase transformation. As

the interfacial flux spikes near the end of discharge leading to non-equilibrium phase transformation, the core of a $LiFePO_4$ sphere could not be utilized even at an extremely small rate. However, a $LiFePO_4$ plate could be completely accessed as long as the discharge rate is low enough, resulting in a higher discharge capacity. The ratio of *r/L* = 0.58 translates to a discharge capacity of $170 \times (1^3 - 0.58^3) \approx 140$ mAh/g for a $LiFePO_4$ sphere, where 170 is the theoretical capacity (in mAh/g) of $LiFePO_4$ materials. When the discharge rate increases, capacity of $LiFePO_4$ particles in both shapes decreases. However, when the discharge capacity decreases to below 140 mAh/g (*r/L* = 0.58), the lower interfacial Li flux as seen in Fig. 6.9 makes the sphere better utilized and therefore results in a higher capacity. This is why spherical particles show better capacity than the plates at a higher discharge rate. The capacity of 140 mAh/g (*r/L* = 0.58) should therefore correspond to the point where the two curves for plate and sphere cross as shown in Fig. 6.8.

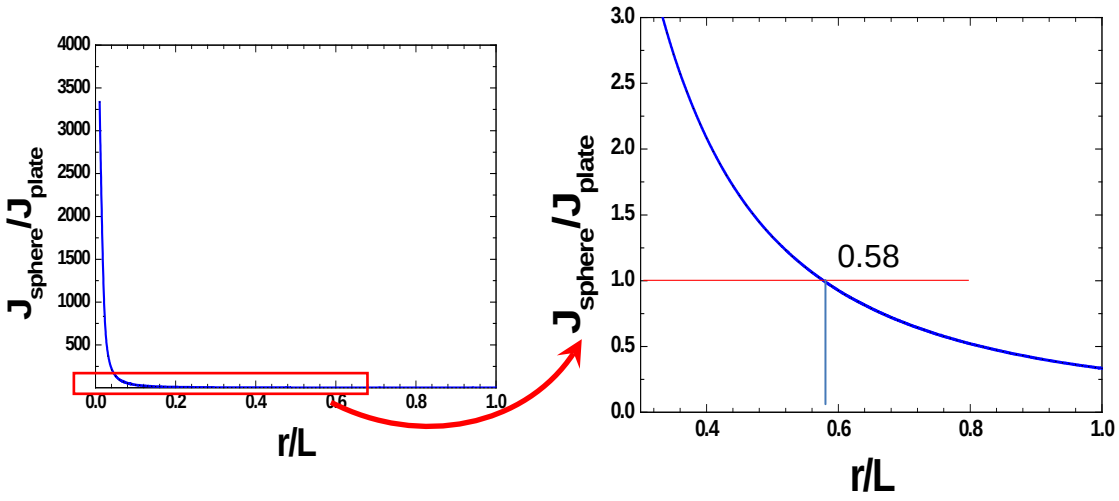

Figure 6.9: Ratio of the Li ion flux at the two-phase interface for two different particle shapes during discharge.

6.2.5 Particle Size Effect

Apart from the significant effect of particle geometry, the effect of particle size also has been studied. Discharge performance of $LiFePO_4$ spherical particles with different sizes was numerically simulated and is shown in Figure 6.10. At low rate (0.5C), capacities of spherical particles with different sizes are almost the same, but at higher rates (1C and 2C) bigger particles show significantly lower capacity. For example, the 20 nm $LiFePO_4$ particle delivers a capacity of 160 mAh/g almost constantly at different discharge rates; however, the 50 nm particle only shows a capacity of 100 mAh/g at a discharge rate of 2C though its capacity is around 160 mAh/g at smaller rate of 0.5C. The fluctuation in some of the discharge curves at high discharge rates or for bigger particles is due to the fact that the potential plateau is calculated based on single particle. The discharge curves we get experimentally are usually from a many particle electrode system where the potential value is an average value from many particles. But for a single particle, at higher discharge rates or bigger particles (non-equilibrium phase transformation) the kinetically induced effects such as diffusion of Li ions, and available Li ions in the adjacent electrolyte cause the fluctuations in the potential plateau.

The influence of particle size on discharge curve at different rates can be explained by the Li flux at the two-phase interface between α (lithium-deficient phase, $FePO_4$) and β (lithium-rich phase, $LiFePO_4$) phases. In Eqn 6.12, r/R (L=R) can be considered as the state of discharge (SOD); a smaller value of r/R ratio translates to a larger SOD (close to the end of discharge). It is evident from Eqn 6.12 that for bigger particles, the lithium flux at the two-phase interface is higher at the same SOD and it becomes more prominent near the end of discharge.

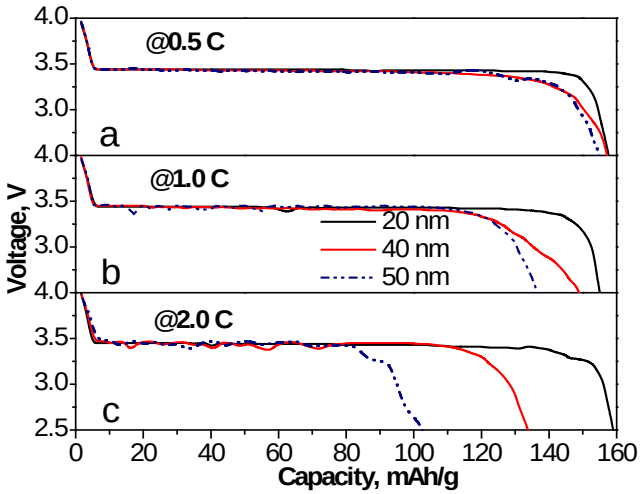

Figure 6.10: Discharge performances of single spherical particle of $LiFePO_4$ at a) 0.5C, b) 1C and c) 2C rate.

Size of the particles also impacts the miscibility gap of the two phase region in the phase diagram. This size dependence of the miscibility gap during the discharge process is shown in Figure 6.11. For a fixed particle size at a constant discharge rate, the miscibility gap slowly increases during the discharge process and increases more rapidly near the end of the discharge. Also, it is evident that the miscibility gap expands more significantly for bigger particles. At lower discharge rate, the miscibility gap does not expand significantly with the particle size. But at higher discharge rate, a little increase in the particle size causes a large expansion in the miscibility gap of the two-phase region. This implies that for bigger particles of active materials, non-equilibrium phase transition can occur at even a low discharge rates. This clearly indicates that non-equilibrium miscibility gap not only relies on temperature, discharging or charging time etc., but also on particle size. This is due to the fact that near the end of the discharge process the sluggish lithium diffusion cannot keep up with the increasing lithium flux at the two-phase

interface demanded by the prescribed discharge rate. As a result, the equilibrium lithium concentrations in the two phases across the boundary cannot be maintained; therefore, the kinetics-controlled non-equilibrium phase transformation occurs and the miscibility gap expands.

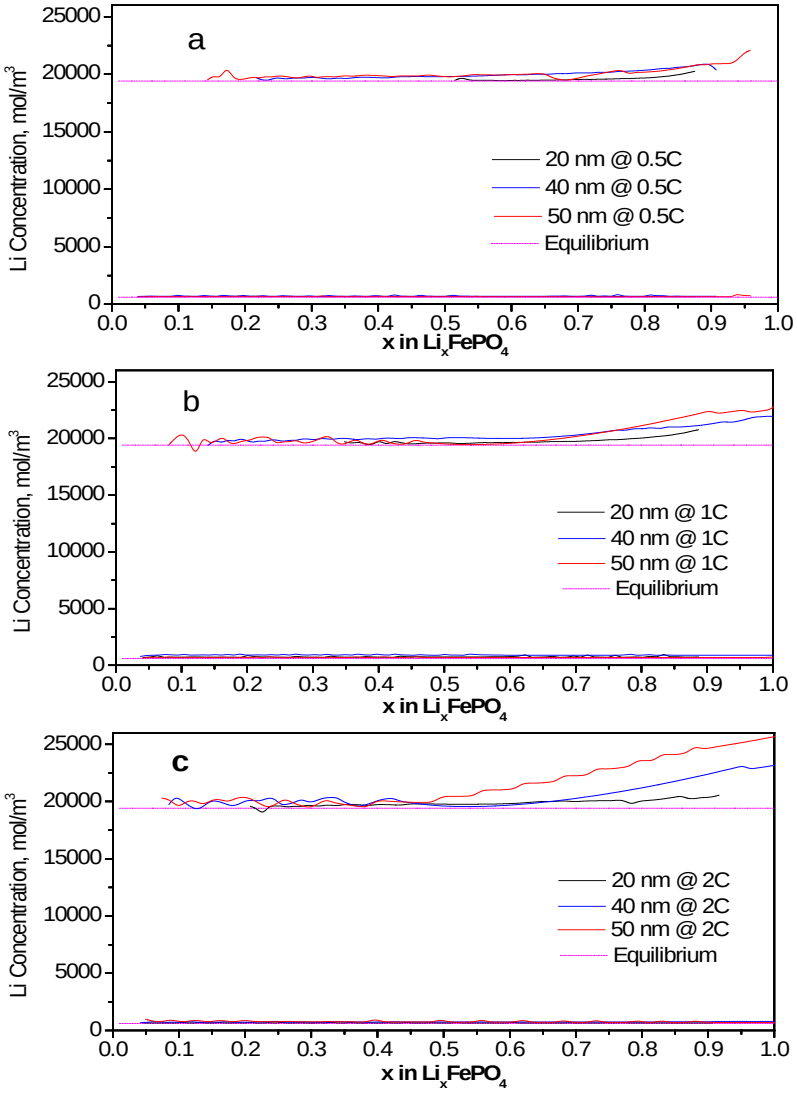

Figure 6.11: Miscibility gap during the discharge process for different particle size at a) 0.5C, b) 1C and c) 2C discharge rate.

6.2.6 Nature of two-phase interface

The nature of the two-phase interface can be understood from the concentration profile at any SOD. At a SOD of 44%, the concentration profiles are shown in Figure 6.12 for two different discharge rates. For lower discharge rates, the interface is wider than that at higher discharge rates, especially for smaller particle size, e.g., 20 nm at 0.5C. And also at the same discharge rate, bigger particles show much narrower two-phase transition. The results indicate that small particle size (<20 nm) and slow discharge rate (<0.5C) tend to create homogenous phase transformation (i.e., small miscibility gap). The results of this study are in good agreement with Meethong et al's [105] experimental discovery that miscibility gap contracts systematically (increased solid solution limits) with decreasing particle size. The results in Figure 6.12 can also be explained from material structure point of view. During the discharge process, when lithium ions enter the active material particles, there comes a mismatch between the de-lithiated α ($FePO_4$) and lithiated β ($LiFePO_4$) phase. When the particle size is smaller, this mismatch is accommodated within several layers of FeO_4 blocks [73]. But when the particle size is bigger, the mismatch between the two phases is accommodated by creation of dislocations and cracks. So, for smaller particles like particles of 20 nm radii show wider two-phase interface, while the 40 nm and 50 nm particles show very sharp two-phase interface.

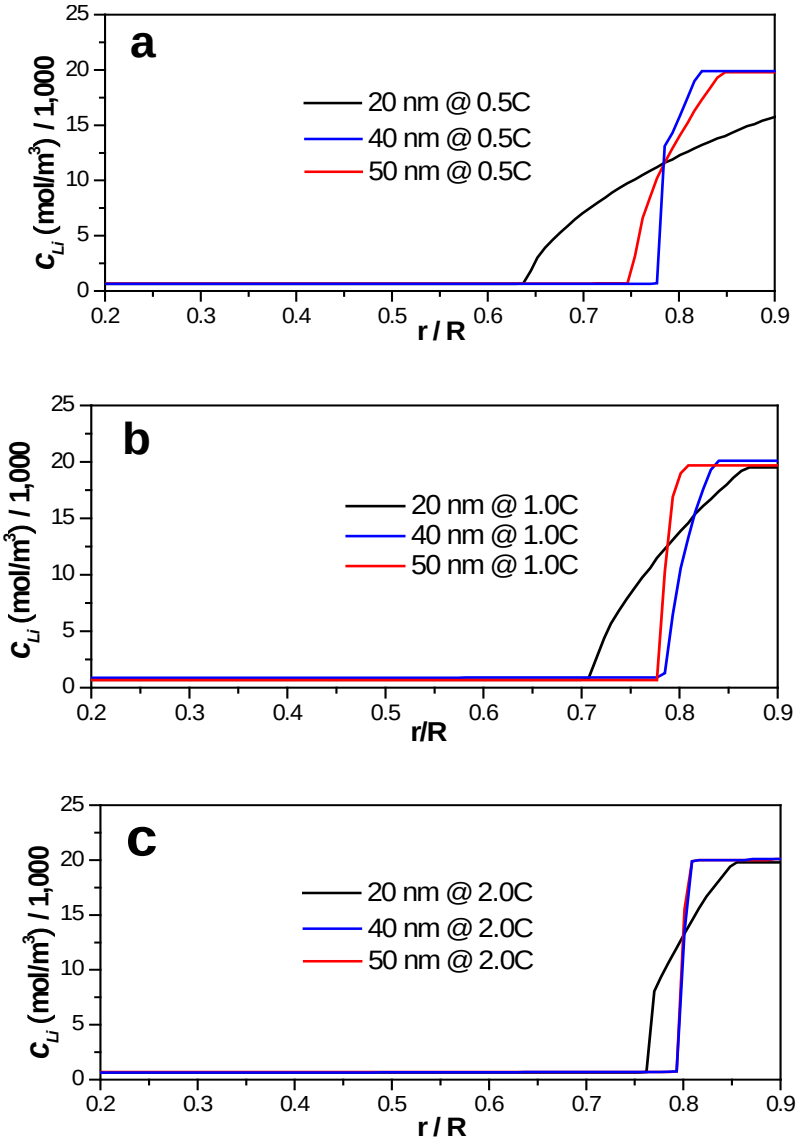

Figure 6.12: Li concentration profiles at SOD of 44% for different particle size at a) 0.5C, b) 1.0C, and c) 2.0C.

To understand the nature of sharp two-phase interface at any stage of discharge, the gradient of chemical potential $\left(d\mu/dr\right)$ for Li ion intercalation is calculated for

different particle sizes. The following Cahn-Hilliard equation was used for 1D Li ion transport [141].

$$\nabla\mu_{Li} = \left\{\left[-2W_c + RT\left[\frac{1}{c} + \frac{1}{(1-c)}\right]\right] \Big/ V_m + C_{1111}.\Delta e_{11}^0.\Delta e_{11}^0 + C_{2222}.\Delta e_{22}^0.\Delta e_{22}^0 + C_{3333}.\Delta e_{33}^0.\Delta e_{33}^0\right\}.\frac{\partial c}{\partial x}$$
$$+\left(2C_{1133}.\Delta e_{11}^0.\Delta e_{33}^0 - 2C_{1122}.\Delta e_{11}^0.\Delta e_{22}^0 - 2C_{2233}.\Delta e_{22}^0.\Delta e_{33}^0\right).\frac{\partial c}{\partial x} - \kappa.\left(\frac{\partial^3 c}{\partial x^3}\right) \quad \ldots 6.13$$

where V_m is the molar volume of stoichiometric $LiFePO_4$, W_c is the regular solution coefficient, C_{ijkl} is the stiffness tensor component, Δe_{ii}^o is linear misfit between the two end members ($LiFePO_4$ and $FePO_4$), and κ is the concentration gradient coefficient. The gradient of chemical potentials for three particle sizes is plotted in Fig. 6.13.

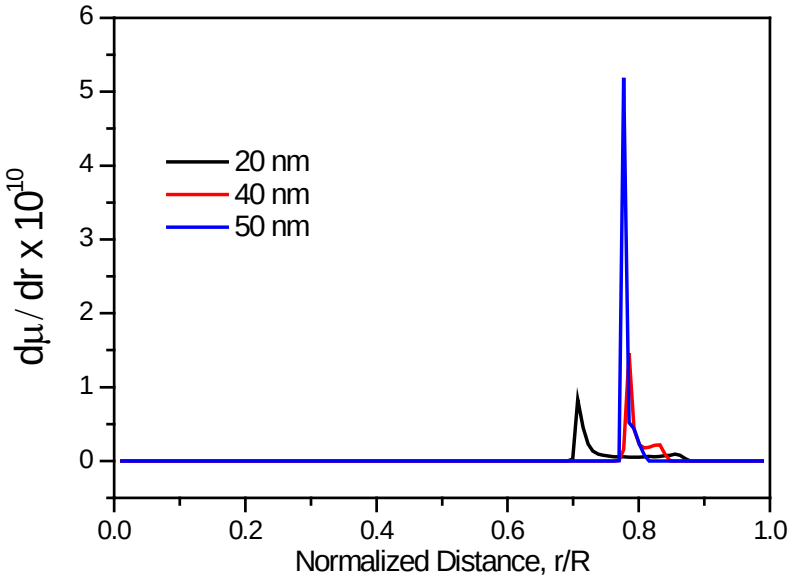

Figure 6.13: Gradient of chemical potentials of spherical particles at 1C discharge rate at 44% SOD (corresponding to Fig. 6.12b).

It is clearly observed that for bigger particle sizes, the change in chemical potential is more drastic than those of smaller ones which is believed to be caused by the sharp two phase interfaces as one sees in Figure 6.12. From a material point of view, the simulated Li concentration in Figure 6.12 and chemical potential gradient shown in Figure 6.13 are determined by the mismatch of structural properties (e.g., structure and lattice parameters) of the two phases presented in the cathode materials.

6.3 Conclusion

The important non-equilibrium phenomena that have pronounced effects on battery discharge performance have been explored, via the unique mushy-zone approach. The non-equilibrium phase transition, occurring due to the fact that sluggish Li diffusion across the two-phase boundaries cannot keep up with the required Li flux at high discharge rate. As a result, the two-phase region in the phase diagram expands and the miscibility gap shifts towards the Li-rich phase. Additionally, particle shape is found to significantly affect the non-equilibrium phase transformation due to different Li flux across the two-phase boundary and therefore different degree of non-equilibrium phase transformation. Growth of $LiFePO_4$ phase follows a well-predicted linear curve in plate-shaped particles; however, two-phase transformation is remarkably delayed for spherical particles, especially at low discharge rates. The different phase transformation behavior leads to different discharge capacity at different rate: at lower rates, plate-shaped particles are slightly better but show much lower discharge capacity when discharge rate increases; at higher discharge rates, spherical particles show better capacity.

Non-equilibrium phase transformation tends to be pronounced for bigger particles even at low discharge rates. It is found that the miscibility gap expands gradually during discharge, which is evident for bigger particles, especially at high rates. Internal

distribution of Li within a particle suggests that small particles (20 nm) tend to create homogenous phase transformation (i.e., no miscibility gap).

It is admitted that experimental validation of the simulation results on individual particle in this work is almost impossible. The conventional battery testing picks up the electrode-level phase transformation information which is thus averaged over multiple particles. Besides, in a complex multi-phase electrode structure the lithiated and delithiated phases may coexist within the same particle or as an assembly of particles [132]. Nevertheless, this study is intended to understand the non-equilibrium phase transformation in individual particle of $LiFePO_4$ and provide fundamental guidance to design high-rate battery materials from a particle-level point of view.

Chapter 7

Conclusion

LIBs have become very popular over the last two decades because of high energy densities in various applications including electric vehicle and portable electronic devices. $LiFePO_4$ material has become one of the most reliable and high performing cathode materials due to its inherent stability and safety features. The phase transition between the two end members (Li rich $LiFePO_4$ and Li poor $FePO_4$) plays a critical role in the performance of the LIB containing this material. And hence in this work this material has been studied to understand their two-phase phase transition behavior.

$LiFePO_4$ material has been synthesized using solid state synthesis method. Material synthesized at 700 ^oC showed an irregular morphology with an average particle size of approximately 200 nm. Phase has been confirmed to be olivine type structure (*Pnma*). Two unique techniques, i.e., in-situ Raman spectroscopy and in-situ XRD, were designed to study the phase transition phenomena in $LiFePO_4$. In-situ Raman studies target the particle-level phenomena while the in-situ XRD studies focus on the phase transformation of the materials at the bulk or electrode level.

A specially designed transparent cell containing a NaCl window was used for the in-situ Raman study. Raman laser spot size was 2 µm while our particle size was approximately 200 nm, which indicates that the Raman laser focused only on a few particles. The particle-level Raman study of $LiFePO_4$ at a slow discharge rate (0.3C) showed that during both charge and discharge the particles under study showed a quick phase transition which is agreement with the domino-cascade model [73]. At the particle level, once the phase transition starts in any $LiFePO_4$ particle, it finishes very quickly while some other particles may not have started the phase transition yet. Thus at any

stage of charge or discharge of a LIB, Raman laser detects either transformed particles or the particles those have not been transformed. At high discharge rates, a phase transition delay has been observed. At high discharge rates, the same particles that show phase transition at slow discharge rates may be completely suppressed and may not go through phase transition depending on the local electronic conductivity and availability of Li ions through porous electrode.

Similarly, the other specially-designed transparent cell that was used in the in-situ XRD equipment was developed. A uniquely-designed electrode containing LiFePO4 was used to make batteries for the in-situ XRD experiments. The battery was tested for four different discharge rates of 0.1C, 0.3C, 0.5C and 1C. For these discharge rates, the phase transition progress curves showed a gradual increase during the entire period of cell discharge. This apparently contradicts the in-situ Raman results. But the in-situ XRD results were discovered on a larger area of a battery electrode that contains lots of active material particles, while the Raman laser probes a very small area that contains only a few particles. Although the electrode structure is heterogeneous, and electronic conductivity, electrolyte porous channels, and other electrochemical parameters can vary throughout the electrode, the electrode is quite homogenous over a small area like 2 μm (the size of the Raman laser spot). Therefore, the particles under the laser during the in-situ Raman study showed either transformed or non-transformed. But for a larger area (XRD study area) that was composed of transformed and non-transformed particles, with the course of discharge the amount of transformed particles increases which gives a gradually and continually increasing phase transition progress curve So, this gradual increase of phase transition is in agreement with the core-shrinking model [75] and indicates that core-shrinking model only works at the bulk level, or the aggregate level. In-situ XRD study also revealed that there was almost no detectable peak position shift

for $LiFePO_4$ and $FePO_4$ phases indicating the presence of only stoichiometric end members ($LiFePO_4$ and $FePO_4$) and no solid solution with the Li_xFePO_4 composition. Besides, the in-situ XRD results also showed that the phase transition was delayed at high discharge rates due to the kinetics-induced non-equilibrium phase transition.

Numerical study using the Mushy Zone approach on individual $LiFePO_4$ particles was performed to investigate the effect of particle size and morphology on phase transition, as well as the miscibility gap dynamics during equilibrium and non-equilibrium phase transition at slow and high discharge rates. It is found that at low discharge rates, the plate shaped particles show higher capacity than spherical particles and at high discharge rate beyond a critical discharge rate, the spherical particles show higher capacity. For spherical particles, the miscibility gap increases exponentially near the end of the discharge process. Particle size of spherical particles plays a key role in phase transition. With the increase of particle size, the miscibility gap becomes wider which makes difficult for the phase transition to be completed. Two phase interface for smaller particles is wide while the large particles show a very sharp and narrow two-phase interface. Large particle and high discharge rates induces the non-equilibrium phase transition. A larger particle can show non-equilibrium behavior at the same discharge rate that gives the equilibrium situation in a small particle.

This study provides a detailed picture of phase transition phenomena in $LiFePO_4$ through both the in-situ Raman and XRD studies that record the phase transition information in real time. And also the numerical study opens up the opportunity to study the same phenomena in a single particle. The results obtained from studies are expected to help to understand the complicated phase transition behavior of $LiFePO_4$ which will eventually shed lights on building high performing and reliable LIBs.

Appendix A

Code for simulating Spherical particles

```
# include "udf.h"
# include "id.h"
# include "mem.h"
# include "sg.h"

#define da 8.0e-18  /* diffusivity in alpha phase, LiFePO4 phase */
#define db 4.8e-17  /* diffusivity in beta phase, FePO4 phase */
#define xb0 616.5352   /* surface concentration at beta phase */
#define xa0 19409.44  /* surface concentration at alpha phase */
#define K 31.48148148  /* partition coefficient of phase 2 to phase 1*/
#define l 20.0e-9  /* particle radius*/
#define liflux 0.5  /* unit C */
#define cmax_c 22834.638  /* max surface concentration cathode calculated assuming
170mAh/g */
#define kb 0.00000314   /* Cathode kinetic constant */
#define R 8.314  /* Universal gas constant */
#define T 298.15  /* Room temperature in absolute scale */
#define F 96485.0  /* Faraday constant */

/* C_UDSI(c,t,0) Li total molar fraction */
/*****************************************************************************/
DEFINE_DIFFUSIVITY(Li_diff,c,t,i)
{
double diff,tt;
double x[ND_ND];
C_CENTROID(x,c,t);
```

```
/* determining volume fraction of phase 2, with smaller D */
if (C_UDSI(c,t,0)<xb0)  diff=db*x[0]*x[0];
else if (C_UDSI(c,t,0)>xa0) diff=da*x[0]*x[0];
else
{tt=(C_UDSI(c,t,0)-xb0)/(xa0-xb0);
diff=((1.0-tt)*db+K*da*tt)*(1.0/(1.0-tt+K*tt))*x[0]*x[0]*0.00235*pow(tt,1.8);
}
return diff;
}
/*****************************************************************************/
DEFINE_PROPERTY(cell_density,c,t)
{
double rho;
double x[ND_ND];
C_CENTROID(x,c,t);
rho=x[0]*x[0]*l*l;
return rho;
}
/*************** calculate discharge curves **********************/
DEFINE_PROFILE(left_in_flux, t, i)
{
cell_t c;
  face_t f;
        begin_f_loop(f,t)
        {F_PROFILE(f,t,i) = 1.0/3.0*liflux/1000.0*170.0*3.6*1000000.0/96485.0*l*l;}
        end_f_loop(f,t)
```

```
}
/************************ calculate Li concentration profiles ************************/
DEFINE_EXECUTE_AT_END(cal_profiles)
{
double x[ND_ND],xx;
Domain *d;
Thread *t;
cell_t c;
FILE *f1;
int i;
real sum=0.;
f1=fopen("profile.txt","a");

fprintf(f1,"%12.8f\n", CURRENT_TIME);
d = Get_Domain(1);
thread_loop_c(t,d)
{
begin_c_loop(c,t)
{C_CENTROID(x,c,t);
if (c==0) {xx=x[0]*0.0;}
fprintf(f1,"%12.8e          %12.8e\n",(x[0]-xx), C_UDSI(c,t,0));}
end_c_loop(c,t)
fprintf(f1,"\n");
}
fclose (f1);
}
```

```
/*************************** calculate discharge curves ***************************/
DEFINE_EXECUTE_AT_END(cal_dis_curves)
{
double yy,Ueq,z,u,y;
Domain *d= Get_Domain(1); /* look up through Boundary panel*/
Thread *t_left = Lookup_Thread(d,5);
int f=0;
FILE *f1;
f1=fopen("dis_curve.txt","a");
yy=F_UDSI(f,t_left,0)/cmax_c;
Ueq=3.4323-5.8428*exp(-80.2493*pow((1-yy),1.3198))-3.2474/1000000.0*exp(20.2645*pow((1-
yy),3.8003))+3.2482/1000000.0*exp(20.2646*pow((1-yy),3.7995));
y=liflux/1000.0*170.0*3.6*1000000.0/96485.0*l/(2.0/F*kb*pow((cmax_c
F_UDSI(f,t_left,0)),0.5)*pow(F_UDSI(f,t_left,0),0.5));
        z=log(y+pow(y*y+1.0,0.5));
        u=z*R*T/0.5/F+Ueq;
fprintf(f1,"%12.8e          %12.8e\n",CURRENT_TIME, u);
fclose (f1);
}
/*********************** calculate surface concentration curves ***********************/
DEFINE_EXECUTE_AT_END(surf_con)
{
Domain *d= Get_Domain(1); /* look up through Boundary panel*/
Thread *t_left = Lookup_Thread(d,5);
face_t f;
FILE *f1;
```

```
f1=fopen("surf_con.txt","a");
begin_f_loop(f, t_left)
{fprintf(f1,"%12.8e          %12.8e\n",CURRENT_TIME, F_UDSI(f,t_left,0));}
end_f_loop(f,t_left)
fclose (f1);
}
/********************** calculate surface concentration curves **********************/
DEFINE_EXECUTE_AT_END(core_con)
{
Domain *d= Get_Domain(1); /* look up through Boundary panel*/
Thread *t_left = Lookup_Thread(d,3);
face_t f;
FILE *f1;
f1=fopen("core_con.txt","a");
begin_f_loop(f, t_left)
{fprintf(f1,"%12.8e          %12.8e\n",CURRENT_TIME, F_UDSI(f,t_left,0));}
end_f_loop(f,t_left)
fclose (f1);
}
```

Appendix B

Code for simulating Plate Shaped particles

```
# include "udf.h"
# include "id.h"
# include "mem.h"
# include "sg.h"

#define da 8.0e-18  /* diffusivity in alpha phase */
#define db 4.8e-17  /* diffusivity in beta phase */
#define xb0 616.5352   /* surface concentration at beta phase */
#define xa0 19409.44  /* surface concentration at alpha phase */
#define K 31.48148148  /* partition coefficient of phase 2 to phase 1*/
#define l 20.0e-9  /* particle length*/
#define liflux 0.5  /* unit C */
#define cmax_c 22834.638  /* max surface concentration cathode calculated assuming
170mAh/g */
#define kb 0.00000314   /* Cathode kinetic constant */
#define R 8.314  /* Universal gas constant */
#define T 298.15  /* Room temperature in absolute scale */
#define F 96485.0  /* Faraday constant */
/* C_UDSI(c,t,0) Li total molar fraction */
/*****************************************************************************/
DEFINE_DIFFUSIVITY(Li_diff,c,t,i)
{
double diff,tt;
/* determining volume fraction of phase 2, with smaller D */
if (C_UDSI(c,t,0)<xb0)  diff=db/l/l;
```

```
else if (C_UDSI(c,t,0)>xa0) diff=da/l/l;
else
{tt=(C_UDSI(c,t,0)-xb0)/(xa0-xb0);
diff=((1.0-tt)*db+K*da*tt)*(1.0/(1.0-tt+K*tt))/l/l*0.00235*pow(tt,1.8);
}
return diff;
}
/*************** calculate discharge curves **********************/
DEFINE_PROFILE(left_in_flux, t, i)
{
  cell_t c;
  face_t f;
        begin_f_loop(f,t)
        {F_PROFILE(f,t,i) = liflux/1000.0*170.0*3.6*1000000.0/96485.0;}
        end_f_loop(f,t)
}
/************************ calculate concentration profiles ************************/
DEFINE_EXECUTE_AT_END(cal_profiles)
{
double x[ND_ND],xx;
Domain *d;
Thread *t;
cell_t c;
FILE *f1;
int i;
```

```
real sum=0.;
f1=fopen("profile.txt","a");
fprintf(f1,"%12.8f\n", CURRENT_TIME);
d = Get_Domain(1);
thread_loop_c(t,d)
{
begin_c_loop(c,t)
{C_CENTROID(x,c,t);
if (c==0) {xx=x[0];}
fprintf(f1,"%12.8e          %12.8e\n",(x[0]-xx), C_UDSI(c,t,0));}
end_c_loop(c,t)
fprintf(f1,"\n");
}
fclose (f1);
}
/************************ calculate discharge curves ************************/
DEFINE_EXECUTE_AT_END(cal_dis_curves)
{
real yy,Ueq;
Domain *d= Get_Domain(1); /* look up through Boundary panel*/
Thread *t_left = Lookup_Thread(d,3);
face_t f;
 int n,js,m,i;
double z,y,z1,y1,z0,y0,xn;
double a,b,h,eps;
```

```
FILE *f1;
a=2.0;
b=5.0;
h=0.1;
eps=0.00000001;
m=1;
f1=fopen("dis_curve.txt","a");
begin_f_loop(f, t_left)
{
yy=F_UDSI(f,t_left,0)/cmax_c;
Ueq=3.4323-5.8428*exp(-80.2493*pow((1-yy),1.3198))-
3.2474/1000000.0*exp(20.2645*pow((1-
yy),3.8003))+3.2482/1000000.0*exp(20.2646*pow((1-yy),3.7995));
 n=0; z=a;
y=liflux/1000.0*170.0*3.6*1000000.0/96485.0*l-1.0/F*kb*pow((cmax_c-
F_UDSI(f,t_left,0)),0.5)*pow(F_UDSI(f,t_left,0),0.5)*(exp(0.5*F/R/T*(z-Ueq))-exp(-
0.5*F/R/T*(z-Ueq)));
            while ((z<=b+h/2.0)&&(n!=m))
     { if (fabs(y)<eps)
        { n=n+1; xn=z;
          z=z+h/2.0; y=liflux/1000.0*170.0*3.6*1000000.0/96485.0*l-
1.0/F*kb*pow((cmax_c-
F_UDSI(f,t_left,0)),0.5)*pow(F_UDSI(f,t_left,0),0.5)*(exp(0.5*F/R/T*(z-Ueq))-exp(-
0.5*F/R/T*(z-Ueq)));
        }
```

```
        else
         { z1=z+h; y1=liflux/1000.0*170.0*3.6*1000000.0/96485.0*l-1.0/F*kb*pow((cmax_c-
F_UDSI(f,t_left,0)),0.5)*pow(F_UDSI(f,t_left,0),0.5)*(exp(0.5*F/R/T*(z1-Ueq))-exp(-
0.5*F/R/T*(z1-Ueq)));
            if (fabs(y1)<eps)
             { n=n+1; xn=z1;
               z=z1+h/2.0; y=liflux/1000.0*170.0*3.6*1000000.0/96485.0*l-
1.0/F*kb*pow((cmax_c-
F_UDSI(f,t_left,0)),0.5)*pow(F_UDSI(f,t_left,0),0.5)*(exp(0.5*F/R/T*(z-Ueq))-exp(-
0.5*F/R/T*(z-Ueq)));
              }
            else if (y*y1>0.0)
             { y=y1; z=z1;}
            else
             { js=0;
               while (js==0)
                { if (fabs(z1-z)<eps)
                    { n=n+1; xn=(z1+z)/2.0;
                      z=z1+h/2.0; y=liflux/1000.0*170.0*3.6*1000000.0/96485.0*l-
1.0/F*kb*pow((cmax_c-
F_UDSI(f,t_left,0)),0.5)*pow(F_UDSI(f,t_left,0),0.5)*(exp(0.5*F/R/T*(z-Ueq))-exp(-
0.5*F/R/T*(z-Ueq)));
                       js=1;
                    }
                  else
```

```
                { z0=(z1+z)/2.0; y0=liflux/1000.0*170.0*3.6*1000000.0/96485.0*l-
1.0/F*kb*pow((cmax_c-
F_UDSI(f,t_left,0)),0.5)*pow(F_UDSI(f,t_left,0),0.5)*(exp(0.5*F/R/T*(z0-Ueq))-exp(-
0.5*F/R/T*(z0-Ueq)));
                  if (fabs(y0)<eps)
                   { xn=z0; n=n+1; js=1;
                     z=z0+h/2.0; y=liflux/1000.0*170.0*3.6*1000000.0/96485.0*l-
1.0/F*kb*pow((cmax_c-
F_UDSI(f,t_left,0)),0.5)*pow(F_UDSI(f,t_left,0),0.5)*(exp(0.5*F/R/T*(z-Ueq))-exp(-
0.5*F/R/T*(z-Ueq)));
                    }
                  else if ((y*y0)<0.0)
                   { z1=z0; y1=y0;}
                  else { z=z0; y=y0;}
                }
              }
            }
          }
fprintf(f1,"%12.8e          %12.8e\n",CURRENT_TIME, xn);
} end_f_loop(f,t_left)
fclose (f1);
}
/************************* calculate interfacial values ************************/
DEFINE_EXECUTE_AT_END(cal_interface)
```

```
{
double min,max,xx,yy;
Domain *d;
Thread *t;
cell_t c;
int c_max,c_min;
FILE *f1;
int i;
real sum=0.;
f1=fopen("interface.txt","a");
min=1000.0;
max=-1000.0;
d = Get_Domain(1);
thread_loop_c(t,d)
{
begin_c_loop(c,t)
        {
                if((c<123)&&(c>3))
                        {
                        C_UDSI(c,t,1)=C_UDSI_G(c,t,0)[0];
        C_UDSI(c,t,2)=C_UDSI_G(c,t,1)[0];
                if ((C_UDSI(c,t,2)>max)&&(C_UDSI(c,t,0)<xb0*1.1)) max=C_UDSI(c,t,2);
                if ((C_UDSI(c,t,2)<min)&&(C_UDSI(c,t,0)>xa0*0.95)) min=C_UDSI(c,t,2);
                        }
        }
```

```
end_c_loop(c,t)
begin_c_loop(c,t)
        {
                if (C_UDSI(c,t,2)==max) c_max=c;
                        if (C_UDSI(c,t,2)==min) c_min=c;
        }
end_c_loop(c,t)
   fprintf(f1,"%12.8e       ",CURRENT_TIME);
        fprintf(f1,"%12.8e          ",C_UDSI(c_max,t,0));
        fprintf(f1,"%12.8e\n",C_UDSI(c_min,t,0));
} /* end of thread loop*/
fclose (f1);
}
```

References

[1] Pistoia G, 'Lithium-Ion Batteries: Advances and Applications', Elsevier, 2014, p:2

[2] Quinn W, 'Lithium Mining', Greeniacs, 2010.19 April 2012. http://www.greeniacs.com/GreeniacsArticles/Energy/Lithium-Mining.html.

[3] 'Cell Chemistries', Woodbank Communications Ltd, 2005. http://www.mpoweruk.com/chemistries.htm.

[4] Padhi AK, Nanjundaswamy KS, Goodenough JB, 'Phospho-olivines as Positive Electrode Materials for Rechargeable Lithium Batteries', Journal of The Electrochemical Society (1997) Vol:144, p:1188-1194.

[5] Akimoto J, Gotoh Y, Oosawa Y, 'Synthesis and Structure Refinement of $LiCoO_2$ Single Crystals', Journal of Solid State Chemistry (1998) Vol:141, p:298-302.

[6] Belharouak I, Vissers D, Amine K, 'Thermal Stability of the $Li(Ni_{0.8}Co_{0.15}Al_{0.05})O_2$ Cathode in the Presence of Cell Components', Journal of The Electrochemical Society (2006) Vol:153, p:A2030-A2035.

[7] Liu F, Siddique NA, Mukherjee PP, 'Nonequilibrium Phase Transformation and Particle Shape Effect in $LiFePO_4$ Materials for Li-Ion Batteries', Electrochemical and Solid-State Letters (2011) Vol:14, p:A143-A147.

[8] La Mantia F, Rosciano F, Tran N, Novak P, 'Direct evidence of oxygen evolution from Li_{1+x} $(Ni_{1/3}Mn_{1/3}Co_{1/3})_{1-x}O_2$ at high potentials', Journal of Applied Electrochemistry (2008) Vol:38, p:893-896.

[9] Thongtem T, Thongtem S, 'Characterization of $Li_{1-x}Ni_{1+x}O_2$ prepared using succinic acid as a complexing agent', Inorganic Materials (2006) Vol:42, p:202-209.

[10] Nam KT, Kim D-W, Yoo PJ, Chiang C-Y, Meethong N, Hammond PT, Chiang Y-M, Belcher AM, 'Virus-Enabled Synthesis and Assembly of Nanowires for Lithium Ion Battery Electrodes', Science (2006) Vol:312, p:885-888.

[11] Wang Z, Su S, Yu C, Chen Y, Xia D, 'Synthesises, characterizations and electrochemical properties of spherical-like $LiFePO_4$ by hydrothermal method', Journal of Power Sources (2008) Vol:184, p:633-636.

[12] Hwang B-J, Hsu K-F, Hu S-K, Cheng M-Y, Chou T-C, Tsay S-Y, Santhanam R, 'Template-free reverse micelle process for the synthesis of a rod-like $LiFePO_4$/C composite cathode material for lithium batteries', Journal of Power Sources (2009) Vol:194, p:515-519.

[13] Joachin H, Kaun TD, Zaghib K, Prakash J, 'Electrochemical and Thermal Studies of Carbon-Coated $LiFePO_4$ Cathode', Journal of The Electrochemical Society (2009) Vol:156, p:A401-A406.

[14] Yang J, Xu JJ, 'Nonaqueous Sol-Gel Synthesis of High-Performance $LiFePO_4$', Electrochemical and Solid-State Letters (2004) Vol:7, p:A515-A518.

[15] Chen YH, Wang CW, Liu G, Song XY, Battaglia VS, Sastry AM, 'Selection of Conductive Additives in Li-Ion Battery Cathodes: A Numerical Study', Journal of The Electrochemical Society (2007) Vol:154, p:A978-A986.

[16] Sharma N, Guo X, Du G, Guo Z, Wang J, Wang Z, Peterson VK, 'Direct Evidence of Concurrent Solid-Solution and Two-Phase Reactions and the Nonequilibrium Structural Evolution of $LiFePO_4$', Journal of the American Chemical Society (2012) Vol:134, p:7867-7873.

[17] Yuan L-X, Wang Z-H, Zhang W-X, Hu X-L, Chen J-T, Huang Y-H, Goodenough JB, 'Development and challenges of $LiFePO_4$ cathode material for lithium-ion batteries', Energy & Environmental Science Vol:4, p:269-284.

[18] Goodenough JB, Kim Y, 'Challenges for Rechargeable Li Batteries', Chemistry of Materials (2009) Vol:22, p:587-603.

[19] Ge M, Rong J, Fang X, Zhou C, 'Porous Doped Silicon Nanowires for Lithium Ion Battery Anode with Long Cycle Life', Nano Letters (2012) Vol:12, p:2318-2323.

[20] Morita T, Takami N, 'Nano Si Cluster-SiO_x-C Composite Material as High-Capacity Anode Material for Rechargeable Lithium Batteries', Journal of The Electrochemical Society (2006) Vol:153, p:A425-A430.

[21] Yang J, Wang BF, Wang K, Liu Y, Xie JY, Wen ZS, 'Si/C Composites for High Capacity Lithium Storage Materials', Electrochemical and Solid-State Letters (2003) Vol:6, p:A154-A156.

[22] Kim I-S, Kumta PN, 'High capacity Si/C nanocomposite anodes for Li-ion batteries', Journal of Power Sources (2004) Vol:136, p:145-149.

[23] Zhao Y, Li J, Wang N, Wu C, Dong G, Guan L, 'Fully Reversible Conversion between SnO_2 and Sn in SWNTs@SnO_2@PPy Coaxial Nanocable As High Performance Anode Material for Lithium Ion Batteries', The Journal of Physical Chemistry C (2012) Vol:116, p:18612-18617.

[24] Wang J, Zhao H, Yang Q, Wang C, Lv P, Xia Q, '$Li_4Ti_5O_{12}$ - TiO_2 composite anode material for lithium-ion batteries', Journal of Power Sources (2013) Vol:222, p:196-201.

[25] Li Y, Pan GL, Liu JW, Gao XP, 'Preparation of $Li_4Ti_5O_{12}$ Nanorods as Anode Materials for Lithium-Ion Batteries', Journal of The Electrochemical Society (2009) Vol:156, p:A495-A499.

[26] Du Pasquier A, Huang CC, Spitler T, 'Nano $Li_4Ti_5O_{12}$ - $LiMn_2O_4$ batteries with high power capability and improved cycle-life', Journal of Power Sources (2009) Vol:186, p:508-514.

[27] Valoen LO, Reimers JN, 'Transport Properties of $LiPF_6$-Based Li-Ion Battery Electrolytes', Journal of The Electrochemical Society (2005) Vol:152, p:A882-A891.

[28] Moumouzias G, Ritzoulis G, Siapkas D, Terzidis D, 'Comparative study of $LiBF_4$, $LiAsF_6$, $LiPF_6$, and $LiClO_4$ as electrolytes in propylene carbonate-diethyl carbonate solutions for $Li/LiMn_2O_4$ cells', Journal of Power Sources (2003) Vol:122, p:57-66.

[29] Sequeira CAC, Hooper A, 'The study of lithium electrode reversibility against $(PEO)_xLiF_3CSO_3$ polymeric electrolytes', Solid State Ionics (1983) Vol:9-10, Part 2, p:1131-1138.

[30] Guyomard D, Tarascon JM, 'High voltage stable liquid electrolytes for $Li_{1+x}Mn_2O_4$/carbon rocking-chair lithium batteries', Journal of Power Sources (1995) Vol:54, p:92-98.

[31] Ein-Eli Y, 'Dimethyl carbonate (DMC) electrolytes - the effect of solvent purity on Li-ion intercalation into graphite anodes', Electrochemistry Communications (2002) Vol:4, p:644-648.

[32] Whittingham MS, 'Lithium Batteries and Cathode Materials', Chemical Reviews (2004) Vol:104, p:4271-4302.

[33] Takahashi Y, Tode S, Kinoshita A, Fujimoto H, Nakane I, Fujitani S, 'Development of Lithium-Ion Batteries with a $LiCoO_2$ Cathode Toward High Capacity by Elevating Charging Potential', Journal of The Electrochemical Society (2008) Vol:155, p:A537-A541.

[34] Amatucci GG, Tarascon JM, Klein LC, 'Cobalt dissolution in $LiCoO_2$-based non-aqueous rechargeable batteries', Solid State Ionics (1996) Vol:83, p:167-173.

[35] Ohzuku T, Ueda A, 'Solid-State Redox Reactions of $LiCoO_2$ (R_{3m}) for 4 Volt Secondary Lithium Cells', Journal of The Electrochemical Society (1994) Vol:141, p:2972-2977.

[36] Baek B, Jung C, 'Enhancement of the Li^+ ion transfer reaction at the $LiCoO_2$ interface by 1,3,5-trifluorobenzene', Electrochimica Acta (2010) Vol:55, p:3307-3311.

[37] Inaba M, Iriyama Y, Ogumi Z, Todzuka Y, Tasaka A, 'Raman study of layered rock-salt $LiCoO_2$ and its electrochemical lithium deintercalation', Journal of Raman Spectroscopy (1997) Vol:28, p:613-617.

[38] Zhang Q, White RE, 'Moving Boundary Model for the Discharge of a $LiCoO_2$ Electrode', Journal of The Electrochemical Society (2007) Vol:154, p:A587-A596.

[39] Liu H, Yang Y, Zhang J, 'Reaction mechanism and kinetics of lithium ion battery cathode material $LiNiO_2$ with CO_2', Journal of Power Sources (2007) Vol:173, p:556-561.

[40] Rougier A, Gravereau P, Delmas C, 'Optimization of the Composition of the $Li_{1-z}Ni_{1+z}O_2$ Electrode Materials: Structural, Magnetic, and Electrochemical Studies', Journal of The Electrochemical Society (1996) Vol:143, p:1168-1175.

[41] Xie J, Tanaka T, Imanishi N, Matsumura T, Hirano A, Takeda Y, Yamamoto O, 'Li-ion transport kinetics in $LiMn_2O_4$ thin films prepared by radio frequency magnetron sputtering', Journal of Power Sources (2008) Vol:180, p:576-581.

[42] Chen Z, Amine K, 'Capacity Fade of $Li_{1+x}Mn_{2-x}O_4$-Based Lithium-Ion Cells', Journal of The Electrochemical Society (2006) Vol:153, p:A316-A320.

[43] Darling R, Newman J, 'Modeling Side Reactions in Composite $Li_yMn_2O_4$ Electrodes', Journal of The Electrochemical Society (1998) Vol:145, p:990-998.

[44] Huang W, Frech R, 'In situ Raman spectroscopic studies of electrochemical intercalation in $Li_xMn_2O_4$-based cathodes', Journal of Power Sources (1999) Vol:81-82, p:616-620.

[45] Wu F, Wang L, Wu C, Bai Y, Wang F, 'Study on $Li_{1+x}V_3O_8$ synthesized by microwave sol-gel route', Materials Chemistry and Physics (2009) Vol:115, p:707-711.

[46] Liu J, Manthiram A, 'Understanding the Improvement in the Electrochemical Properties of Surface Modified 5 V $LiMn_{1.42}Ni_{0.42}Co_{0.16}O_4$ Spinel Cathodes in Lithium-ion Cells', Chemistry of Materials (2009) Vol:21, p:1695-1707.

[47] Zhou J, Notten PHL, 'Studies on the degradation of Li-ion batteries by the use of microreference electrodes', Journal of Power Sources (2008) Vol:177, p:553-560.

[48] Yamada A, Chung SC, Hinokuma K, 'Optimized $LiFePO_4$ for Lithium Battery Cathodes', Journal of The Electrochemical Society (2001) Vol:148, p:A224-A229.

[49] Feng CQ, Wang SY, Zeng R, Guo ZP, Konstantinov K, Liu HK, 'Synthesis of spherical porous vanadium pentoxide and its electrochemical properties', Journal of Power Sources (2008) Vol:184, p:485-488.

[50] Liu Y, Zhou X, Guo Y, 'Structure and electrochemical performance of LiV_3O_8 synthesized by solid-state routine with quenching in freezing atmosphere', Materials Chemistry and Physics (2009) Vol:114, p:915-919.

[51] Morgan D, Van der Ven A, Ceder G, 'Li Conductivity in Li_xMPO_4 (M = Mn, Fe, Co, Ni) Olivine Materials', Electrochemical and Solid-State Letters (2004) Vol:7, p:A30-A32.

[52] Kim S-W, Kim J, Gwon H, Kang K, 'Phase Stability Study of $Li_{1-x}MnPO_4$ ($0 \leq x \leq 1$) Cathode for Li Rechargeable Battery', Journal of The Electrochemical Society (2009) Vol:156, p:A635-A638.

[53] Bramnik NN, Nikolowski K, Trots DM, Ehrenberg H, 'Thermal Stability of $LiCoPO_4$ Cathodes', Electrochemical and Solid-State Letters (2008) Vol:11, p:A89-A93.

[54] Chen Y-C, Chen J-M, Hsu C-H, Yeh J-W, Shih HC, Chang Y-S, Sheu H-S, 'Structure studies on $LiMn_{0.25}Fe_{0.75}PO_4$ by in-situ synchrotron X-ray diffraction analysis', Journal of Power Sources (2009) Vol:189, p:790-793.

[55] Nakamura T, Sakumoto K, Seki S, Kobayashi Y, Tabuchi M, Yamada Y, 'Apparent Diffusion Constant and Electrochemical Reaction in $LiFe_{1-x}$ Mn_xPO_4 Olivine Cathodes', Journal of The Electrochemical Society (2007) Vol:154, p:A1118-A1123.

[56] Shanmukaraj D, Wang GX, Murugan R, Liu HK, 'Electrochemical studies on $LiFe_{1-x}Co_xPO_4$/carbon composite cathode materials synthesized by citrate gel technique for lithium-ion batteries', Materials Science and Engineering: B (2008) Vol:149, p:93-98.

[57] Chen Q, Wang J, Tang Z, He W, Shao H, Zhang J, 'Electrochemical performance of the carbon coated $Li_3V_2(PO_4)_3$ cathode material synthesized by a sol-gel method', Electrochimica Acta (2007) Vol:52, p:5251-5257.

[58] Roth EP. 43rd Power Sources Conference. Philadelphia, PA, 2008.

[59] Stewart SG, Srinivasan V, Newman J, 'Modeling the Performance of Lithium-Ion Batteries and Capacitors during Hybrid-Electric-Vehicle Operation', Journal of The Electrochemical Society (2008) Vol:155, p:A664-A671.

[60] Yamada A, Koizumi H, Nishimura S-i, Sonoyama N, Kanno R, Yonemura M, Nakamura T, Kobayashi Y, 'Room-temperature miscibility gap in Li_xFePO_4', Nat Mater (2006) Vol:5, p:357-360.

[61] Dreyer W, Jamnik J, Guhlke C, Huth R, Moskon J, Gaberscek M, 'The thermodynamic origin of hysteresis in insertion batteries', Nat Mater (2010) Vol:9, p:448-453.

[62] Hsu K-F, Hu S-K, Chen C-H, Cheng M-Y, Tsay S-Y, Chou T-C, Sheu H-S, Lee J-F, Hwang B-J, 'Formation mechanism of $LiFePO_4$/C composite powders investigated by X-ray absorption spectroscopy', Journal of Power Sources (2009) Vol:192, p:660-667.

[63] Wang Q, Ping P, Zhao X, Chu G, Sun J, Chen C, 'Thermal runaway caused fire and explosion of lithium ion battery', Journal of Power Sources (2012) Vol:208, p:210-224.

[64] Chen Z, Dahn JR, 'Reducing Carbon in $LiFePO_4$/C Composite Electrodes to Maximize Specific Energy, Volumetric Energy, and Tap Density', Journal of The Electrochemical Society (2002) Vol:149, p:A1184-A1189.

[65] Chung S-Y, Bloking JT, Chiang Y-M, 'Electronically conductive phospho-olivines as lithium storage electrodes', Nat Mater (2002) Vol:1, p:123-128.

[66] N. Jayaprakash, N. Kalaiselvi, Periasamy P, 'Synthesis and Characterization of $LiM_xFe_{1-x}PO_4$ (M = Cu, Sn; x = 0.02) Cathodes - A study on the Effect of Cation Substitution in $LiFePO_4$ Material', International Journal of Electrochemical Science (2008) Vol:3, p:476-488.

[67] Herle PS, Ellis B, Coombs N, Nazar LF, 'Nano-network electronic conduction in iron and nickel olivine phosphates', Nat Mater (2004) Vol:3, p:147-152.

[68] Hu Y, Doeff MM, Kostecki R, Finones R, 'Electrochemical Performance of Sol-Gel Synthesized $LiFePO_4$ in Lithium Batteries', Journal of The Electrochemical Society (2004) Vol:151, p:A1279-A1285.

[69] Croce F, Epifanio AD, Hassoun J, Deptula A, Olczac T, Scrosati B, 'A Novel Concept for the Synthesis of an Improved $LiFePO_4$ Lithium Battery Cathode', Electrochemical and Solid-State Letters (2002) Vol:5, p:A47-A50.

[70] Park KS, Son JT, Chung HT, Kim SJ, Lee CH, Kang KT, Kim HG, 'Surface modification by silver coating for improving electrochemical properties of $LiFePO_4$', Solid State Communications (2004) Vol:129, p:311-314.

[71] Jayaprakash N, Kalaiselvi N, Periasamy P, 'Synthesis and Characterization of $LiM_xFe_{1-x}PO_4$ (M = Cu, Sn; x = 0.02) Cathodes - A study on the Effect of Cation Substitution in $LiFePO_4$ Material', International Journal of Electrochemical Science (2008) Vol:3, p:476-488.

[72] Wagemaker M, Ellis BL, Lutzenkirchen-Hecht D, Mulder FM, Nazar LF, 'Proof of Supervalent Doping in Olivine $LiFePO_4$', Chemistry of Materials (2008) Vol:20, p:6313-6315.

[73] Delmas C, Maccario M, Croguennec L, Le Cras F, Weill F, 'Lithium deintercalation in $LiFePO_4$ nanoparticles via a domino-cascade model', Nat Mater (2008) Vol:7, p:665-671.

[74] Rousse G, Rodriguez-Carvajal J, Patoux S, Masquelier C, 'Magnetic Structures of the Triphylite $LiFePO_4$ and of Its Delithiated Form $FePO_4$', Chemistry of Materials (2003) Vol:15, p:4082-4090.

[75] Srinivasan V, Newman J, 'Discharge Model for the Lithium Iron-Phosphate Electrode', Journal of The Electrochemical Society (2004) Vol:151, p:A1517-A1529.

[76] Andersson AS, Thomas JO, 'The source of first-cycle capacity loss in $LiFePO_4$', Journal of Power Sources (2001) Vol:97-98, p:498-502.

[77] Delacourt C, Safari M, 'Analysis of lithium deinsertion/insertion in $LiyFePO_4$ with a simple mathematical model', Electrochimica Acta (2011) Vol:56, p:5222-5229.

[78] Malik R, Zhou F, Ceder G, 'Kinetics of non-equilibrium lithium incorporation in $LiFePO_4$', Nat Mater (2011) Vol:10, p:587-590.

[79] Laffont L, Delacourt C, Gibot P, Wu MY, Kooyman P, Masquelier C, Tarascon JM, 'Study of the $LiFePO_4/FePO_4$ Two-Phase System by High-Resolution Electron Energy Loss Spectroscopy', Chemistry of Materials (2006) Vol:18, p:5520-5529.

[80] Ramana CV, Mauger A, Gendron F, Julien CM, Zaghib K, 'Study of the Li-insertion/extraction process in $LiFePO_4/FePO_4$', Journal of Power Sources (2009) Vol:187, p:555-564.

[81] Chen G, Song X, Richardson TJ, 'Electron Microscopy Study of the $LiFePO_4$ to $FePO_4$ Phase Transition', Electrochemical and Solid-State Letters (2006) Vol:9, p:A295-A298.

[82] Meethong N, Kao Y-H, Carter WC, Chiang Y-M, 'Comparative Study of Lithium Transport Kinetics in Olivine Cathodes for Li-ion Batteries ', Chemistry of Materials (2009) Vol:22, p:1088-1097.

[83] Islam MS, Driscoll DJ, Fisher CAJ, Slater PR, 'Atomic-Scale Investigation of Defects, Dopants, and Lithium Transport in the $LiFePO_4$ Olivine-Type Battery Material', Chemistry of Materials (2005) Vol:17, p:5085-5092.

[84] Maxisch T, Zhou F, Ceder G, 'Ab initio study of the migration of small polarons in olivine Li_xFePO_4 and their association with lithium ions and vacancies', Physical Review B (2006) Vol:73, p:104301.

[85] Brunetti G, Robert D, Bayle-Guillemaud P, Rouviere JL, Rauch EF, Martin JF, Colin JF, Bertin F, Cayron C, 'Confirmation of the Domino-Cascade Model by

$LiFePO_4/FePO_4$ Precession Electron Diffraction', Chemistry of Materials (2011) Vol:23, p:4515-4524.

[86] Badi S-P, Wagemaker M, Ellis BL, Singh DP, Borghols WJH, Kan WH, Ryan DH, Mulder FM, Nazar LF, 'Direct synthesis of nanocrystalline $Li_{0.90}FePO_4$: observation of phase segregation of anti-site defects on delithiation', Journal of Materials Chemistry (2011) Vol:21, p:10085-10093.

[87] Weichert K, Sigle W, van Aken PA, Jamnik J, Zhu C, Amin R, Acarturk T, Starke U, Maier J, 'Phase Boundary Propagation in Large $LiFePO_4$ Single Crystals on Delithiation', Journal of the American Chemical Society (2012) Vol:134, p:2988-2992.

[88] Moreau P, Mauchamp V, Pailloux F, Boucher F, 'Fast determination of phases in Li_xFePO_4 using low losses in electron energy-loss spectroscopy', Applied Physics Letters (2009) Vol:94, p:123111.

[89] Suo L, Han W, Lu X, Gu L, Hu Y-S, Li H, Chen D, Chen L, Tsukimoto S, Ikuhara Y, 'Highly ordered staging structural interface between $LiFePO_4$ and $FePO_4$', Physical Chemistry Chemical Physics (2012) Vol:14, p:5363-5367.

[90] Yu X, Wang Q, Zhou Y, Li H, Yang X-Q, Nam K-W, Ehrlich SN, Khalid S, Meng YS, 'High rate delithiation behaviour of $LiFePO_4$ studied by quick X-ray absorption spectroscopy', Chemical Communications (2012) Vol:48, p:11537-11539.

[91] Liu X, Liu J, Qiao R, Yu Y, Li H, Suo L, Hu Y-s, Chuang Y-D, Shu G, Chou F, Weng T-C, Nordlund D, Sokaras D, Wang YJ, Lin H, Barbiellini B, Bansil A, Song X, Liu Z, Yan S, Liu G, Qiao S, Richardson TJ, Prendergast D, Hussain Z, de Groot FMF, Yang W, 'Phase Transformation and Lithiation Effect on Electronic

Structure of Li_xFePO_4: An In-Depth Study by Soft X-ray and Simulations', Journal of the American Chemical Society (2012) Vol:134, p:13708-13715.

[92] Oyama G, Yamada Y, Natsui R-i, Nishimura S-i, Yamada A, 'Kinetics of Nucleation and Growth in Two-Phase Electrochemical Reaction of Li_xFePO_4', The Journal of Physical Chemistry C (2012) Vol:116, p:7306-7311.

[93] Allen JL, Jow TR, Wolfenstine J, 'Kinetic Study of the Electrochemical $FePO_4$ to $LiFePO_4$ Phase Transition', Chemistry of Materials (2007) Vol:19, p:2108-2111.

[94] Dedryvere R, Maccario M, Croguennec L, Le Cras F, Delmas C, Gonbeau D, 'X-Ray Photoelectron Spectroscopy Investigations of Carbon-Coated Li_xFePO_4 Materials', Chemistry of Materials (2008) Vol:20, p:7164-7170.

[95] Chang H-H, Chang C-C, Wu H-C, Yang M-H, Sheu H-S, Wu N-L, 'Study on dynamics of structural transformation during charge/discharge of $LiFePO_4$ cathode', Electrochemistry Communications (2008) Vol:10, p:335-339.

[96] Love CT, Korovina A, Patridge CJ, Swider-Lyons KE, Twigg ME, Ramaker DE, 'Review of $LiFePO_4$ Phase Transition Mechanisms and New Observations from X-ray Absorption Spectroscopy', Journal of The Electrochemical Society (2013) Vol:160, p:A3153-A3161.

[97] Meethong N, Kao Y-H, Tang M, Huang H-Y, Carter WC, Chiang Y-M, 'Electrochemically Induced Phase Transformation in Nanoscale Olivines $Li_{1-x}MPO_4$ (M = Fe, Mn)', Chemistry of Materials (2008) Vol:20, p:6189-6198.

[98] Wang X-J, Jaye C, Nam K-W, Zhang B, Chen H-Y, Bai J, Li H, Huang X, Fischer DA, Yang X-Q, 'Investigation of the structural changes in $Li_{1-x}FePO_4$ upon charging by synchrotron radiation techniques', Journal of Materials Chemistry (2011) Vol:21, p:11406-11411.

[99] Gu L, Zhu C, Li H, Yu Y, Li C, Tsukimoto S, Maier J, Ikuhara Y, 'Direct Observation of Lithium Staging in Partially Delithiated $LiFePO_4$ at Atomic Resolution', Journal of the American Chemical Society (2011) Vol:133, p:4661-4663.

[100] Andersson AS, Kalska B, Haggstrom L, Thomas JO, 'Lithium extraction/insertion in $LiFePO_4$: an X-ray diffraction and Mossbauer spectroscopy study', Solid State Ionics (2000) Vol:130, p:41-52.

[101] Leriche JB, Hamelet S, Shu J, Morcrette M, Masquelier C, Ouvrard G, Zerrouki M, Soudan P, Belin S, Elkaim E, Baudelet F, 'An Electrochemical Cell for Operando Study of Lithium Batteries Using Synchrotron Radiation', Journal of The Electrochemical Society (2010) Vol:157, p:A606-A610.

[102] Jing W, Gopi Krishna Phani D, Chunwen S, Murali GT, Danielle A, Anthony GD, Arumugam M, Graeme H, John BG, Keith JS, 'In situ Raman spectroscopy of $LiFePO_4$: size and morphology dependence during charge and self-discharge', Nanotechnology (2013) Vol:24, p:424009.

[103] Srinivasan V, Newman J, 'Existence of Path-Dependence in the $LiFePO_4$ Electrode', Electrochemical and Solid-State Letters (2006) Vol:9, p:A110-A114.

[104] Allen JL, Jow TR, Wolfenstine J, 'Analysis of the $FePO_4$ to $LiFePO_4$ phase transition', Journal of Solid State Electrochemistry (2008) Vol:12, p:1031-1033.

[105] Meethong N, Huang H-YS, Carter WC, Chiang Y-M, 'Size-Dependent Lithium Miscibility Gap in Nanoscale $Li_{1-x}FePO_4$', Electrochemical and Solid-State Letters (2007) Vol:10, p:A134-A138.

[106] Salehi A, 'Performance qualification and Raman investigation on cell behavior and aging of $LiFePO_4$ cathodes in Lithium-ion Batteries'. Materials Science and

Engineering, vol. Master of Science. Arlington: The University of Texas at Arlington, 2013. p:91.

[107] Aroca R, Nazri M, Nazri GA, Camargo AJ, Trsic M, 'Vibrational Spectra and Ion-Pair Properties of Lithium Hexafluorophosphate in Ethylene Carbonate Based Mixed-Solvent Systems for Lithium Batteries', Journal of Solution Chemistry (2000) Vol:29, p:1047-1060.

[108] Battisti D, Nazri GA, Klassen B, Aroca R, 'Vibrational studies of lithium perchlorate in propylene carbonate solutions', The Journal of Physical Chemistry (1993) Vol:97, p:5826-5830.

[109] Huang W, Frech R, Wheeler RA, 'Molecular structures and normal vibrations of trifluoromethane sulfonate ($CF_3SO_3^-$) and its lithium ion pairs and aggregates', The Journal of Physical Chemistry (1994) Vol:98, p:100-110.

[110] Klassen B, Aroca R, Nazri M, Nazri GA, 'Raman Spectra and Transport Properties of Lithium Perchlorate in Ethylene Carbonate Based Binary Solvent Systems for Lithium Batteries', The Journal of Physical Chemistry B (1998) Vol:102, p:4795-4801.

[111] Palomares V, Goni A, Muro IGd, de Meatza I, Bengoechea M, Cantero I, Rojo T, 'Conductive additive content balance in Li-ion battery cathodes: Commercial carbon blacks vs. in situ carbon from $LiFePO_4$/C composites', Journal of Power Sources (2010) Vol:195, p:7661-7668.

[112] Nikiel L, Jagodzinski PW, 'Raman spectroscopic characterization of graphites: A re-evaluation of spectra/ structure correlation', Carbon (1993) Vol:31, p:1313-1317.

[113] Huang W, Frech R, 'In Situ Roman Studies of Graphite Surface Structures during Lithium Electrochemical Intercalation', Journal of The Electrochemical Society (1998) Vol:145, p:765-770.

[114] Wang Y, Alsmeyer DC, McCreery RL, 'Raman spectroscopy of carbon materials: structural basis of observed spectra', Chemistry of Materials (1990) Vol:2, p:557-563.

[115] Wilcox JD, Doeff MM, Marcinek M, Kostecki R, 'Factors Influencing the Quality of Carbon Coatings on $LiFePO_4$', Journal of The Electrochemical Society (2007) Vol:154, p:A389-A395.

[116] Nagpure SC, Bhushan B, Babu SS, 'Raman and NMR studies of aged $LiFePO_4$ cathode', Applied Surface Science (2012) Vol:259, p:49-54.

[117] Markevich E, Sharabi R, Haik O, Borgel V, Salitra G, Aurbach D, Semrau G, Schmidt MA, Schall N, Stinner C, 'Raman spectroscopy of carbon-coated $LiCoPO_4$ and $LiFePO_4$ olivines', Journal of Power Sources (2011) Vol:196, p:6433-6439.

[118] Burba CM, Frech R, 'Raman and FTIR Spectroscopic Study of Li_xFePO_4 ($0 \leq x \leq 1$)', Journal of The Electrochemical Society (2004) Vol:151, p:A1032-A1038.

[119] Zhang X, Frech R, 'In Situ Raman Spectroscopy of $Li_xV_2O_5$ in a Lithium Rechargeable Battery', Journal of The Electrochemical Society (1998) Vol:145, p:847-851.

[120] Panitz J-C, Novak P, 'Raman microscopy as a quality control tool for electrodes of lithium-ion batteries', Journal of Power Sources (2001) Vol:97-98, p:174-180.

[121] Doeff MM, Hu Y, McLarnon F, Kostecki R, 'Effect of Surface Carbon Structure on the Electrochemical Performance of $LiFePO_4$', Electrochemical and Solid-State Letters (2003) Vol:6, p:A207-A209.

[122] Robertson J, 'Diamond-like amorphous carbon', Materials Science and Engineering: R: Reports (2002) Vol:37, p:129-281.

[123] Tuinstra F, Koenig JL, 'Raman Spectrum of Graphite', The Journal of Chemical Physics (1970) Vol:53, p:1126-1130.

[124] Vidano R, Fischbach DB, 'New Lines in the Raman Spectra of Carbons and Graphite', Journal of the American Ceramic Society (1978) Vol:61, p:13-17.

[125] Morita M, Asai Y, Yoshimoto N, Ishikawa M, 'A Raman spectroscopic study of organic electrolyte solutions based on binary solvent systems of ethylene carbonate with low viscosity solvents which dissolve different lithium salts', Journal of the Chemical Society, Faraday Transactions (1998) Vol:94, p:3451-3456.

[126] Gabrisch H, Wilcox J, Doeff MM, 'TEM Study of Fracturing in Spherical and Plate-like $LiFePO_4$ Particles', Electrochemical and Solid-State Letters (2008) Vol:11, p:A25-A29.

[127] Eventoff W, Robert M, Reacor DR, 'The Crystal Structure of Heterosite', American Mineralogist (1972) Vol:57, p:45-51.

[128] Burch D, Bazant MZ, 'Size-Dependent Spinodal and Miscibility Gaps for Intercalation in Nanoparticles', Nano Letters (2009) Vol:9, p:3795-3800.

[129] Safari M, Morcrette M, Teyssot A, Delacourt C, 'Multimodal Physics-Based Aging Model for Life Prediction of Li-Ion Batteries', Journal of The Electrochemical Society (2009) Vol:156, p:A145-A153.

[130] Wagemaker M, Singh DP, Borghols WJH, Lafont U, Haverkate L, Peterson VK, Mulder FM, 'Dynamic Solubility Limits in Nanosized Olivine LiFePO4', Journal of the American Chemical Society (2011) Vol:133, p:10222-10228.

[131] Zaghib K, Mauger A, Gendron F, Julien CM, 'Surface Effects on the Physical and Electrochemical Properties of Thin $LiFePO_4$ Particles', Chemistry of Materials (2007) Vol:20, p:462-469.

[132] Wagemaker M, Mulder FM, Van der Ven A, 'The Role of Surface and Interface Energy on Phase Stability of Nanosized Insertion Compounds', Advanced Materials (2009) Vol:21, p:2703-2709.

[133] Smith KC, Mukherjee PP, Fisher TS, 'Columnar order in jammed $LiFePO_4$ cathodes: ion transport catastrophe and its mitigation', Physical Chemistry Chemical Physics (2012) Vol:14, p:7040-7050.

[134] Meethong N, Huang HYS, Speakman SA, Carter WC, Chiang YM, 'Strain Accommodation during Phase Transformations in Olivine-Based Cathodes as a Materials Selection Criterion for High-Power Rechargeable Batteries', Advanced Functional Materials (2007) Vol:17, p:1115-1123.

[135] Zhu Y, Wang C, 'Strain accommodation and potential hysteresis of $LiFePO_4$ cathodes during lithium ion insertion/extraction', Journal of Power Sources (2011) Vol:196, p:1442-1448.

[136] Kang B, Ceder G, 'Battery materials for ultrafast charging and discharging', Nature (2009) Vol:458, p:190-193.

[137] Xia Y, Fujieda T, Tatsumi K, Prosini PP, Sakai T, 'Thermal and electrochemical stability of cathode materials in solid polymer electrolyte', Journal of Power Sources (2001) Vol:92, p:234-243.

[138] Zhang Y, Wang C-Y, Tang X, 'Cycling degradation of an automotive $LiFePO_4$ lithium-ion battery', Journal of Power Sources (2011) Vol:196, p:1513-1520.

[139] Kasavajjula US, Wang C, Arce PE, 'Discharge Model for $LiFePO_4$ Accounting for the Solid Solution Range', Journal of The Electrochemical Society (2008) Vol:155, p:A866-A874.

[140] Wang C, Kasavajjula US, Arce PE, 'A Discharge Model for Phase Transformation Electrodes: Formulation, Experimental Validation, and Analysis', The Journal of Physical Chemistry C (2007) Vol:111, p:16656-16663.

[141] Tang M, Belak JF, Dorr MR, 'Anisotropic Phase Boundary Morphology in Nanoscale Olivine Electrode Particles', The Journal of Physical Chemistry C (2011) Vol:115, p:4922-4926.

Biographical Information

Md Noor E Alam Siddique was born in Khulna, Bangladesh and got his primary education there. He received his Bachelor of Science (BS) degree in Materials and Metallurgical Engineering from Bangladesh University of Engineering and Technology, Dhaka, Bangladesh in 2007. As recognition for being ranked first in his class in BS program, he was appointed as lecturer in the Materials and Metallurgical Engineering department (MME) to teach undergraduate courses. Also he received Amir Khushbahar Gold medal for holding highest CGPA (grade point) in the MME dept, and Engineers 6061 gold medal for achieving highest CGPA in the Engineering faculty consisting of some other engineering departments. He also received his Master of Science (MS) degree from the same institution in 2009.

In 2009 he joined The University of Texas at Arlington to pursue his doctoral degree and worked under supervision of Dr. Fuqiang Liu of Materials Science and Engineering and received his Ph.D. degree in 2014. His primary research area during his doctoral study was science, engineering and technology of lithium ion battery materials, while he also worked on PEM fuel cell catalyst, vanadium redox flow battery and synthesizing nanostructures for lithium ion batteries. His research results were published in several journals and are listed beleow.

1) N A Siddique, Ashley M Allen, Partha P Mukherjee, Fuqiang Li, “Simulation of effect of interfacial lithium flux on miscibility gap in non-equilibrium phase transformation of $LiFePO_4$ particles”, Journal of Power Sources 245 (2014) 83-88.

2) N. Siddique, Amir Salehi, Fuqiang Liu, “Stochastic reconstruction and electrical transport studies of porous cathode of Li-ion batteries”, Journal of Power Sources 217 (2012) 437-443.

3) Fuqiang Liu, N. A. Siddique, and Partha P. Mukherjee, “Nonequilibrium Phase Transformation and Particle Shape Effect in $LiFePO_4$ Materials for Li-Ion Batteries”, Electrochemical and Solid-State Letters, 14 (10) A143-A147 (2011).

4) Fuqiang Liu and N A Siddique, “ Microstructure Reconstruction and Direct Evaluation of Li-Ion Battery Cathodes”, ECS Transactions, 33 (24) 25-32 (2011).

5) N.A. Siddique, Fuqiang Liu, “Process based reconstruction and simulation of a three-dimensional fuel cell catalyst layer”, Electrochimica Acta 55 (2010) 5357–5366.

6) N A Siddique, A S W Kurny, “Kinetics of leaching of alumina from discarded high alumina refractory bricks”, International Journal of Engineering & Technology IJET-IJENS Vol: 10 No: 01 23-26.

He plans to work in the industries to gain more practical experience that he can use later on in his research either in some universities or research institutes. He also plans to start business in future in the developing countries. But mostly he is keen to remain attached to academia somehow.